

# MIXING AND RADIATION PROPERTIES OF BUOYANT TURBULENT DIFFUSION FLAMES

---

Z. Dai, L.-K. Tseng,  
U.O. Koylu, and G.M. Faeth  
Department of Aerospace Engineering  
University of Michigan  
Ann Arbor, MI 48109-2118

October 1994  
Issued June 1995



**U.S. Department of Commerce**  
Ronald H. Brown, *Secretary*  
**Technology Administration**  
Mary L. Good, *Under Secretary for Technology*  
National Institute of Standards and Technology  
Arati Prabhakar, *Director*

### Notice

This report was prepared for the Building and Fire Research Laboratory of the National Institute of Standards and Technology under grant number 60NANB1D1175. The statement and conclusions contained in this report are those of the authors and do not necessarily reflect the views of the National Institute of Standards and Technology or the Building and Fire Research Laboratory.

# **Modeling and Experimental Validation of Pyrotechnic Gas Generators**

**Herman Krier**  
The University of Illinois at Urbana-Champaign  
Urbana, Illinois

and

**P. Barry Butler**  
The University of Iowa  
Iowa City, Iowa

**NIST Gas Generator Workshop  
Gaithersburg, MD**

**28 June, 1995**

# REFERENCES

---

Butler, P.B., Krier, H.K., Faigle, E.M., Semcherna, J.H., and Thompson, R., **"Modeling Azide-Based Propellant Combustion in a Passenger-Side Automotive Airbag Inflator,"** The Combustion Institute Central States Meeting, April 26, 1992, Columbus, OH.

Butler, P.B., Kang, J., and Krier, H., **"Modeling Pyrotechnic Combustion in an Automotive Airbag Inflator,"** 5th International Congress of the Groupe de Travail de Pyrotechnie, June, 1993, France.

Butler, P.B., Kang, J., and Krier, H., **"Modeling and Numerical Simulation of the Internal Thermochemistry of an Automotive Airbag Inflator,"** Progress in Energy and Combustion Science, Vol. 19, 1993, pp. 365-382.

Butler, P.B., Kang, J., and Krier, H., **"Numerical Simulation of a Pre-Pressurized Pyrotechnic Automotive Airbag Inflator,"** 5th International Congress of the Groupe de Travail de Pyrotechnie, June, 1993, France.

Berger, J.M., and Butler, P.B., **"Equilibrium Analysis of of Three Classes of Automotive Airbag Inflator Propellants,"** Combustion Science and Technology, Vol. 104, No. 1-3, 1995, pp. 93-114.

Greenlee, C.L., and Butler, P.B., **"Influence of Product Species Selection on Thermochemical Equilibrium Calculations, Part I: Energetic Materials,"** submitted to Propellants, Explosives, and Pyrotechnics, 1995.

# **BACKGROUND**

---

- **CONSULTANTS TO AIRBAG INDUSTRY**
  - **MODELING WORK**
    - **developed general-purpose gas generator models**
    - **validated performance of numerous inflators**
    - **used in design of new inflators**
  - **EXPERIMENTAL WORK**
    - **cold-flow test apparatus**
    - **combustion test apparatus**
    - **ignition test apparatus**
    - **design of experiments (DOE)**
  - **ADVANCED CONCEPTS**
    - **next-generation inflator designs**
-

# AIRBAG COMPONENTS

---

- CRASH SENSORS AND COMPUTER LOGIC

- INFLATOR UNIT (i.e., both hybrid and pyrotechnic gas generators)

- ignitor
- propellant grains
- hardware items
- particle filter

- BAG HOLDER AND EXTERIOR PADDING

- NYLON AIRBAG ASSEMBLY

---

# ENGINEERING CHALLENGES

---

- **IGNITOR RELIABILITY** (output history, is it repeatable ?)
  - **TIMING OF EVENTS** (pressure-time profiles)
  - **PRODUCT CHEMICAL COMPOSITION**
    - tank gas
    - tank particulates
    - inflator slag (multi-phase mixture)
  - **AMBIENT OPERATING ENVIRONMENT**
    - temperature
    - pressure
  - **AIRBAG DEPLOYMENT**
    - dynamics of bag filling
    - thermal and mechanical response of bag as it opens
  - **PROPELLANT LIFE** (>15 years)
  - **PROPELLANT DISPOSAL**
-

# GOALS AND OBJECTIVES

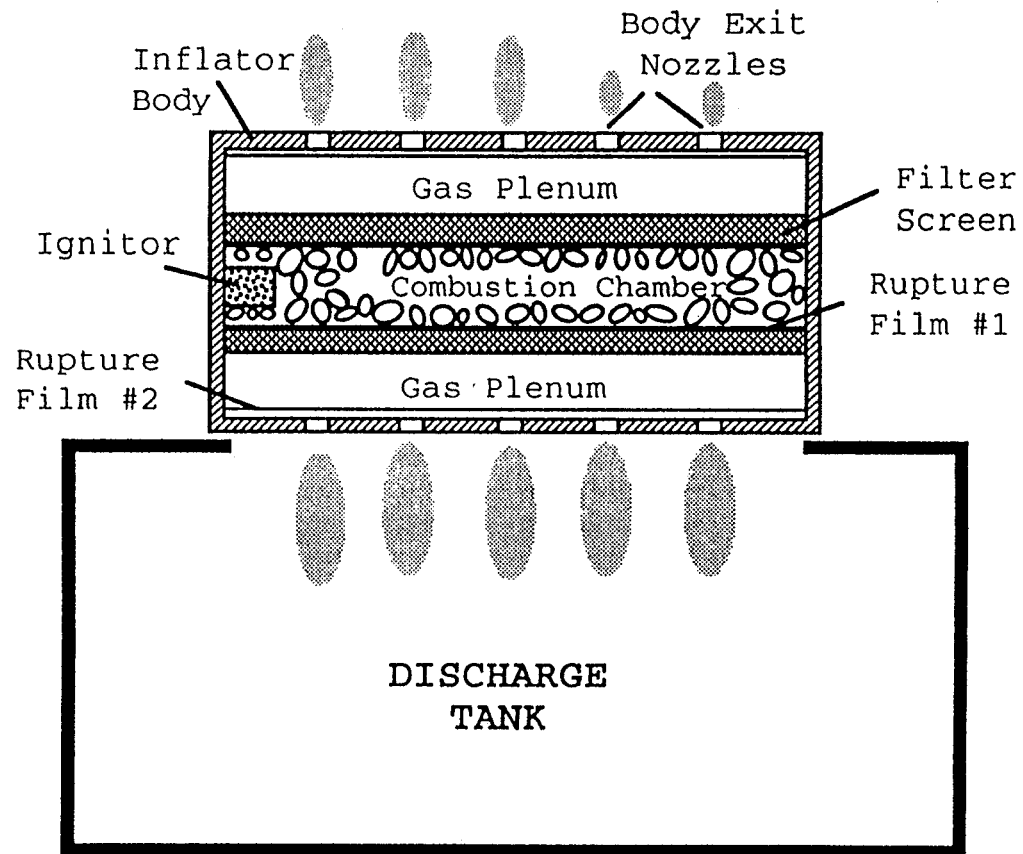
---

- **DEVELOP A MODEL THAT DESCRIBES THE THERMOCHEMICAL EVENTS OCCURRING IN A GAS GENERATOR**
  - **VALIDATE MODEL WITH EXPERIMENTS**
  - **STUDY THE INFLUENCE OF MATERIAL PROPERTIES AND DESIGN PARAMETERS ON PERFORMANCE OF GAS GENERATOR**
    - **maximum inflator pressure, temperature**
    - **maximum tank pressure, temperature**
    - **tank impulse**
    - **pressure-time profiles**
    - **temperature-time profiles**
    - **tank gas composition**
  - **COMPUTER PROGRAM FOR DESIGN OF NEW GAS GENERATORS**
-

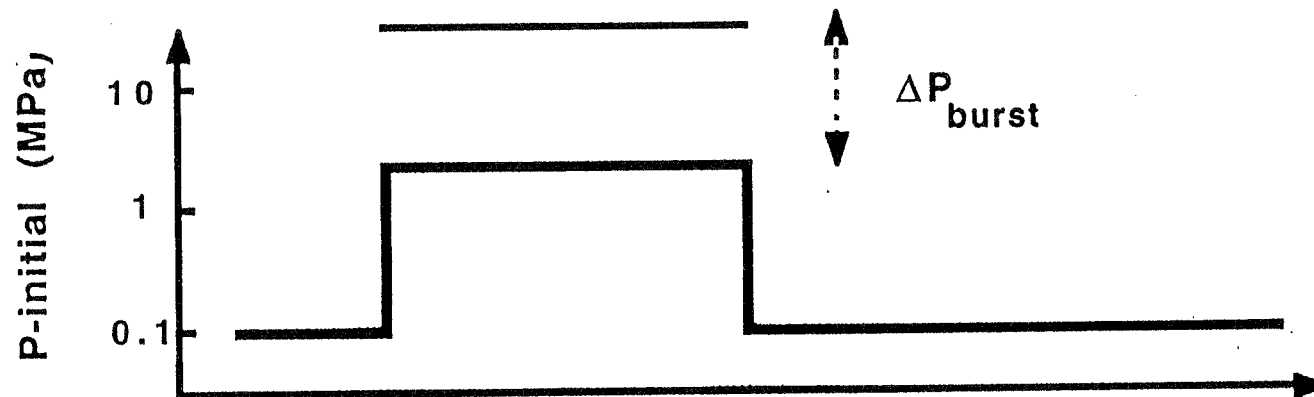
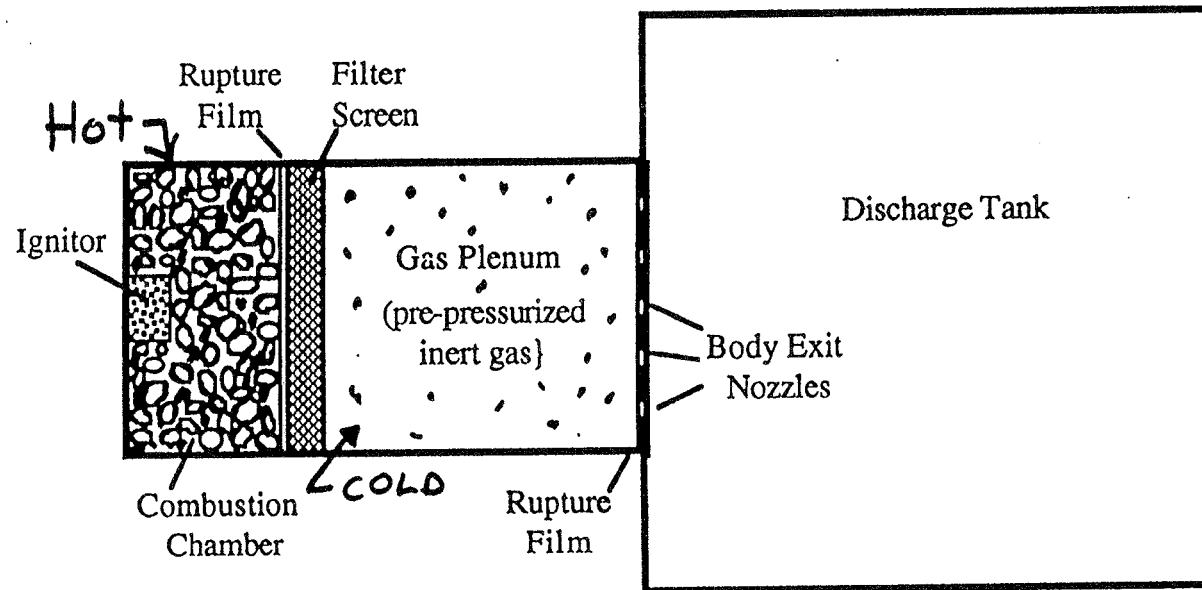


# PHYSICAL MODEL OF GAS GENERATOR AND DISCHARGE TANK

---



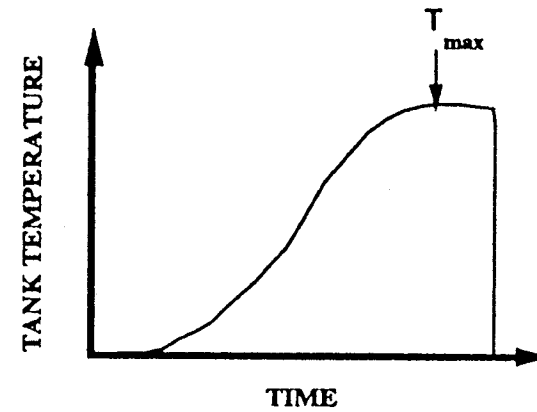
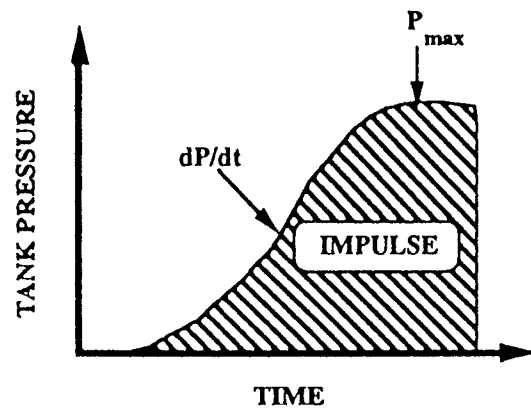
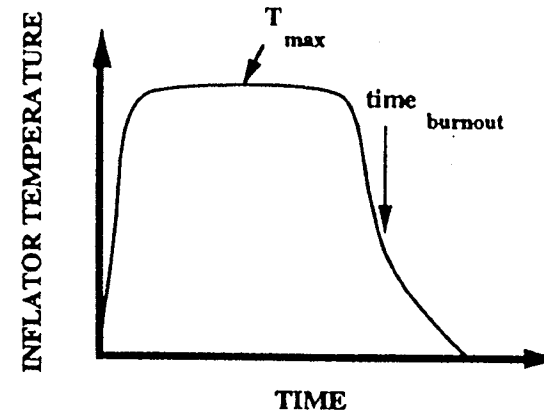
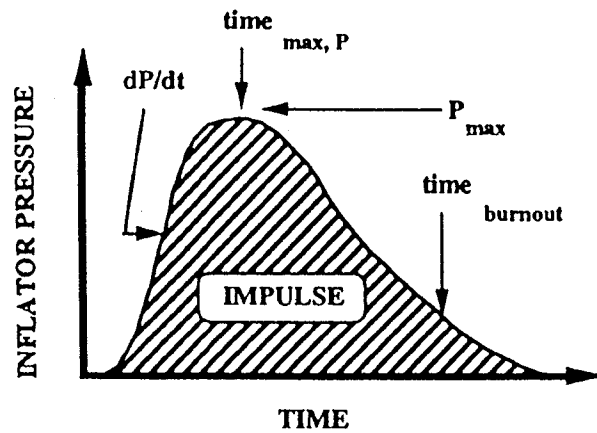
# GAS-ASSISTED PYROTECHNIC INFLATOR



# GAS GENERATOR PERFORMANCE PARAMETERS

---

L6



# COMPUTER SIMULATION

---

- **KEY FEATURES INCLUDED IN MODEL**

- ignition time delay (flame spreading)
- tracks individual species with time (g, s, l)
- grain geometry (form function)
- nozzle discharge flow rates
- filter collection process and gas flow restriction

- **MODEL PREDICTING**

- $P_J(t)$ ,  $T_J(t)$ ,  $X_J(t)$
- heat exchange rates
- hardware temperatures
- propellant properties per time
- flow properties at exit nozzle

- **EXPERIMENTAL VALIDATION DATA**

- ignition delay time
- mass of collected particles in filter
- $P_J(t)$ ,  $T_J(t)$ ,  $X_{JJ}(t = \infty)$ ,  $P_{JJ}(t = \infty)$

- **NUMERICAL PROCEDURE**

- large system of ODE's ( $dT_i/dt$ ,  $dm_k/dt$ , etc.)
- solved using DVODE
- CPU time is 0.1 - 1 minute on HP-735

# MODEL DESCRIPTION

---

- **BASED ON FUNDAMENTAL CONSERVATION LAWS (MASS, ENERGY)**
  - **TWO MAJOR SUBSYSTEMS CONSIDERED:**
    - **gas generator assembly**
    - **discharge tank**
  - **GAS GENERATOR ASSEMBLY INCLUDES:**
    - **body (metal hardware)**
    - **propellant grains**
    - **ignitor assembly**
    - **filter screen**
    - **thin metal foil for environmental seal and burst strength**
  - **DISCHARGE TANK INCLUDES:**
    - **tank walls (heat loss)**
    - **mass discharged from inflator**
  - **DIFFERENT MODES OF HEAT TRANSFER ARE CONSIDERED**
-

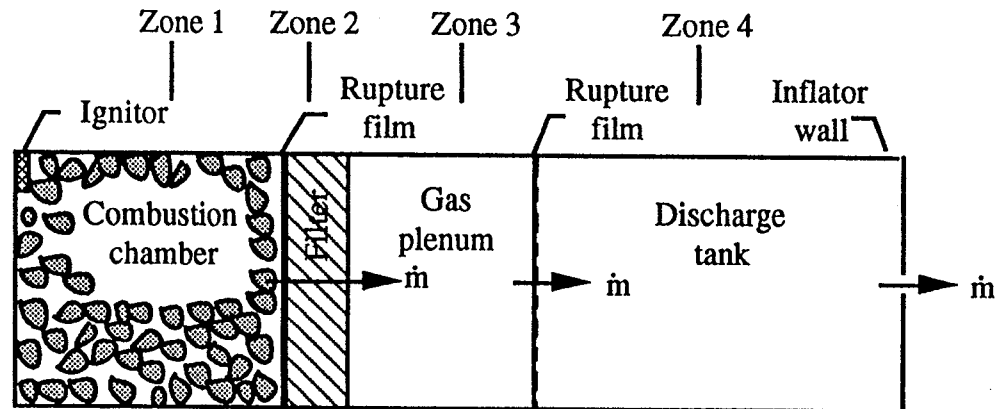
# MODEL ASSUMPTIONS

---

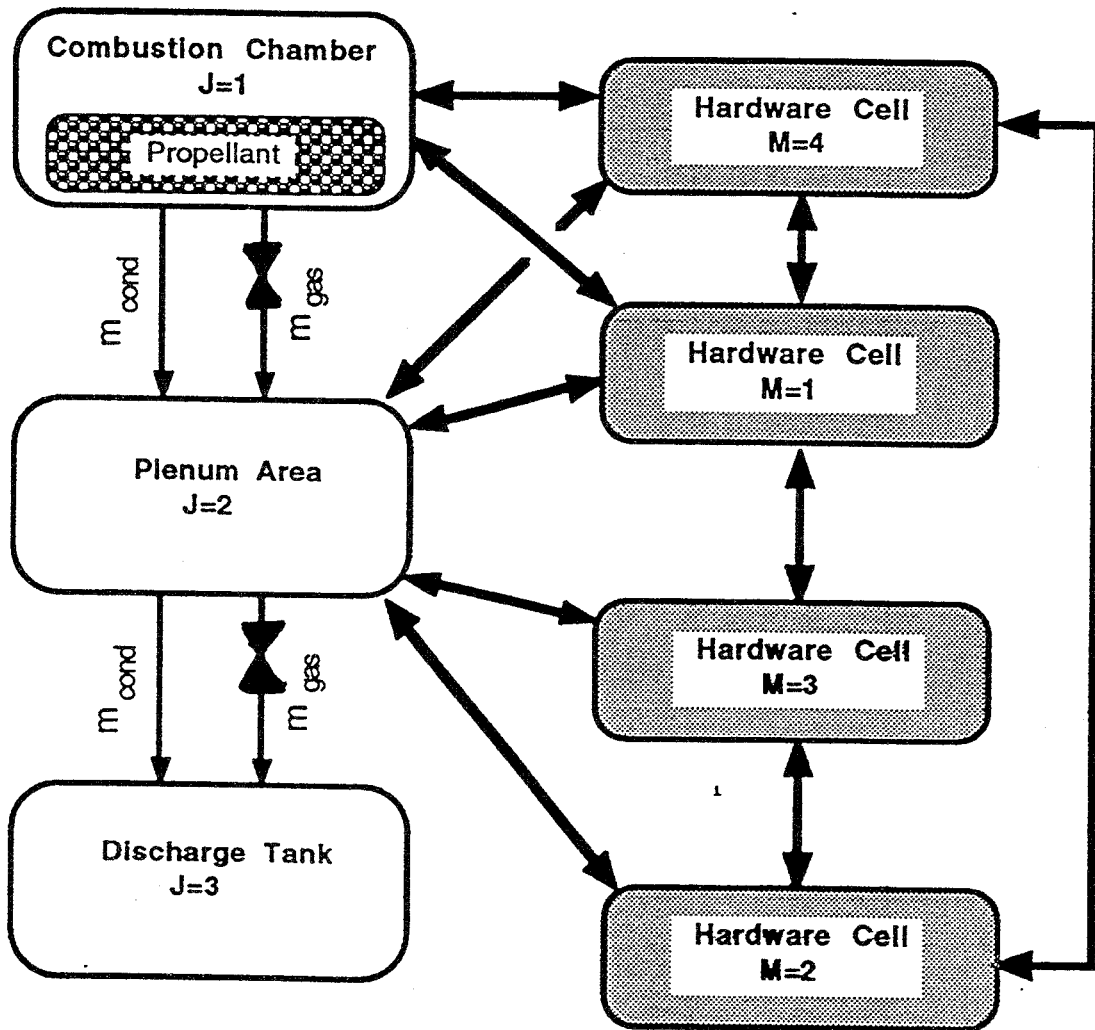
- FILTER DOES NOT COLLECT GAS SPECIES
  - FILTER DOES COLLECT SOLID AND LIQUID PRODUCTS OF COMBUSTION
    - collection efficiency depends on filter design (mass, fiber size, etc.)
  - GAS MIXTURE IS:
    - multiple species
    - $C_p(T)$
    - well-mixed, perfect gas
    - can be chemically reactive
  - CONDENSED SPECIES ARE:
    - multiple species
    - $C_p(T)$
    - not compressible
-

# COMPUTATIONAL MODEL OF GAS GENERATOR AND DISCHARGE TANK

---



# INFLATOR MODEL FLOW CHART



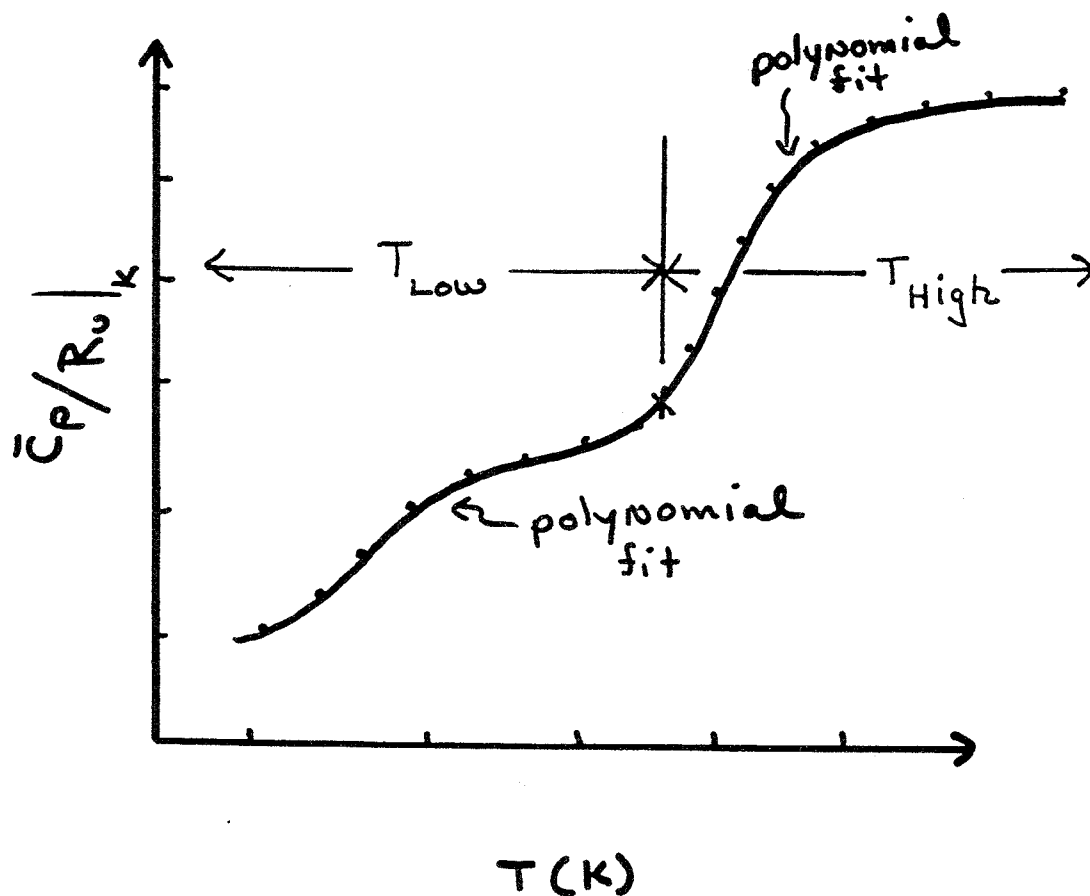


42-22	100 CYCLES, 1 L. ASH	5 SQUARE
42-23	200 CYCLES, 1 L. ASH	5 SQUARE
42-24	100 CYCLES, 1 L. WHIT	5 SQUARE
42-25	200 CYCLES, 1 L. WHIT	5 SQUARE

- A** **Low National Brand**

A graph showing the specific heat capacity ( $C_p$ ) as a function of temperature ( $T$  in K). The curve starts at 300 K and rises towards 2500 K. Horizontal dashed lines represent constant  $C_p$  values. Vertical double-headed arrows indicate the percentage error in  $C_p$  if a constant value is used:  $\sim 20\%$  error at 300 K and  $\sim 10\%$  error at 2500 K.

# SPECIFIC HEAT DATA



- gas ( $300 < T(K) < 5000$ )
- liquid ( $T_m < T(K) < T_v$ )
- solid (multiple phases) ( $T < T_m$ )  
- Debye temp.

# GAS-PHASE CHEMISTRY

---

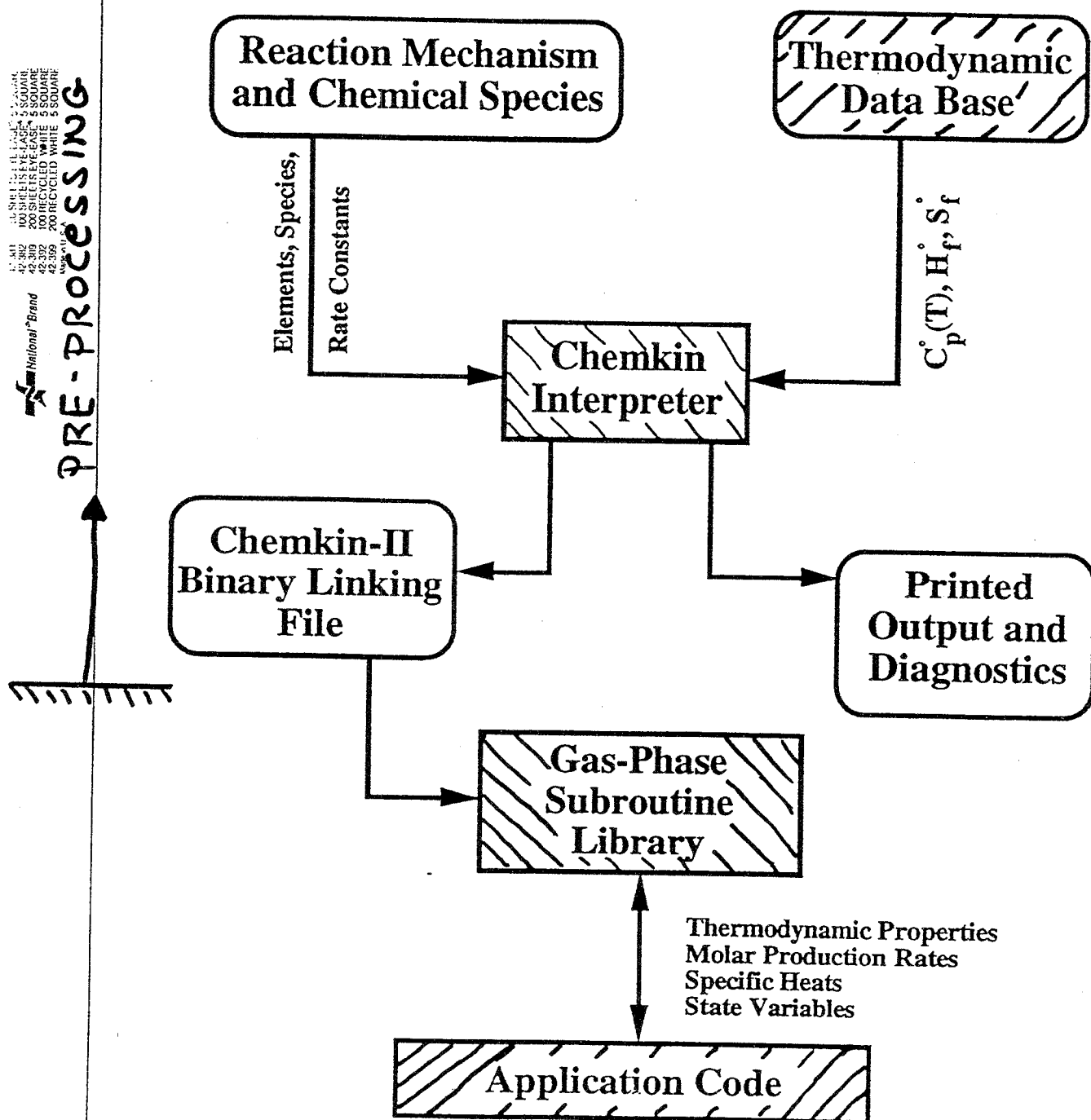
## <<<<<< GAS-PHASE REACTIONS >>>>>>

Rxn number Symbolic representation

---

1.  $\text{C} + \text{O}_2 \rightleftharpoons \text{CO} + \text{O}$
  2.  $\text{C} + \text{OH} \rightleftharpoons \text{CO} + \text{H}$
  3.  $\text{HCO} + \text{OH} \rightleftharpoons \text{H}_2\text{O} + \text{CO}$
  4.  $\text{HCO} + \text{M} \rightleftharpoons \text{H} + \text{CO} + \text{M}$
  5.  $\text{HCO} + \text{H} \rightleftharpoons \text{CO} + \text{H}_2$
  6.  $\text{HCO} + \text{O} \rightleftharpoons \text{CO} + \text{OH}$
  7.  $\text{HCO} + \text{O} \rightleftharpoons \text{CO}_2 + \text{H}$
  8.  $\text{HCO} + \text{O}_2 \rightleftharpoons \text{HO}_2 + \text{CO}$
  9.  $\text{CO} + \text{O} + \text{M} \rightleftharpoons \text{CO}_2 + \text{M}$
  10.  $\text{CO} + \text{OH} \rightleftharpoons \text{CO}_2 + \text{H}$
  11.  $\text{CO} + \text{O}_2 \rightleftharpoons \text{CO}_2 + \text{O}$
  12.  $\text{HO}_2 + \text{CO} \rightleftharpoons \text{CO}_2 + \text{OH}$
  13.  $\text{H}_2 + \text{O}_2 \rightleftharpoons 2\text{OH}$
  14.  $\text{O} + \text{OH} \rightleftharpoons \text{O}_2 + \text{H}$
  15.  $\text{O} + \text{H}_2 \rightleftharpoons \text{OH} + \text{H}$
  16.  $\text{H} + \text{O}_2 + \text{M} \rightleftharpoons \text{HO}_2 + \text{M}$
-

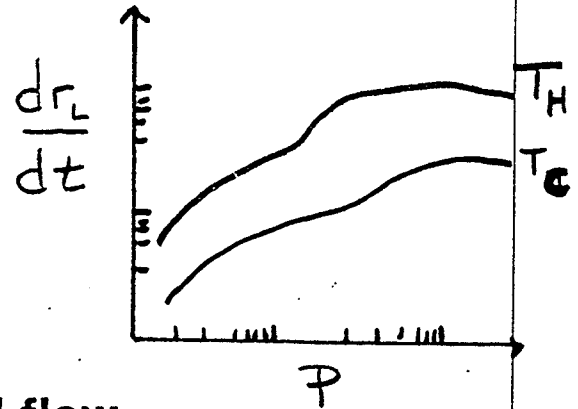
# CHEMKIN-II: FLOW CHART



# CONSTITUTIVE RELATIONS

- Burn-rate

$$\frac{dr_L}{dt} = b(T) \{a P^n\}$$

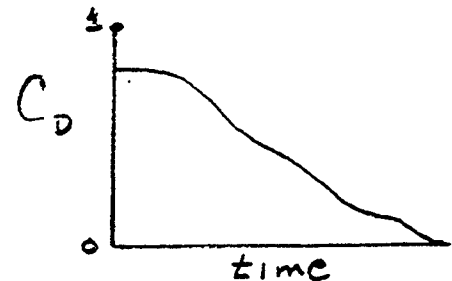


- Flow at the exit ports is choked-flow

$$\frac{dm_{ex}}{dt} = \frac{\Gamma A_{ex} P_i}{c_i} \times C_D \text{ (filter contamination)}$$

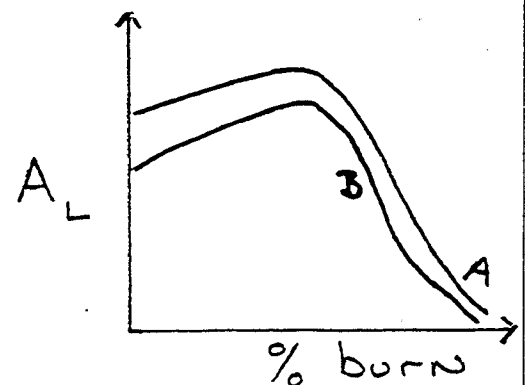
where  $\Gamma$  is a function of the specific heat ratio of the exit gas,

$$\Gamma = \gamma \left( \frac{2}{\gamma + 1} \right)^{\frac{\gamma+1}{2(\gamma-1)}}$$



- Instantaneous surface area (form function)

$A_L(t)$  = function of grain geometry



# PARTICLE FILTER

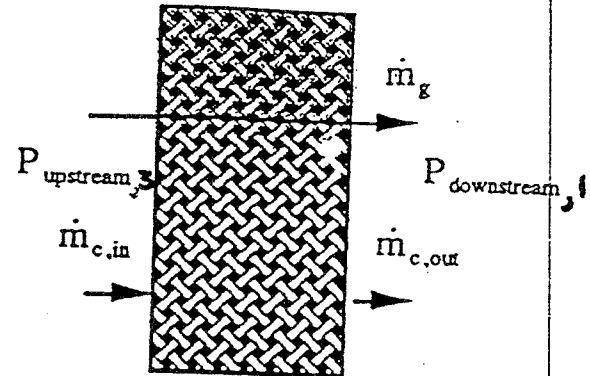
- FILTER FLOW LOSS

$$\dot{m}_{g,1,out} = A_{\text{filter}} C_{\mu,1} \left\{ \frac{2k}{k-1} P_1 \rho_1 \left[ \left( \frac{P_3}{P_1} \right)^{\frac{2}{k}} - \left( \frac{P_3}{P_1} \right)^{\frac{k+1}{k}} \right] \right\}^{\frac{1}{2}}$$

$\swarrow$   
f(filter design)

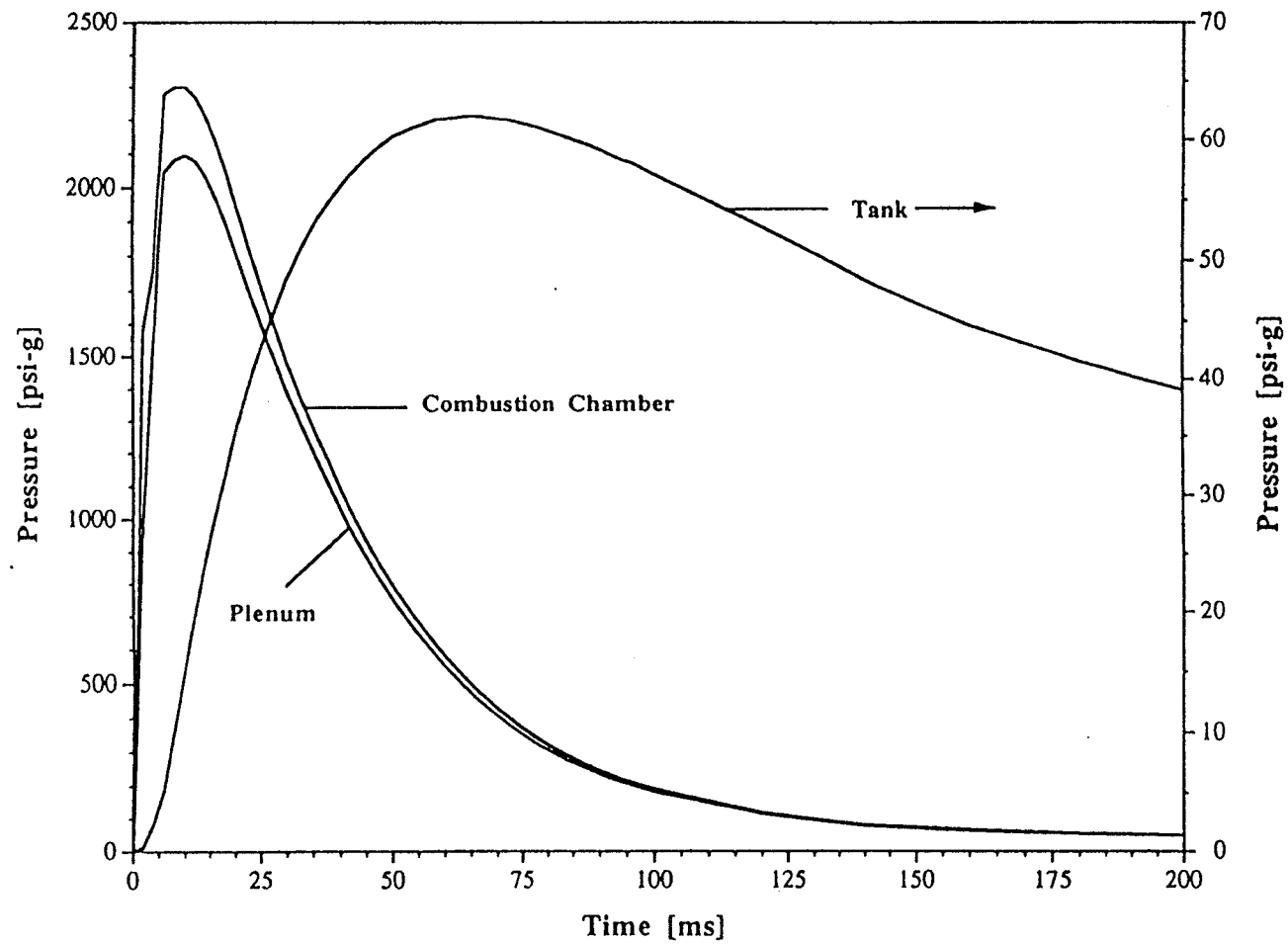
- FILTER COLLECTION EFFICIENCY

$$\dot{m}_{c,1,out} = \dot{m}_{g,1,out} \frac{\dot{m}_{c,1}}{\dot{m}_{g,1}}$$



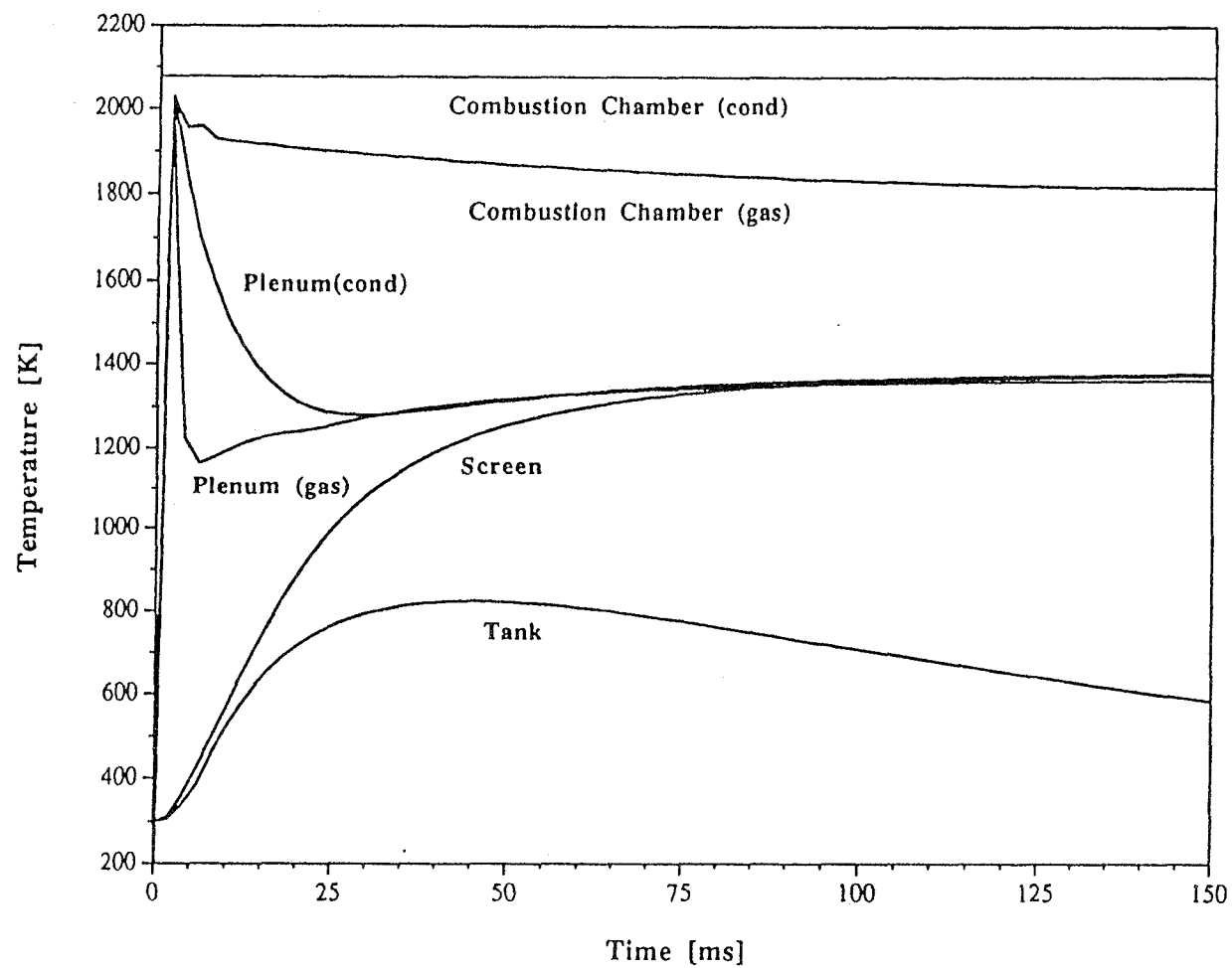
# RESULTS - COMPUTER SIMULATION

---



# RESULTS - COMPUTER SIMULATION

---

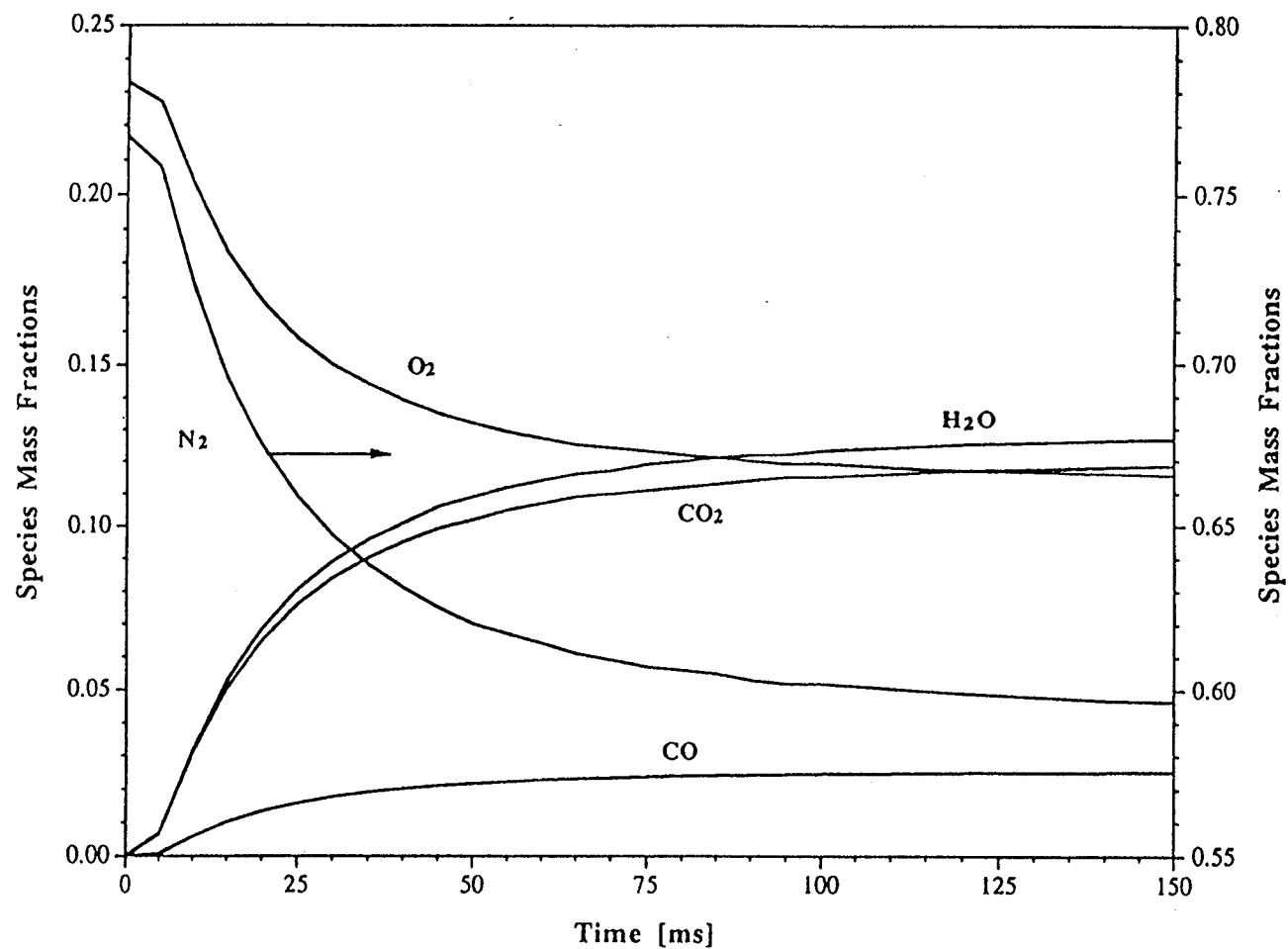


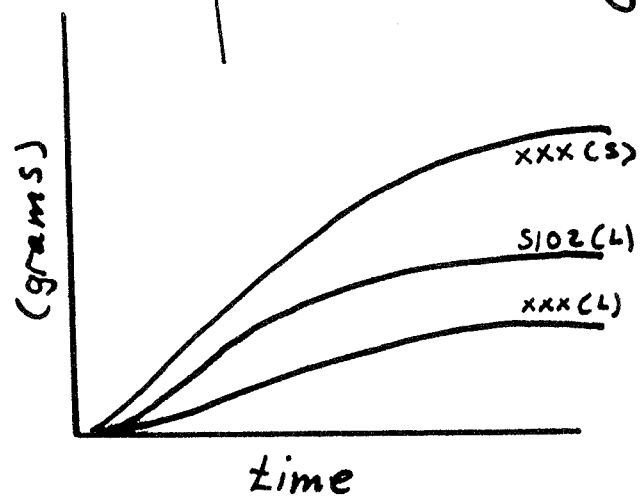
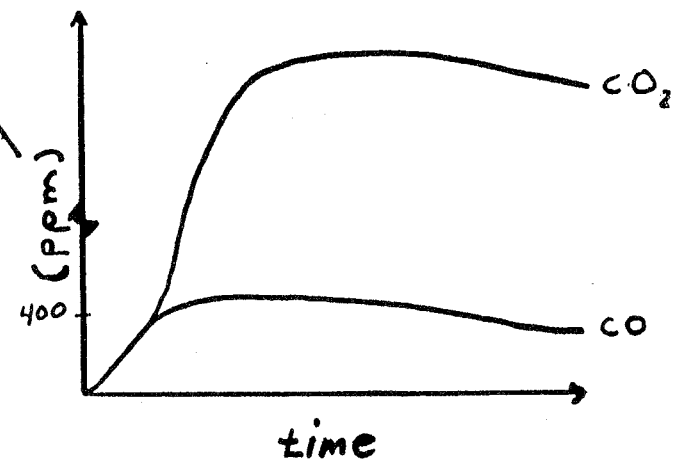


# RESULTS - COMPUTER SIMULATION

---

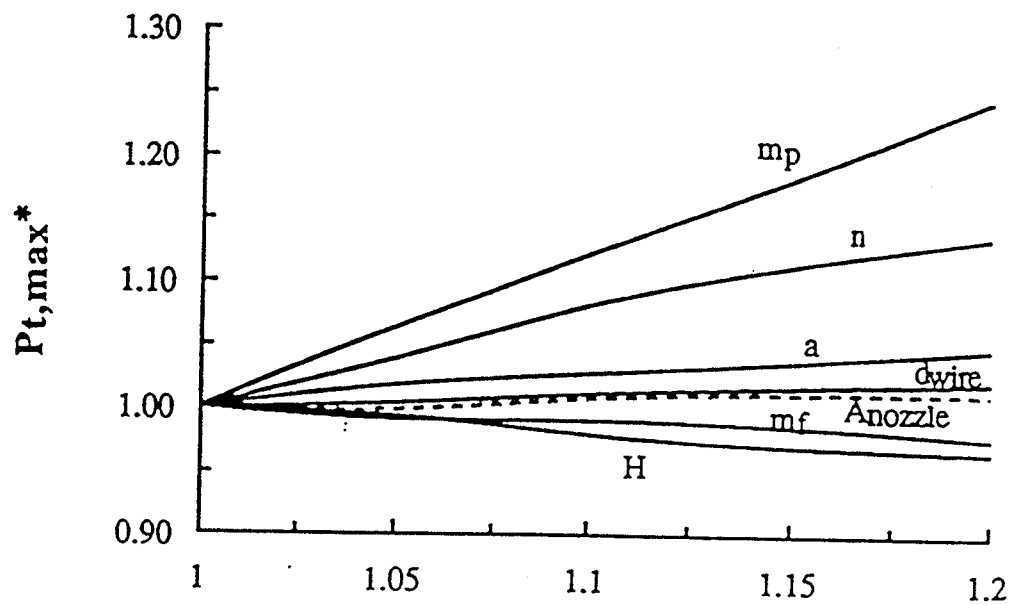
111





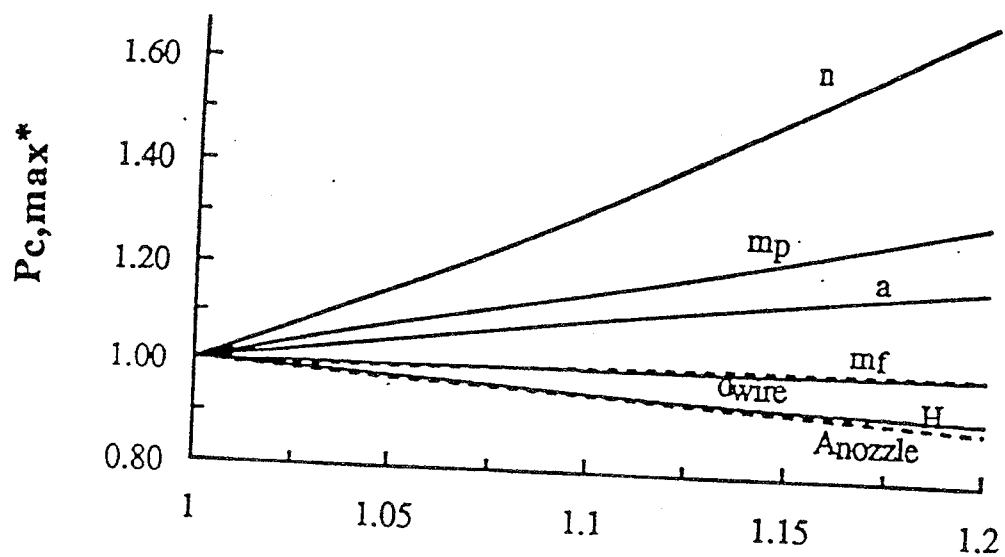
# RESULTS - SENSITIVITY STUDY

---



# RESULTS - SENSITIVITY STUDY

---



## **NECESSARY FOR MEANINGFUL INFLATOR SIMULATION PROGRAM**

---

- **DESCRIPTION OF PROPELLANT AND PRODUCTS  
CHEMICAL COMPOSITION**
  - **TEMPERATURE-DEPENDENT SPECIFIC HEAT  
FUNCTIONS FOR ALL POSSIBLE SPECIES**
  - **PRECISE SOLID PHASE PROPERTIES (V, DENSITY)**
  - **SURFACE REGRESSION RATE (  $= F(P,T)$  )**
  - **SURFACE/VOLUME RATIO OF PROPELLANT DURING  
BURN**
  - **IGNITION SEQUENCE OF THE PROPELLANT  
(COATING, SQUIB SIZE, TEMPERATURE, ETC.)**
  - **FRACTURE OF GRAINS DURING RAPID  
PRESSURIZATION**
  - **SOLID-PHASE THERMAL PROPERTIES (MODEL SLAG  
FORMATION)**
  - **NOZZLE OPENING PROCESS (INCLUDED MULTIPLE  
NOZZLE SIZES TO AVOID SADDLING EFFECT)**
  - **HEAT LOSS TO SCREENS**
  - **DYNAMIC MASS-FLOW DISCHARGE COEFFICIENTS**
  - **DEVELOPMENT OF EXPERIMENTAL PLAN IN PARALLEL  
WITH MODEL DEVELOPMENT**
-

# EXPERIMENTAL REQUIREMENTS

---

- **DESCRIPTION OF PROPELLANT**
    - chemical composition
    - grain geometry
    - burn-rate function
  - **ANALYSIS OF SPECIES REMAINING IN THE INFLATOR AFTER FIRING**
  - **DYNAMIC PRESSURE MEASUREMENTS IN:**
    - inflator body
    - discharge tank
  - **AFTER-FIRING INSPECTION OF HARDWARE FOR CONDENSED PARTICLES**
  - **INDEPENDENT STUDIES OF THE FILTER COLLECTION EFFICIENCY**
  - **INDEPENDENT STUDIES OF THE PROPELLANT IGNITION SEQUENCE**
-

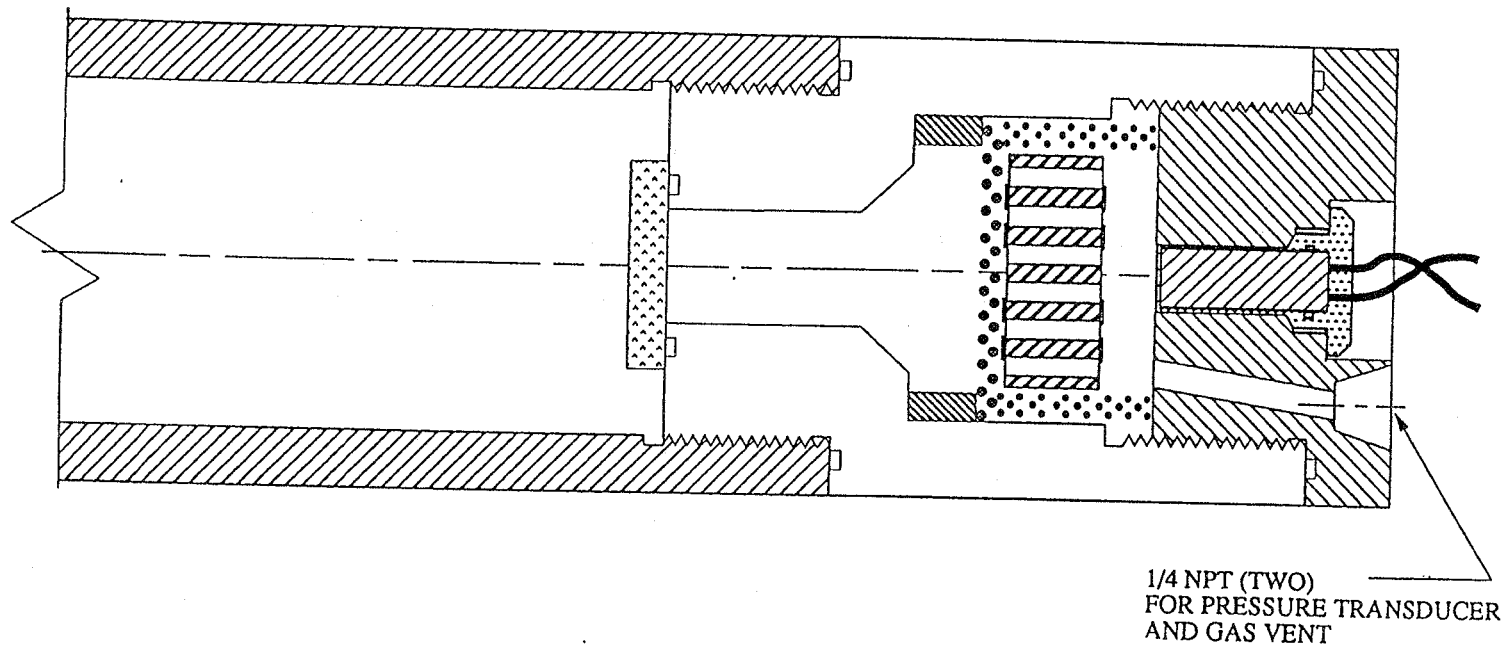
# **PROPELLANT CONCERNS**

---

- **PRODUCT CHEMICAL COMPOSITION**
    - tank gas
    - tank particulates
    - inflator slag (multi-phase mixture)
  - **LIFE (>15 years)**
  - **DISPOSAL**
  - **PROPELLANT OUTPUT**
    - hot vs. cold firing
    - squib can fracture propellant grains
  - **LABORATORY COMBUSTION STUDIES SHOULD REPLICATE ACTUAL GAS GENERATOR OPERATING ENVIRONMENT**
    - high confinement (solids loading)
    - pressure variations (14.7 - 4,000 psi)
    - possible slag build-up
    - flame spreading
-

# COMBUSTION TEST APPARATUS

---





# IGNITION CONCERNS

---

- **ACTION TIME**

- hot vs. cold firing
- uniform performance of "similar" squibs
- some "good" gas-generating propellants require accelerant coatings

- **IGNITOR OUTPUT**

- hot vs. cold firing
- uniformity in performance of "similar" squibs
- can fracture propellant grains

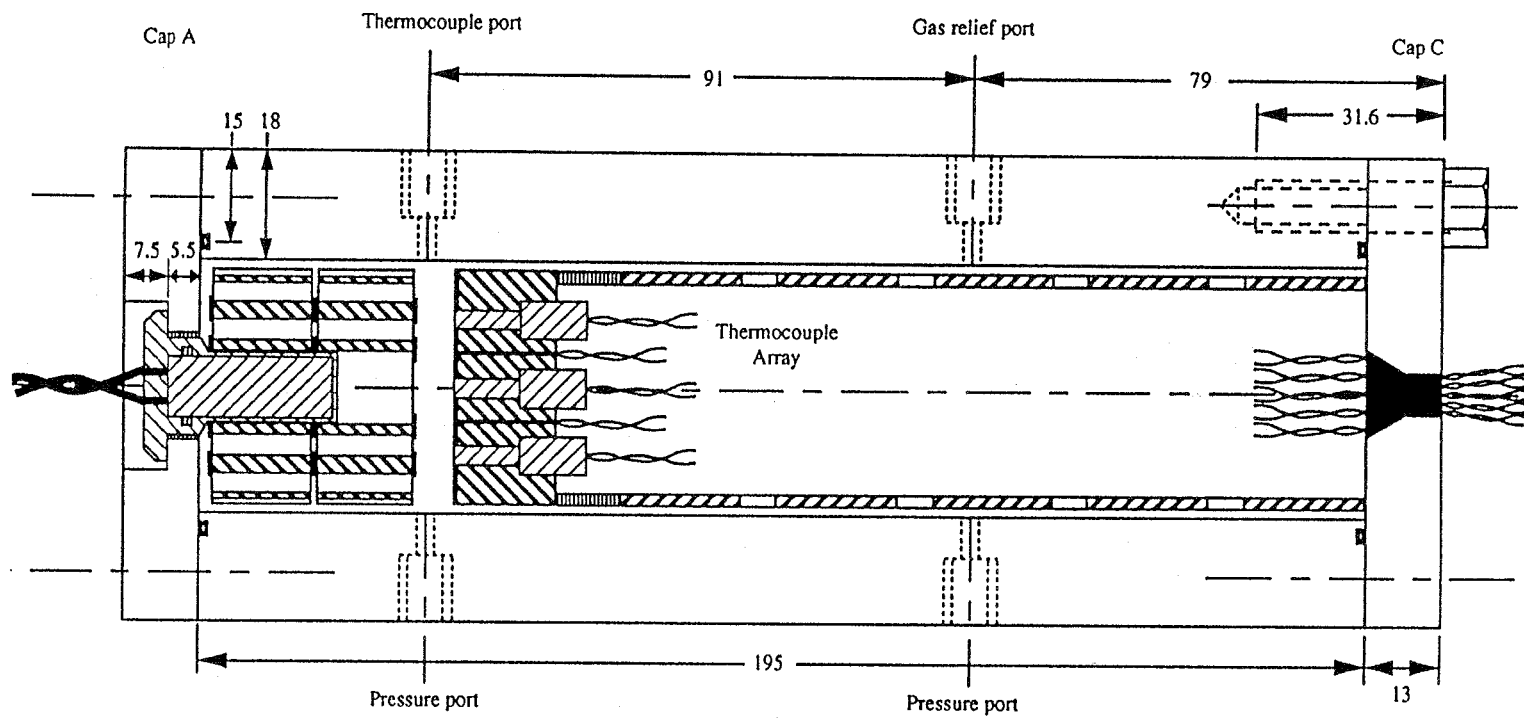
- **IGNITOR LIFE**

- uniform performance after storage

- **INDEPENDENT STUDIES OF IGNITOR AND PROPELLANT IGNITION SEQUENCE ARE NECESSARY UNDER ALL OPERATING CONDITIONS**

---

# IGNITION TEST APPARATUS



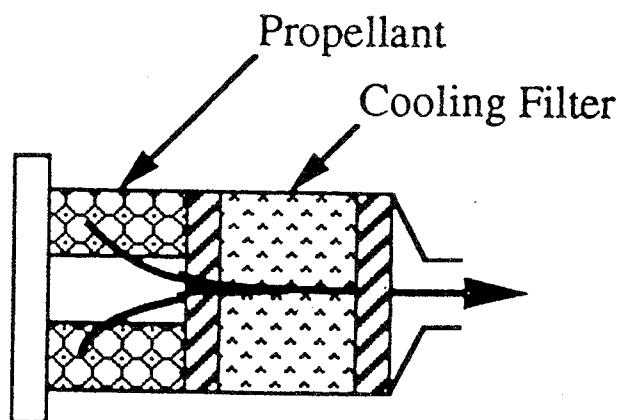
# CONCLUSIONS

---

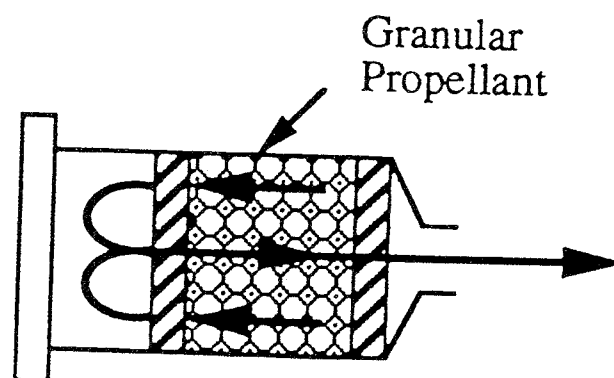
- **COMPREHENSIVE GAS GENERATOR MODEL WAS DEVELOPED**
  - **MODEL HAS BEEN APPLIED TO**
    - **conventional pyrotechnic inflators**
    - **hybrid inflators**
  - **AGREEMENT WITH DATA IS EXCELLENT**
  - **MODEL IS A USEFUL TOOL FOR DESIGN AND DEVELOPMENT OF:**
    - **new inflators (material properties, size, etc.)**
    - **new pyrotechnic compositions**
    - **propellant grain modifications**
    - **ignitors**
    - **new filter designs**
  - **EXPERIENCE SHOWS THAT A RELIABLE EXPERIMENTAL DATABASE IS ESSENTIAL**
  - **WE RECOMMEND THAT SOLID PROPELLANT FIRE EXTINGUISHMENT PROGRAM FOLLOW SAME METHODOLOGY**
-

# ALTERNATIVE DESIGNS

---



a.) Standard Scheme



b.) Self-cooling Scheme

---

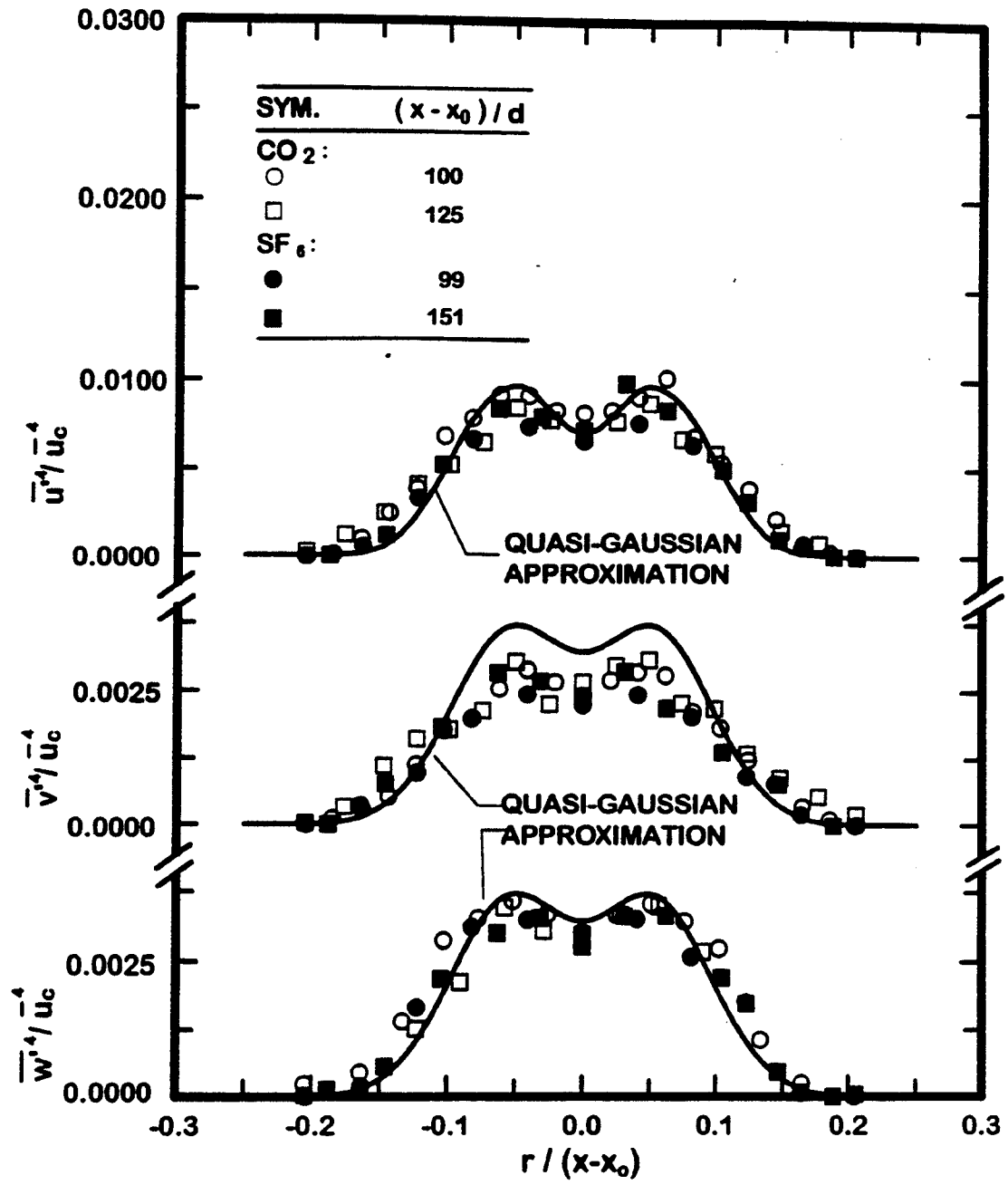


Fig. 10 Radial profiles of  $\bar{u}'^4$ ,  $\bar{v}'^4$  and  $\bar{w}'^4$  within self-preserving buoyant turbulent plumes.

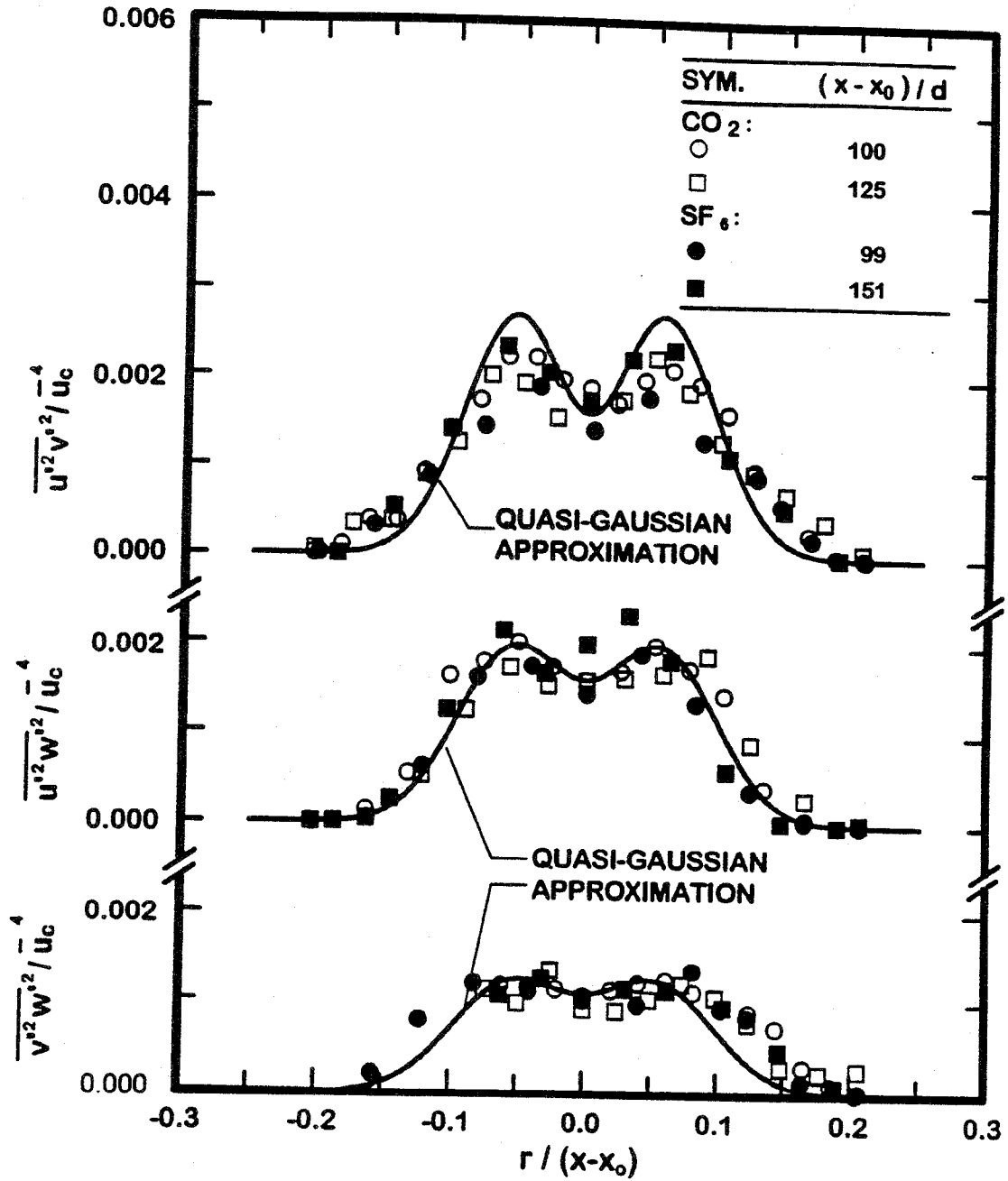


Fig. 11 Radial profiles of  $\overline{u'^2 v'^2}$ ,  $\overline{u'^2 w'^2}$  and  $\overline{v'^2 w'^2}$  within self-preserving buoyant turbulent plumes.

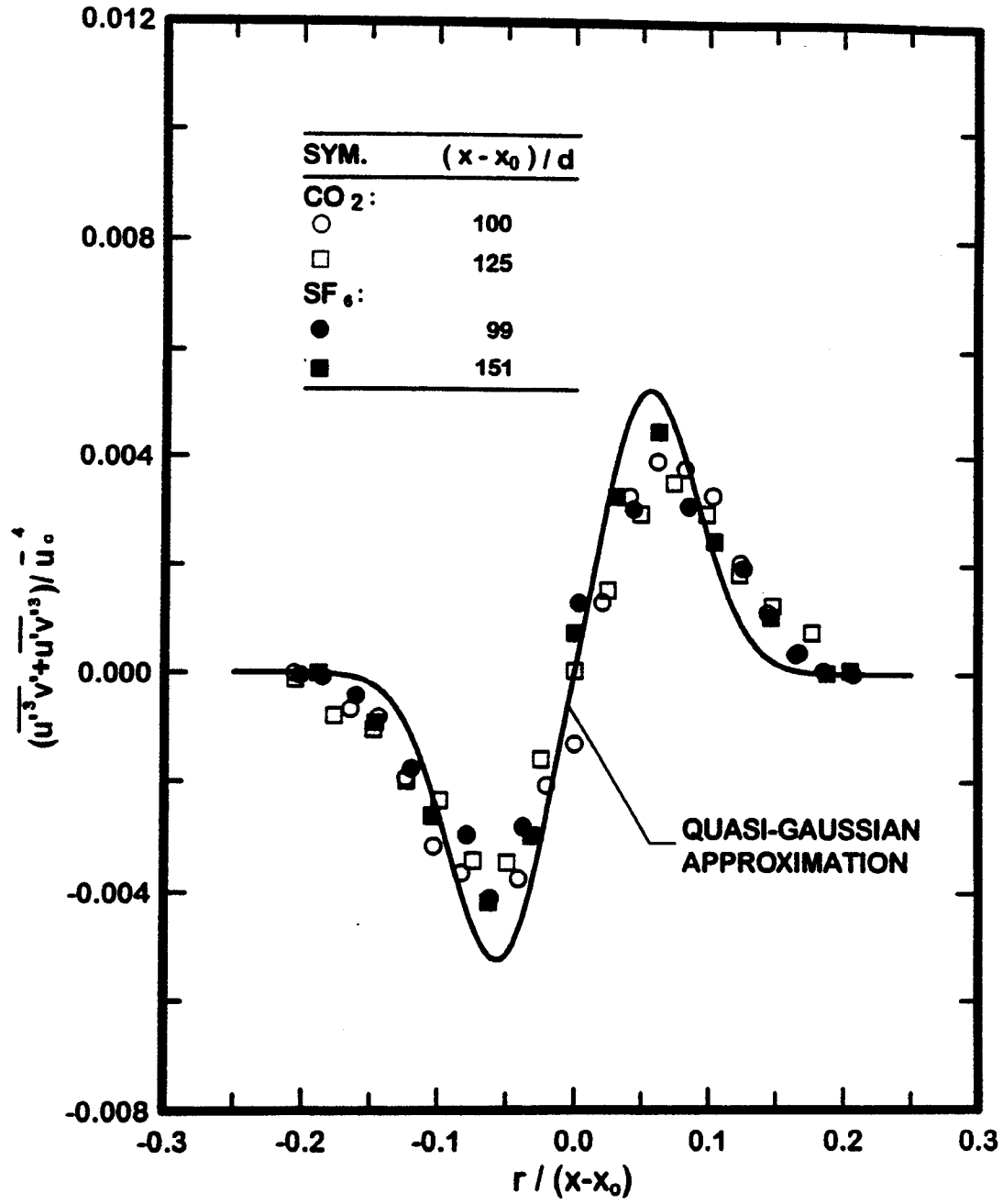


Fig. 12 Radial profiles of  $\overline{(u'^3 v' + u' v'^3)} / \bar{u}_0^4$  within self-preserving buoyant turbulent plumes.

### 2.3 Moments of Velocity/Mixture-Fraction Fluctuations

Measurements of combined velocity/mixture-fraction statistics will be considered next. The three lowest-order statistics of this type are the turbulent mass fluxes,  $\overline{f'u'}$ ,  $\overline{f'v'}$  and  $\overline{f'w'}$ ; measurements of these parameters within the self-preserving region are illustrated in Fig. 13. Typical of other parameters observed for present test conditions, these results clearly exhibit self-preserving behavior. The tangential turbulent mass flux,  $\overline{f'w'} = 0$ , for an axisymmetric flow; present measurements of this parameter are seen to satisfactorily agree with this requirement as well. The radial turbulent mass flux,  $\overline{f'v'}$ , is the most important mass transport parameter in the present boundary-layer-like flow. Analogous to the Reynolds stress illustrated in Fig. 6, this parameter has  $\overline{f'v'} = 0$  at  $r = 0$  due to symmetry, and then increases to a maximum value near  $r/(x-x_0) = 0.06$  (in the absolute sense) before decreasing to zero once again at large  $r$ . Finally,  $\overline{f'u'}$ , exhibits rather large values in the present flows, somewhat analogous to  $\overline{u'^2}$  discussed earlier. In fact, the correlation coefficient  $(\overline{f'u'},/(\overline{f'u'})_c \approx 0.7$  which is quite large. As discussed earlier, this behavior comes about due to the intrinsic instability of plumes where large values of  $f$  provide a corresponding potential for large values of  $u$  due to effects of buoyancy. This behavior has been recognized for some time, see George et al. (1977). Another result of the large correlation of streamwise turbulent mass flux is that this flux is appreciable (typically 15%) in comparison to the mean mass flux, and must be considered for an accurate prescription of conservation of mixture fraction (or buoyancy flux) for the flow.

The consistency of the measured values of radial turbulent mass flux with other measurements of mean and fluctuating quantities was evaluated similar to the conservation of mass considerations for  $\bar{v}$ , and the conservation of momentum considerations for the Reynolds stress, discussed earlier. Imposing the approximations of a thin, boundary-layer-like plume flow, self-preserving conditions so that density variations are small, and neglecting molecular mass diffusion in comparison to turbulent mass diffusion, there results:

$$\bar{u}\partial\bar{f}/\partial x + \bar{v}\partial\bar{f}/\partial r = -(\partial/\partial x(\overline{f'u'}) + \partial/\partial r(r\overline{f'v'})/r) \quad (23)$$

Then, integrating equation (23), both ignoring and considering the streamwise turbulent mass flux ( $\overline{f'u'}$ ), using the present correlations for  $\bar{u}$ ,  $\bar{v}$  and  $\bar{f}$  in the self-preserving portion of the flow, yields the two predictions for  $\overline{f'v'}$  illustrated in Fig. 13. In general, including  $\overline{f'u'}$  does not have a large effect on the predicted value of  $\overline{f'v'}$ ; this follows even though  $\overline{f'u'}$  is large near the axis because  $\overline{f'u'}$  is small near the axis due to the



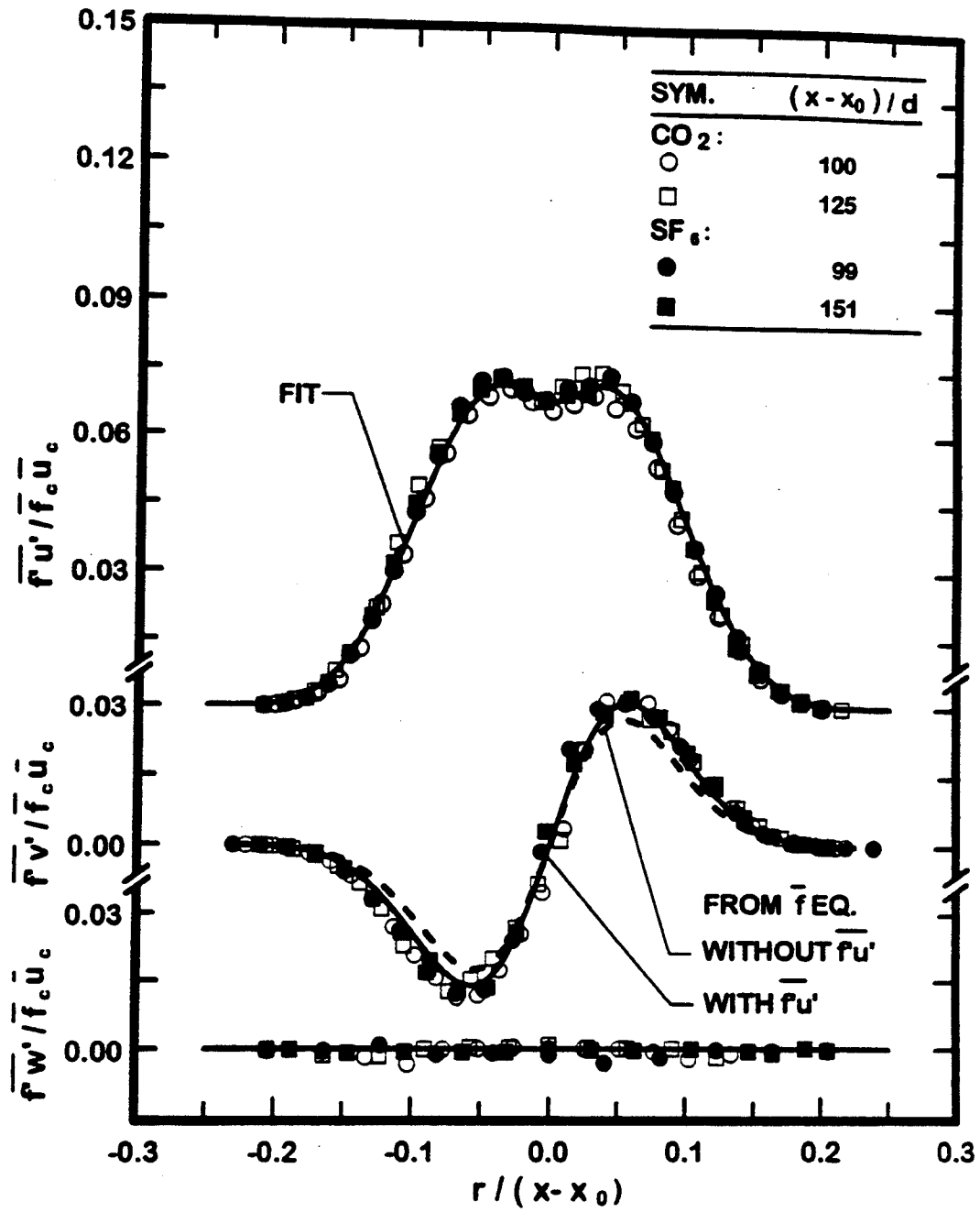


Fig. 13 Radial profiles of turbulent mass fluxes within self-preserving buoyant turbulent plumes.

requirements of symmetry. Thus, both predictions are in good agreement with present measurements which helps confirm the internal consistency of the measurements; nevertheless, the more complete version of the integration, which accounts for effects of  $\overline{f'u'}$ , clearly is in best agreement with the measurements.

The gradient diffusion approximation is commonly made for simplified models of turbulent mixing, which implies the following relationships for the radial and streamwise turbulent mass fluxes:

$$\overline{f'v'} = -(v_t/\sigma_T) \partial \bar{f} / \partial r, \quad \overline{f'u'} = -(v_t/\sigma_T) \partial \bar{f} / \partial x \quad (24)$$

where  $v_t$  is an effective turbulence kinematic viscosity and  $\sigma_T$  is an effective turbulence Prandtl/Schmidt number. The present results in the self-preserving region were used to test the gradient-diffusion hypotheses embodied by equation (24). It was found that the radial flux was reasonably satisfied by the gradient diffusion approximation, which is helpful for modeling the present relatively simple flow because the radial flux dominates turbulent mass transfer. On the other hand, the streamwise turbulent mass flux exhibited counter-gradient diffusion (which implies an unphysical negative value  $v_t$ ) near the edge of the flow. This clearly implies the absence of the isotropy of  $v_t$  implied by equation (24). This counter-gradient diffusion deficiency is not very important for the present boundary layer flow, where streamwise turbulent transport is ignored in any event; nevertheless, this deficiency does raise concerns about the use of simple gradient diffusion hypotheses for the more complex turbulent flows of interest for practical fire environments. Thus, the observation of counter-gradient diffusion in the streamwise direction provides strong motivation for considering higher-order closures that avoid the gradient diffusion hypotheses.

Simple gradient diffusion hypotheses, with constant turbulent Prandtl/Schmidt numbers, are even problematical for transport in the radial direction of the present buoyant turbulent plume flow. This behavior was established by considering the gradient diffusion hypothesis for the Reynolds stress  $\overline{u'v'}$ , as follows:

$$\overline{u'v'} = -v_t \partial \bar{u} / \partial r \quad (25)$$

Then combining equations (24) and (25), and solving for  $\sigma_T$ , yields:

$$\sigma_T = (\overline{u'v'}/\overline{f'v'}) (\partial \bar{f} / \partial r) / (\partial \bar{u} / \partial r) \quad (26)$$

The present measurements of  $\overline{u'v'}$ ,  $\overline{f'v'}$ ,  $\bar{f}$  and  $\bar{u}$  were used to find  $\sigma_T$  as a function of radial position in the self-preserving region of the flow. These results are plotted in Fig. 14. In this case, the measurements exhibit significant scatter, which is unavoidable because finding  $\sigma_T$  from equation (26) involves four measurements, two of which are gradients. Keeping this difficulty in mind, the results indicate crude self-preserving behavior for  $\sigma_T$ . On the other hand,  $\sigma_T$  approaches 0.9 at  $r = 0$  but then progressively decreases to  $\sigma_T \approx 0.1$  (except for a few outlying points near the edge of the flow where present experimental uncertainties are large). Clearly, this behavior departs significantly from the common assumption of  $\sigma_T = 0.7$  or  $0.9$  across the flow width, see Lockwood and Naguib (1975), Lumley (1978), Taulbee (1992), Shabbir and Taulbee (1990) and Pivovarov et al. (1992). Thus, the difficulty with  $\sigma_T$  also suggests that higher-order closures are needed if flow development effects are to be represented accurately in buoyant turbulent flows.

The turbulent diffusion terms in the scalar flux and scalar variance equations contain a number of non-zero triple moments, e.g.,  $\overline{f'^2u'}$ ,  $\overline{f'^2v'}$ ,  $\overline{f'u'^2}$ ,  $\overline{f'v'^2}$ ,  $\overline{f'w'^2}$  and  $\overline{f'u'v'}$ . Terms of this type also appear at lower order when the governing equations are formulated using mass-weighted (Favre) averages, as advocated by Bilger (1976) for flame environments. Modeling procedures for Favre-averaged quantities are discussed by Bilger (1976), Malin and Younis (1990), Shih et al. (1987), Lumley (1978), and references cited therein. Present measurements of these moments are illustrated in Figs. 15-17, along with fits used in budgets of turbulence quantities to be discussed later. Similar to the other variables, these results exhibit self-preserving behavior within the present flows, while terms that should be zero due to symmetry, e.g.,  $\overline{f'^2w'}$ , properly yield small values. Other measurements of these properties are rare, about all that can be said is that there are qualitative similarities between present measurements and those of Panchapakesan and Lumley (1993) for a transitional buoyant plume. More study will be required to interpret these results in terms of higher-order closures for buoyant turbulent flows, see Panchapakesan and Lumley (1993) for initial work along these lines.

Similar to fourth-order velocity fluctuation moments, discussed earlier, combined fourth-order mixture fraction/velocity moments are needed to close the governing equations for third-order mixture fraction/velocity moments. Several of these moments were measured in the self-preserving region and are plotted as follows:  $\overline{f'u'^3}$ ,  $\overline{f'v'^3}$  and  $\overline{f'w'^3}$  in Fig. 18;  $\overline{f'u'w'^2}$ ,  $\overline{f'u'^2w'}$  and  $\overline{f'^2u'w'}$  in Fig. 19;  $\overline{f'^2u'v'}$ ,  $\overline{f'u'^2v'}$  and  $\overline{f'u'v'^2}$  in Fig. 20;  $\overline{f'^3u'}$ ,  $\overline{f'^3v'}$  and  $\overline{f'^3w'}$  in Fig. 21; and  $\overline{f'^2u'^2}$ ,  $\overline{f'^2v'^2}$  and  $\overline{f'^2w'^2}$  in Fig. 22. All these results exhibit self-preserving behavior over the present test range, within experimental uncertainties. In addition, moments that should be zero due to symmetry,

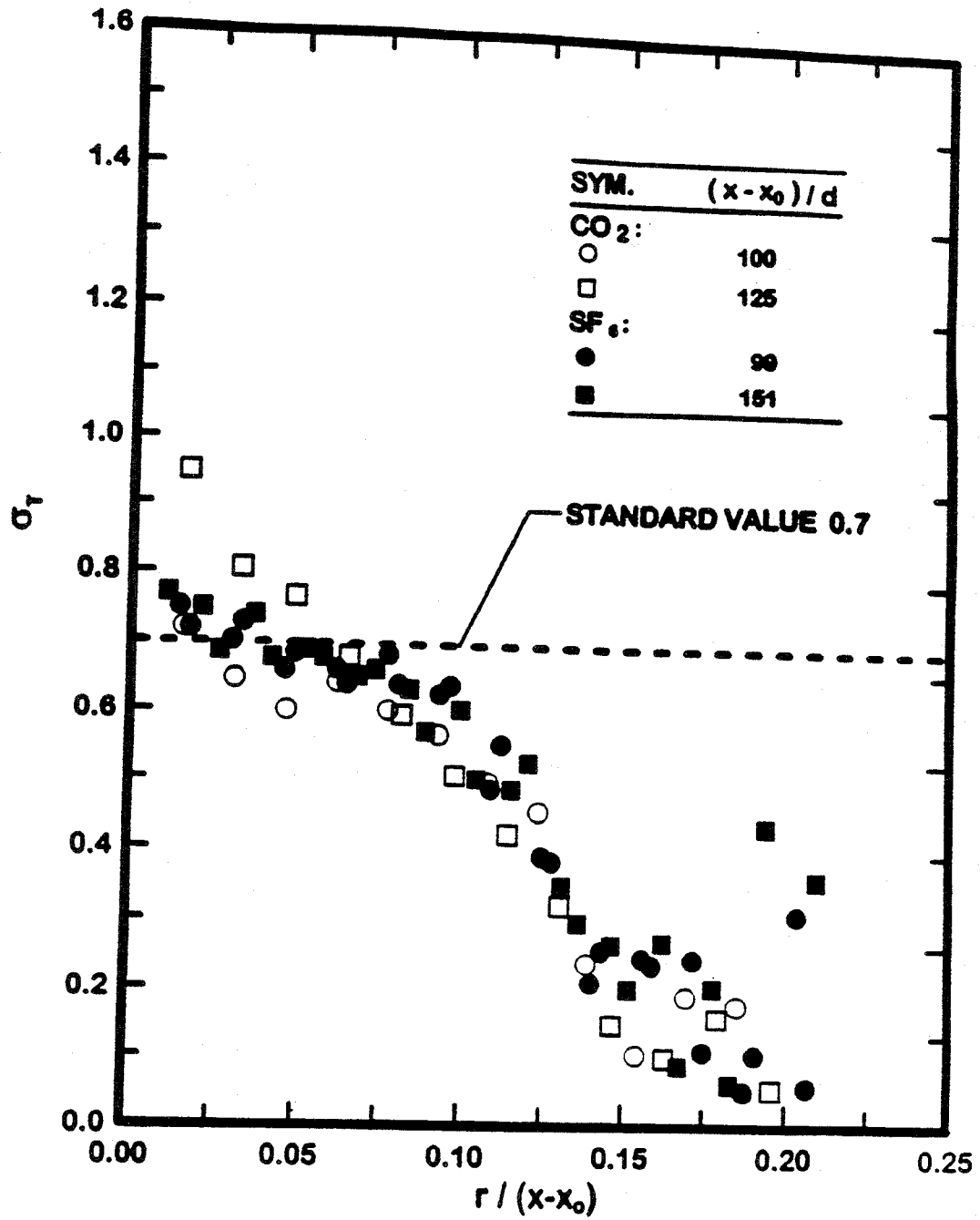


Fig. 14 Radial profiles of turbulent Prandtl/Schmidt numbers within self-preserving buoyant turbulent plumes.

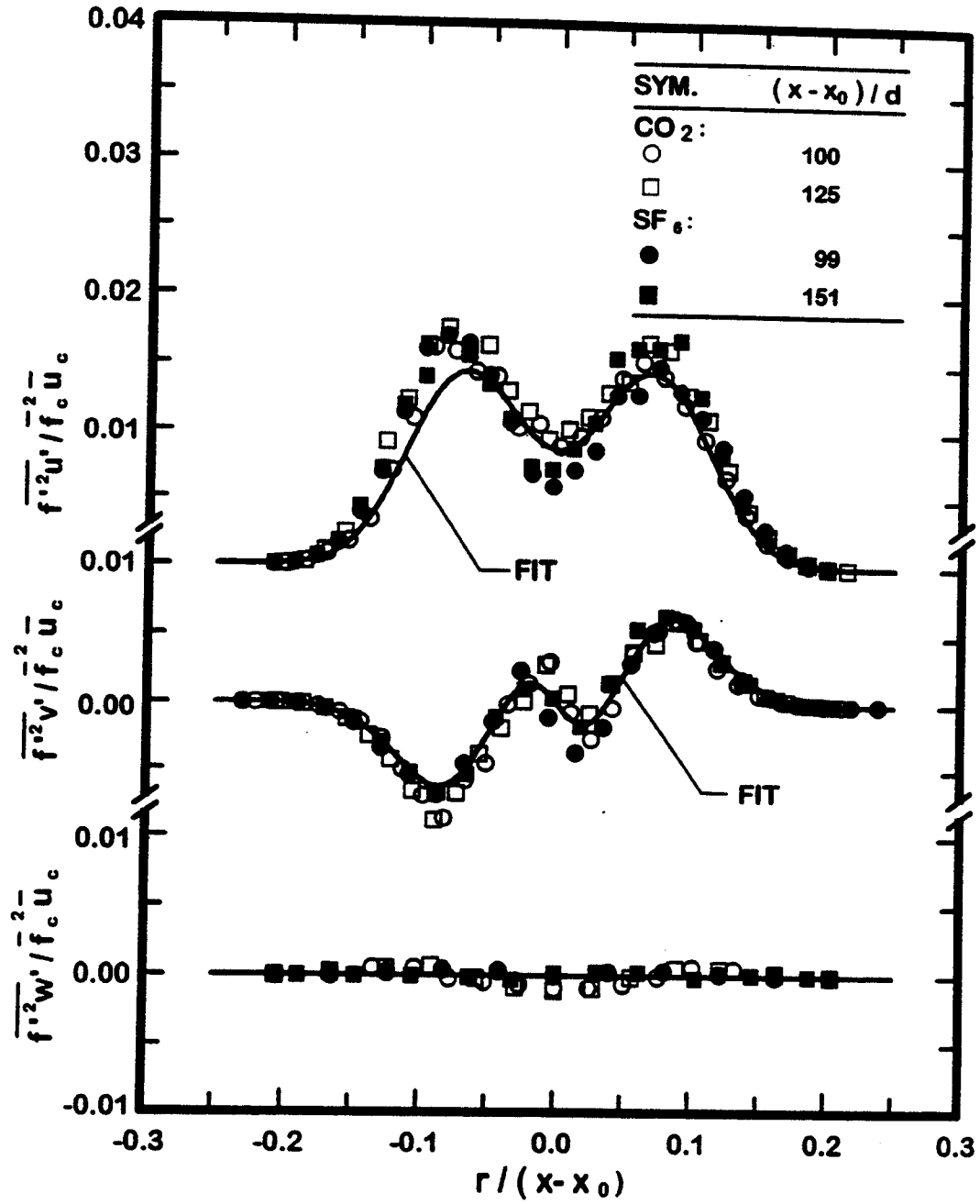


Fig. 15 Radial profiles of  $\overline{f'^2 u'}$ ,  $\overline{f'^2 v'}$  and  $\overline{f'^2 w'}$  within self-preserving buoyant turbulent plumes.

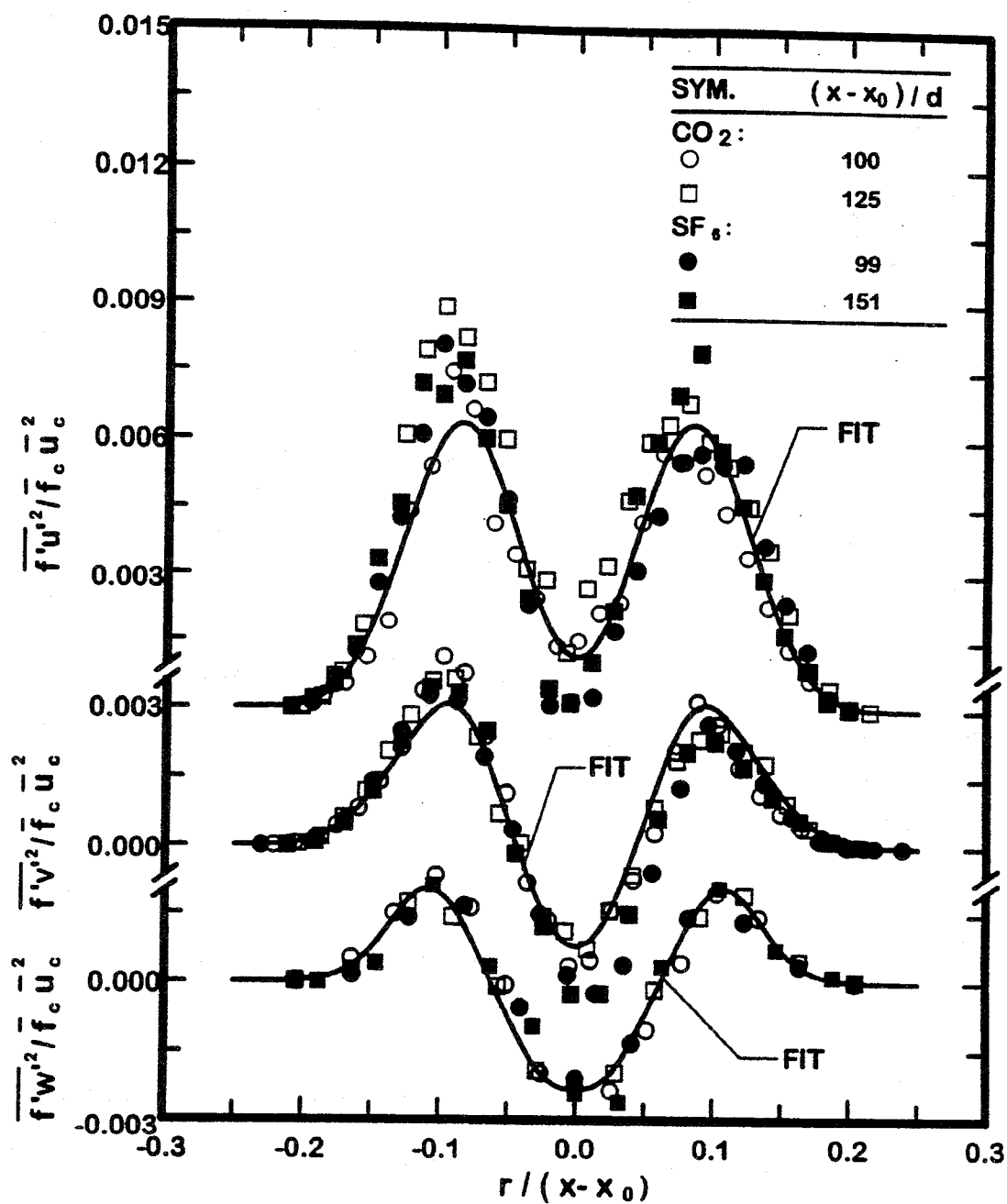


Fig. 16 Radial profiles of  $\overline{f'u'^2}$ ,  $\overline{f'v'^2}$  and  $\overline{f'w'^2}$  within self-preserving buoyant turbulent plumes.

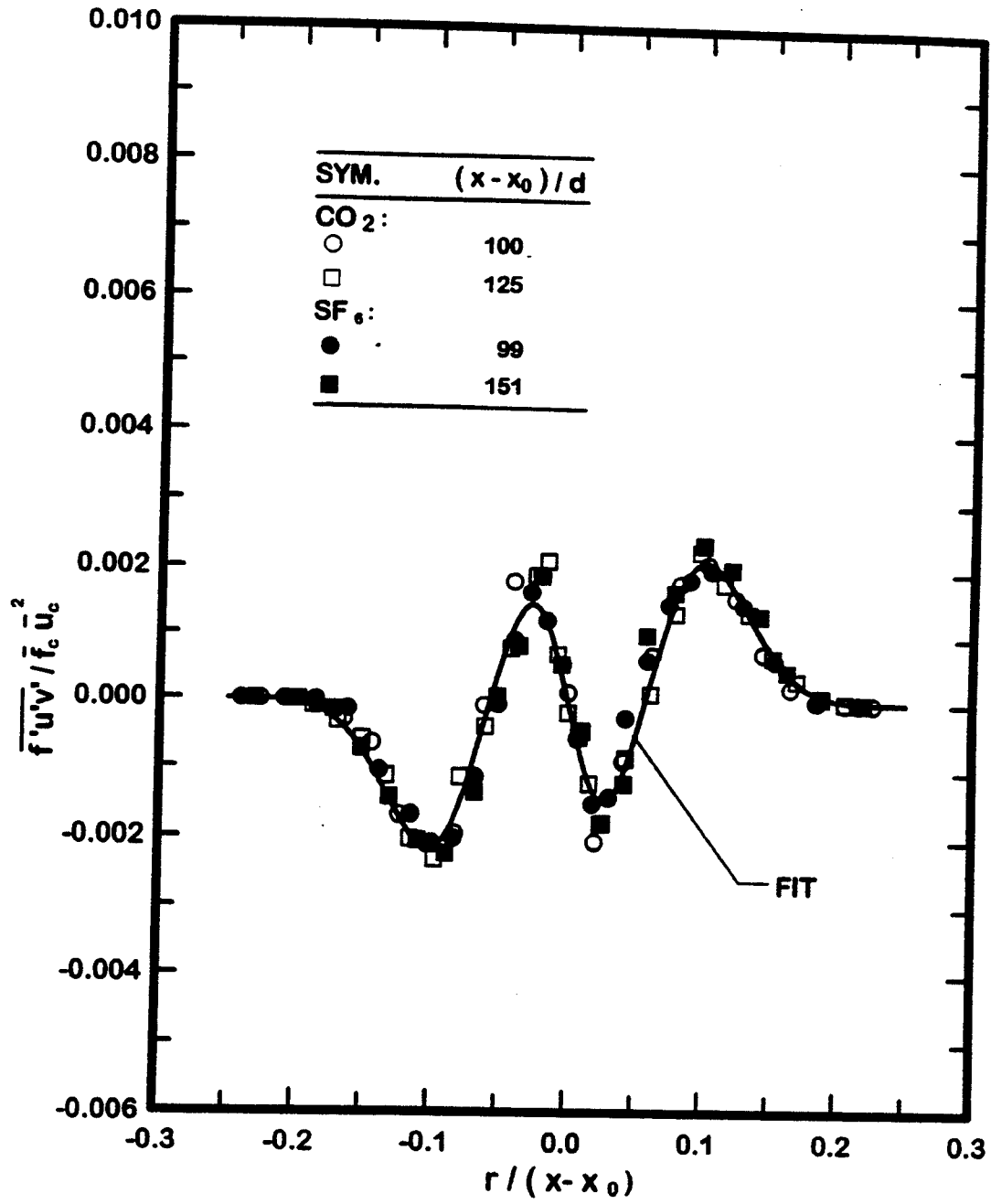


Fig. 17 Radial profiles of  $\overline{f'u'v'}$  within self-preserving buoyant turbulent plumes.

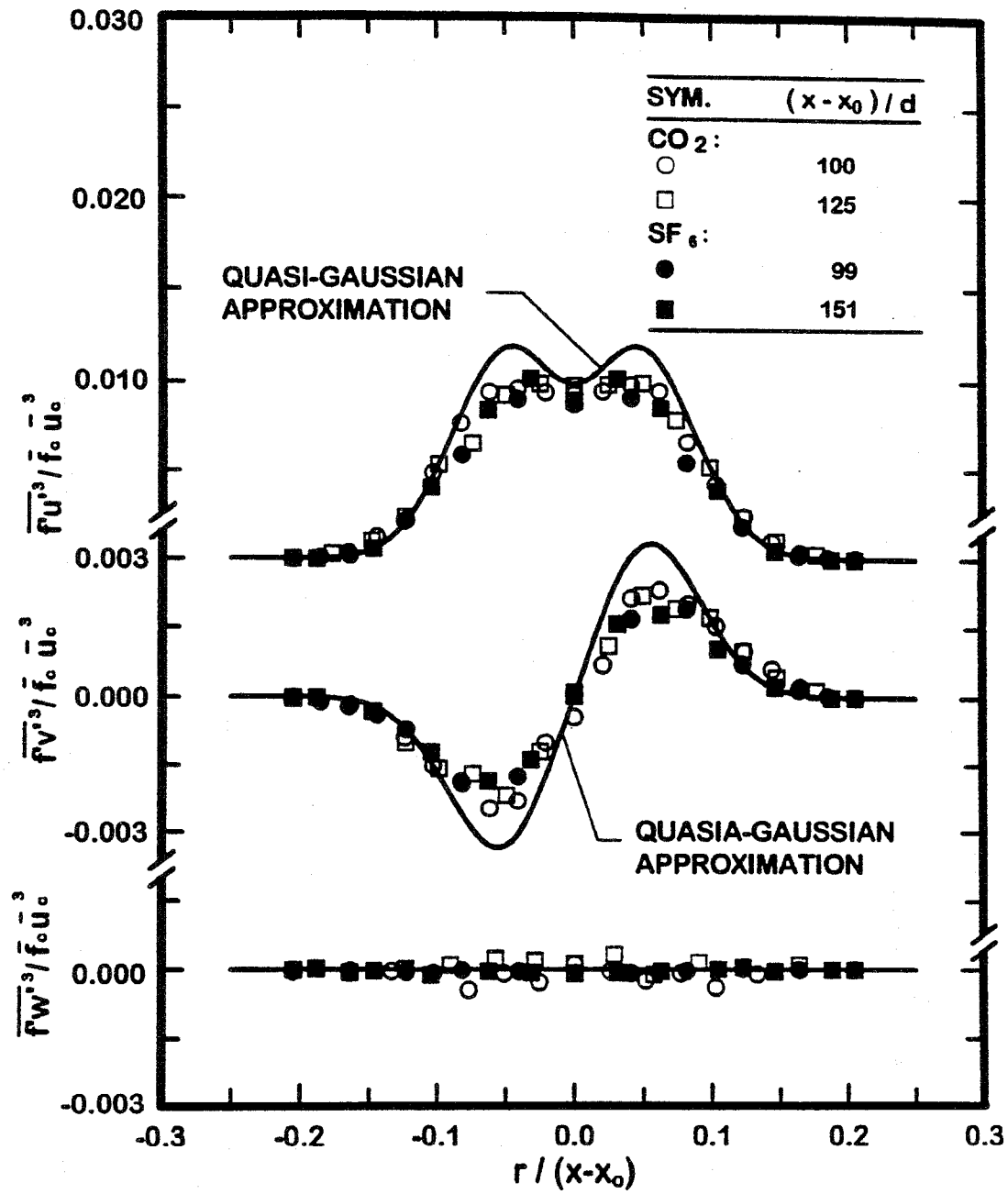


Fig. 18 Radial profiles of  $\overline{f'u'^3}$ ,  $\overline{f'v'^3}$  and  $\overline{f'w'^3}$  within self-preserving buoyant turbulent plumes.



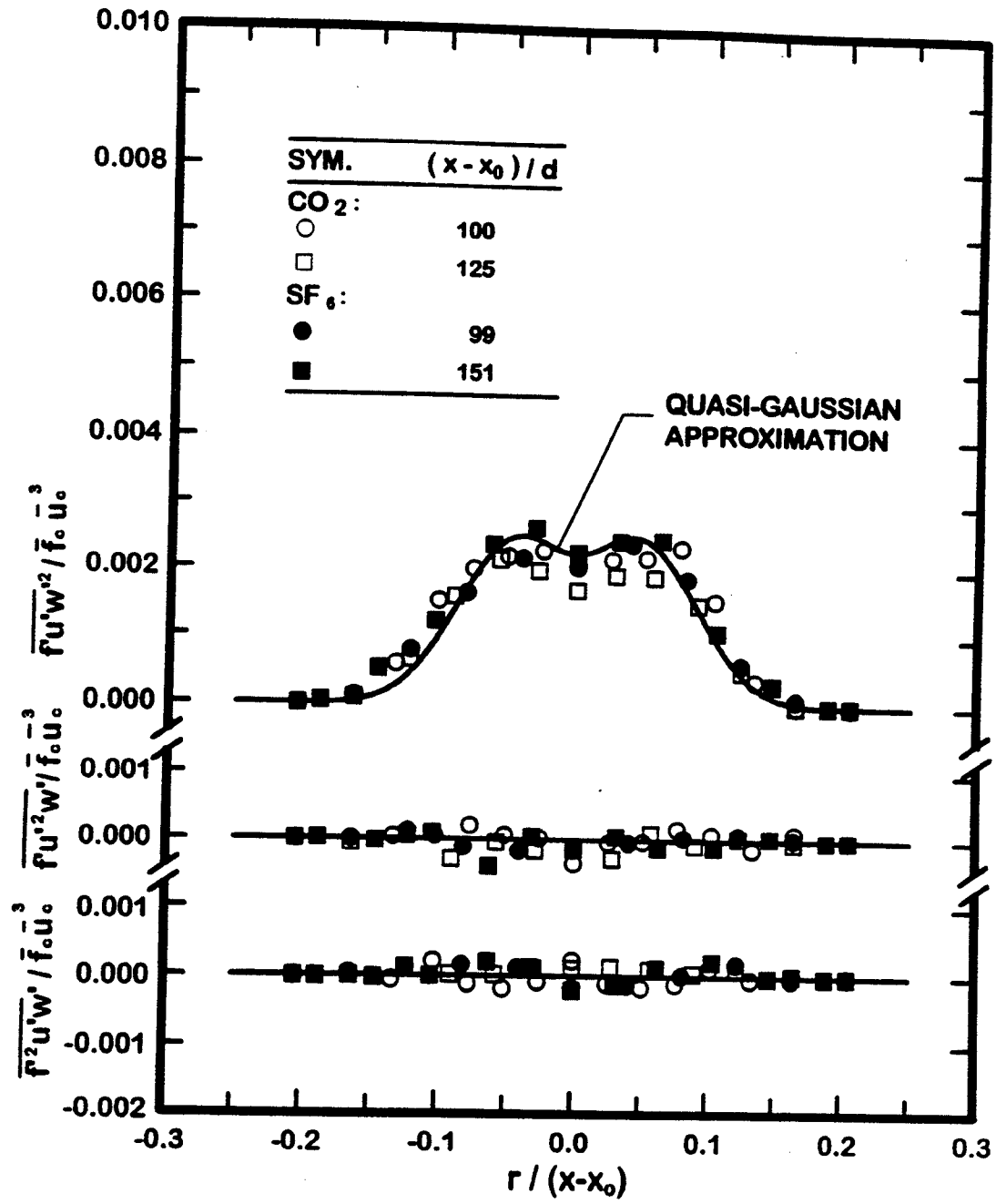


Fig. 19 Radial profiles of  $\overline{f'u'w'^2}$ ,  $\overline{f'u'^2w'}$  and  $\overline{f'^2u'w'}$  within self-preserving buoyant turbulent plumes.

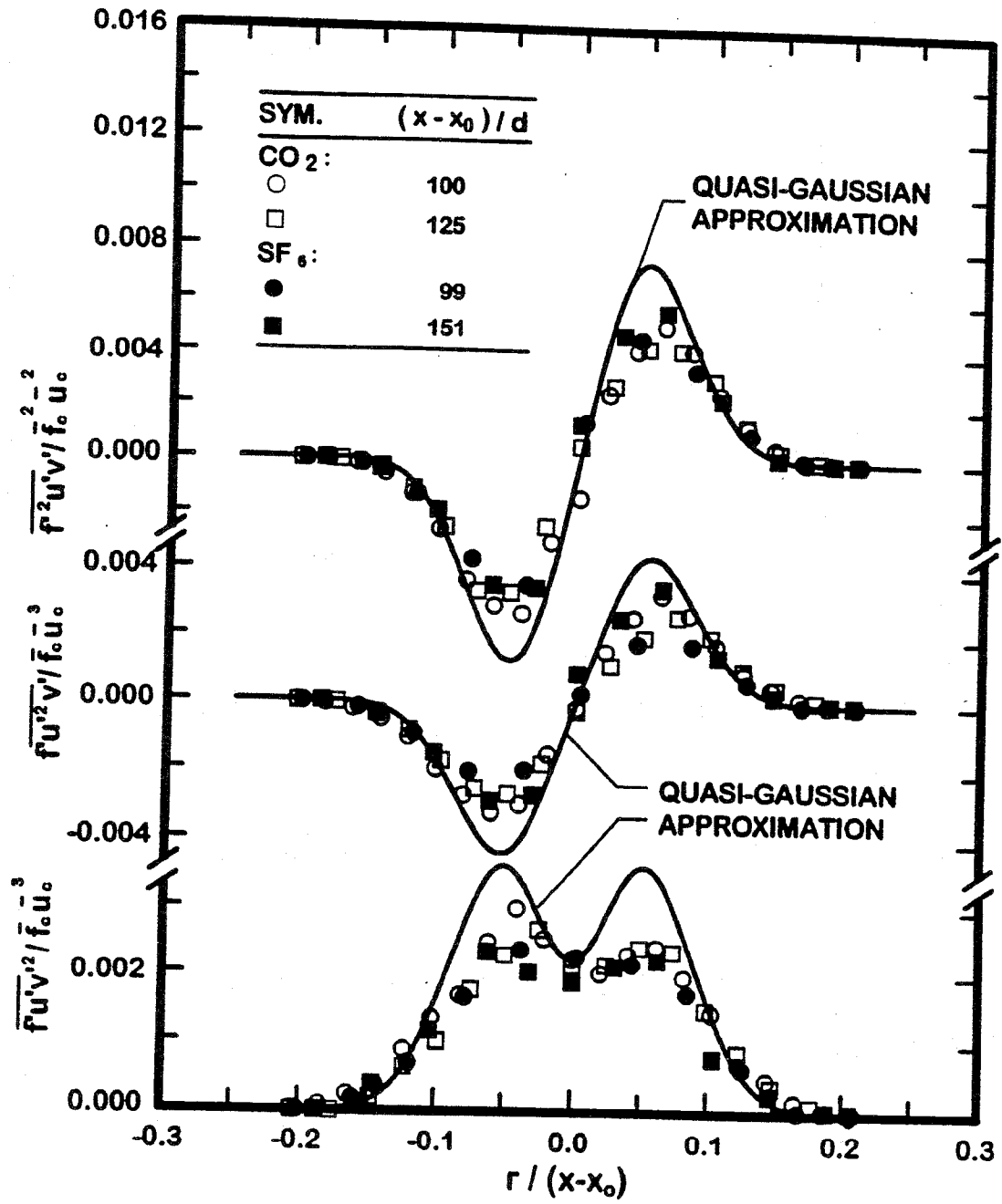


Fig. 20 Radial profiles of  $\overline{f'^2 u' v'}$ ,  $\overline{f' u'^2 v'}$  and  $\overline{f' u' v'^2}$  within self-preserving buoyant turbulent plumes.

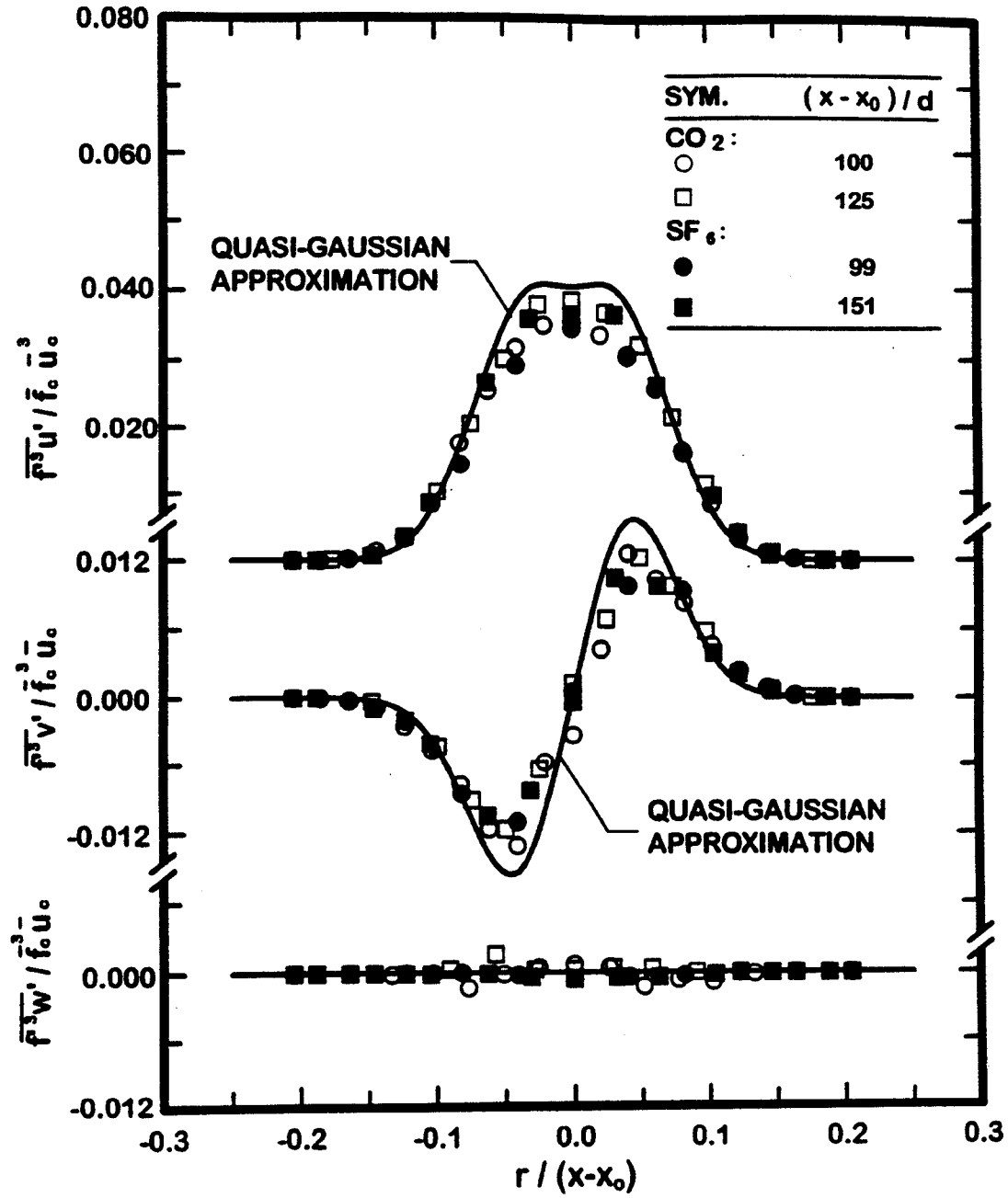


Fig. 21 Radial profiles of  $\overline{f'^3 u'}$ ,  $\overline{f'^3 v'}$  and  $\overline{f'^3 w'}$  within self-preserving buoyant turbulent plumes.

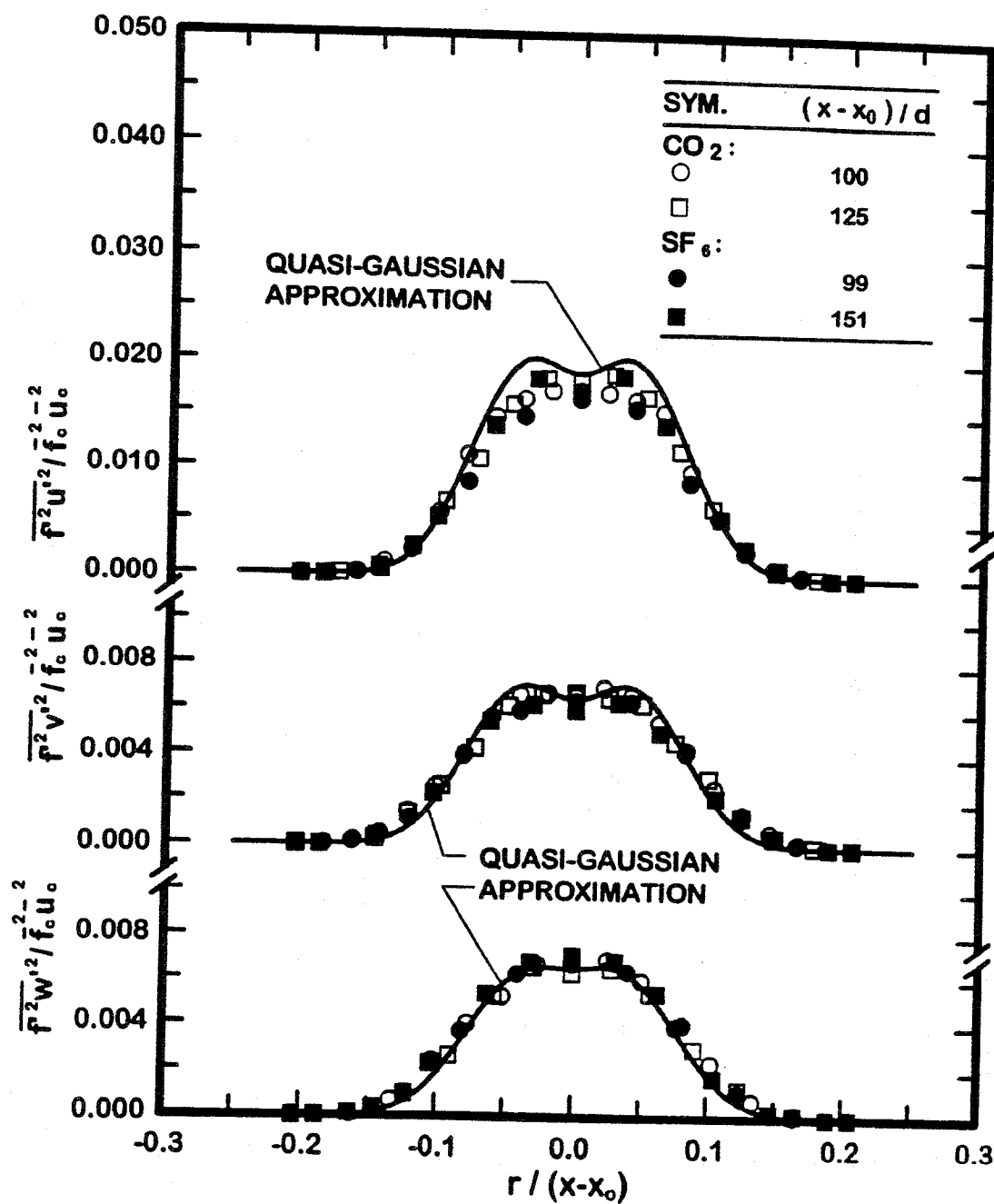


Fig. 22 Radial profiles of  $\overline{f'^2 u'^2}$ ,  $\overline{f'^2 v'^2}$  and  $\overline{f'^2 w'^2}$  within self-preserving buoyant turbulent plumes.

e.g.,  $\overline{f'w'^3}$ ,  $\overline{f'u'^2w'}$ ,  $\overline{f'^2u'v'}$  and  $\overline{f'^3w'}$ , all properly exhibit symmetry behavior. Finally, modeling fourth-order correlations, using the quasi-Gaussian approximation of equations (21) and (22) where  $f'$  can replace any component of velocity fluctuation, also is illustrated in Figs. 19-22. Similar to the fourth-order velocity fluctuation correlations, use of the quasi-Gaussian approximation is seen to be reasonably accurate for present results, in spite of anticipated effects of intermittency.

## 2.4 Conservation Checks and Budgets

In this section, measured moments in the self-preserving region of the round buoyant turbulent plumes will be used to provide conservation checks, e.g., direct evaluation of measurement accuracy using the governing equations of the flow. This exercise helps to show importance of various properties of the flow to overall flow behavior. Budgets of turbulence quantities are then considered in order to highlight the dominant mechanisms of turbulent mixing. The budgets of turbulence quantities also provide estimates of the rate of dissipation of turbulence kinetic energy and scalar dissipation which were not measured directly during the present experiments.

In order to complete conservation checks and find budgets, the various correlations in similarity variables were fitted with curves. This procedure involved using the general expressions of equations (11) and (12) for  $\bar{f}$  and  $\bar{u}$ , along with least-squares fits for the other parameters, see Figs. 7-17 for examples of these fits. Using the resulting fits, the governing equations for conservation of mass, momentum and mixture fraction have been integrated to find,  $\bar{v}$ ,  $\overline{u'v'}$  and  $\overline{f'v'}$  for comparison with direct measurements of these properties, as illustrated in Figs. 4,6 and 13. As discussed earlier, these predictions and direct measurements of  $\bar{v}$ ,  $\overline{u'v'}$  and  $\overline{f'v'}$  were in good agreement, which implies that the measurements were internally consistent and properly satisfy the governing equations within experimental uncertainties.

Checks of the governing equations for conservation of momentum and mixture fraction will now be reconsidered, by plotting the individual terms in the equations at each point in the flow; along with the error term needed to balance the governing equation. The appropriate governing equation for conservation of momentum appears as equation (19). Proceeding in order from left to right, the terms in this equation can be described as follows: streamwise advection, radial advection, streamwise transport, buoyancy force and radial transport. The plots of these terms for self-preserving flows, along with the resulting error term, are illustrated in Fig. 23. Following Panchapakesan and Lumley

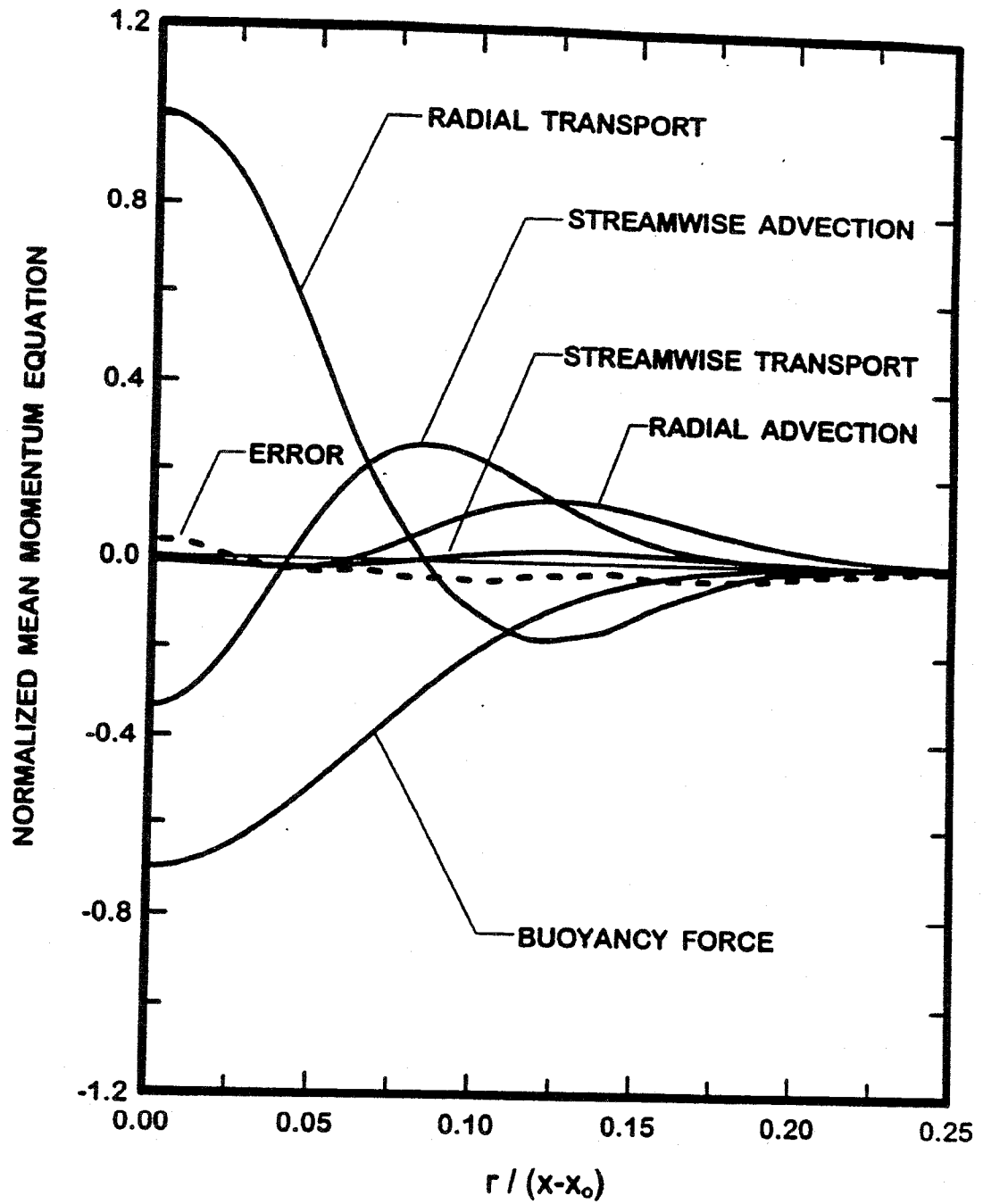


Fig. 23 Mean streamwise velocity budget within self-preserving buoyant turbulent plumes.

(1993), all the terms illustrated in Fig. 23 have been made dimensionless by multiplying them by  $(x-x_0)/\bar{u}_c^2$ . As anticipated from the evaluation of Reynolds stress illustrated in Fig. 6, the error term is relatively small across the width of the flow. In addition, the streamwise transport of momentum also is small, comparable to the error term; this behavior is reasonable because terms of this nature typically are small and are ignored under the boundary layer approximations. Near the axis, radial transport is the largest term and it is balanced mainly by the buoyancy force and streamwise advection. In contrast, near the edge of the flow radial advection and radial transport are the dominant terms and they balance each other.

The appropriate governing equation for conservation of mixture fraction (or the transport equation) is equation (23). Proceeding in order from left to right, the terms in this equation can be described as follows: streamwise advection, radial advection, streamwise transport and radial transport. The plots of these terms for self-preserving flows, along with the resulting error term, are illustrated in Fig. 24. Following Panchapakesan and Lumley (1993), all the terms illustrated in Fig. 24 have been made dimensionless by multiplying them by  $(x-x_0)/(\bar{f}_c \bar{u}_c)$ . As anticipated from evaluation of the radial turbulent mass flux illustrated in Fig. 13, the error term is relatively small across the width of the flow. The streamwise transport is somewhat larger for scalar variance than for conservation of momentum, due to the relatively large value of the  $\overline{f'u'}$  correlation near the axis of the flow; nevertheless, this term still is relatively small as expected for a boundary layer flow. Both near the flow axis and near the edge of the flow, radial transport is balanced by streamwise advection while radial advection remains relatively small throughout the flow.

The equation for turbulence kinetic energy for a round buoyant turbulent flow can be found in Panchapakesan and Lumley (1993), and Shabbir and Taulbee (1990). The terms in this equation are plotted for the self-preserving region in Fig. 25. Similar to the conservation checks, each term in the plots has been made dimensionless by multiplying it by  $(x-x_0)/\bar{u}_c^3$ . In this case, the production, advection and diffusion terms have been found directly from the measurements while the dissipation (or more exactly the sum of dissipation plus pressure diffusion) term has been found from the budget as a balance. The radial and total production terms, and the radial and total diffusion terms, are nearly the same as is expected for a boundary layer flow. Near the axis, buoyancy production, advection and radial diffusion are all roughly the same, and their sum is balanced by dissipation. The profiles of production, diffusion and dissipation are qualitatively similar to the results reported by Panchapakesan and Lumley (1993) for nonbuoyant turbulent jets; however, advection near the axis is much smaller for plumes than for jets (by a factor of 2-

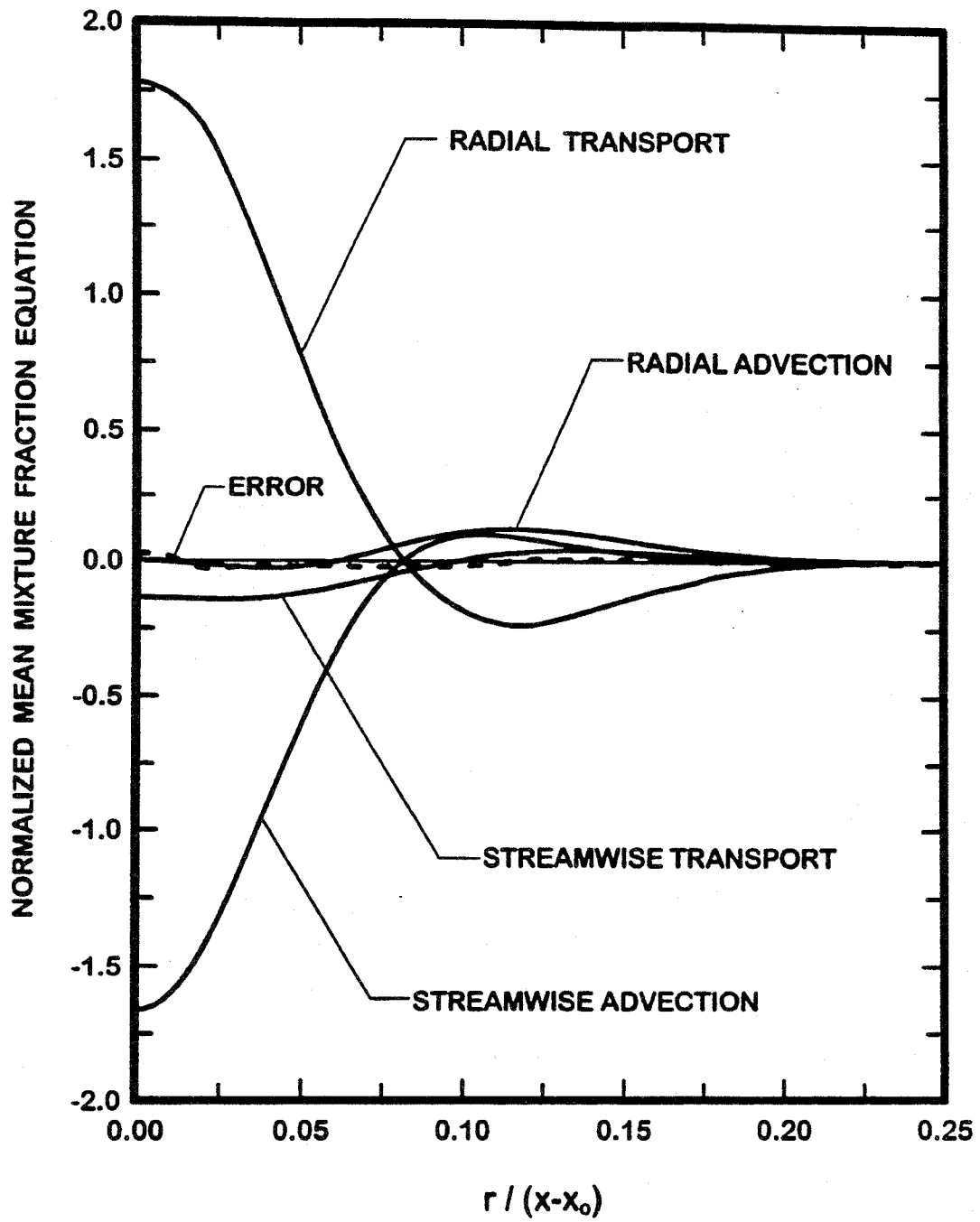


Fig. 24 Mean mixture fraction budget within self-preserving buoyant turbulent plumes.



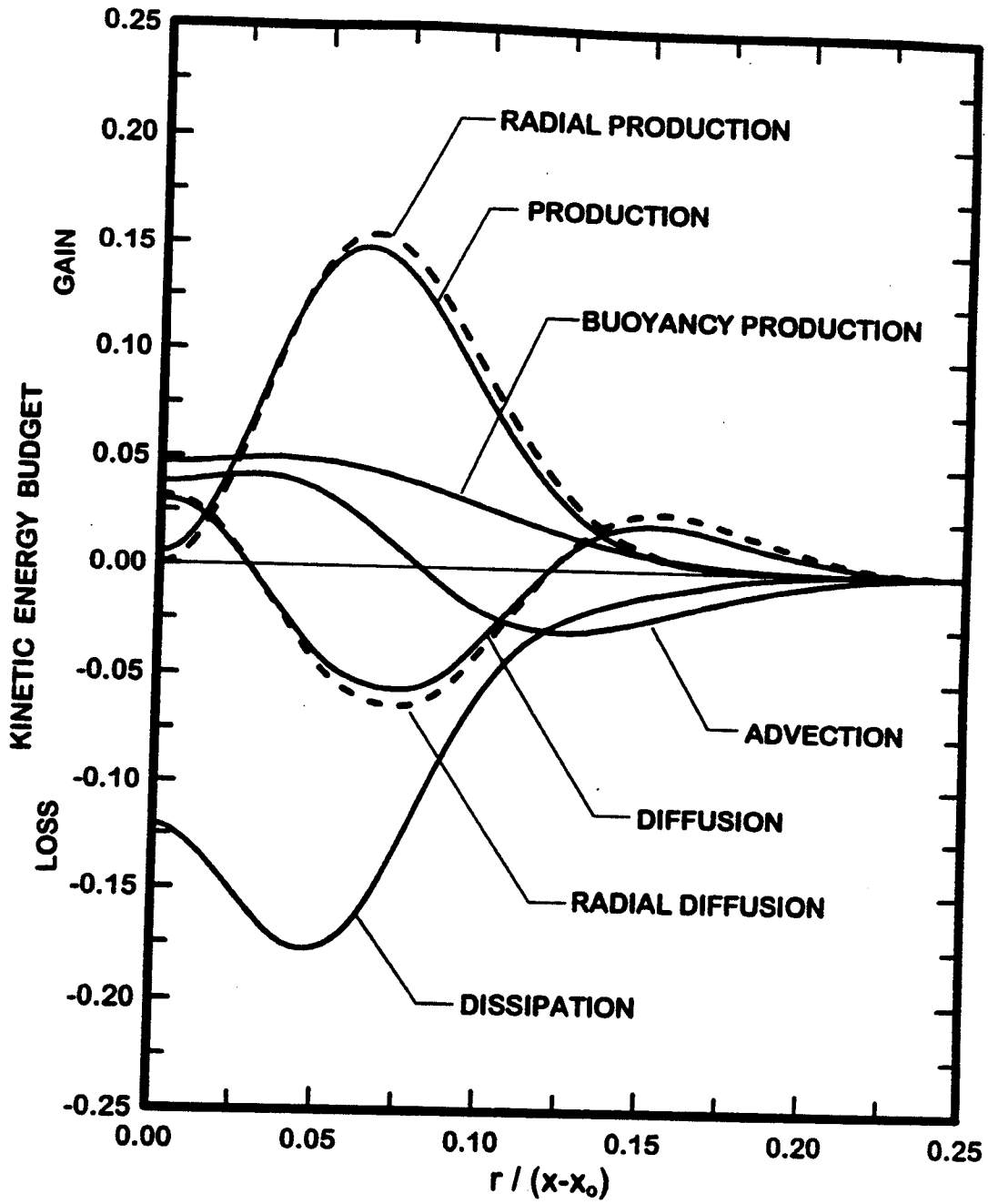


Fig. 25. Turbulence kinetic energy budget within self-preserving buoyant turbulent plumes.

3) which is compensated by contributions from buoyancy production and diffusion for the plumes.

The component energy budgets and the shear stress budget are illustrated in Figs. 26-29. The dissipation terms in these budgets have been estimated assuming small scale isotropy, i.e.,  $\epsilon_{ij} = (2\epsilon/3)\delta_{ij}$ , while the pressure diffusion term has been neglected when estimating  $\epsilon$  as before. The pressure terms in the component energy budgets, which contain both dispersive and non-dispersive effects, have been obtained as the balance. These latter approximations both follow Panchapakesan and Lumley (1993). The component energy budgets have properties analogous to nonbuoyant turbulent jets but are modified somewhat by effects of buoyancy. The energy production is almost entirely in  $\bar{u}'^2$  which is mainly shear production with an increasing contribution of buoyancy production near the flow axis. The energy produced in  $\bar{u}'^2$  is mainly transferred to  $\bar{v}'^2$  and  $\bar{w}'^2$  by the pressure redistribution term, i.e., the pressure term is mainly a loss in  $\bar{u}'^2$  and mainly a gain in  $\bar{v}'^2$  and  $\bar{w}'^2$ ; however, this redistribution is unequal, with  $\bar{w}'^2$  receiving more than  $\bar{v}'^2$ . Finally, the advection terms have the same shapes with the values near the axis proportional to the component energies in this region. The present shear stress budget generally is similar to results for nonbuoyant turbulent jets, with the contribution of buoyancy being rather small throughout.

The scalar variance budget is illustrated in Fig. 30. In this case, the various terms have been made dimensionless by multiplying the governing equation by  $(x-x_0)/(\bar{f}_c^2 \bar{u}_c)$ . Radial and total diffusion are nearly the same which is typical of a boundary-layer flow. In contrast, streamwise and radial production are only comparable near the edge of the flow, while streamwise production dominates near the axis as discussed earlier. It is likely that this increased production of scalar variance near the axis is responsible for the large values of scalar variance in this region. Near the axis, advection (with a smaller contribution from production) is balanced by dissipation. Near the edge of the flow, however, advection becomes small and radial production mainly balances diffusion. These trends are similar to the observations of Panchapakesan and Lumley (1993) for a transitional buoyant turbulent jet, except that the present flows have larger effects of advection, balanced by increased dissipation, near the axis.

The component turbulent mass flux budgets appear in Figs. 31 and 32. Similar to the other figures the terms in these figures have been normalized by multiplying the governing equation for the flux by  $(x-x_0)/(\bar{u}_c^2 \bar{f}_c)$ . The pressure terms for the streamwise and radial turbulent mass fluxes have been obtained as a balance since the other terms were known. Similar to the scalar variance budget, the radial and total production terms of  $\bar{f}'\bar{u}'$

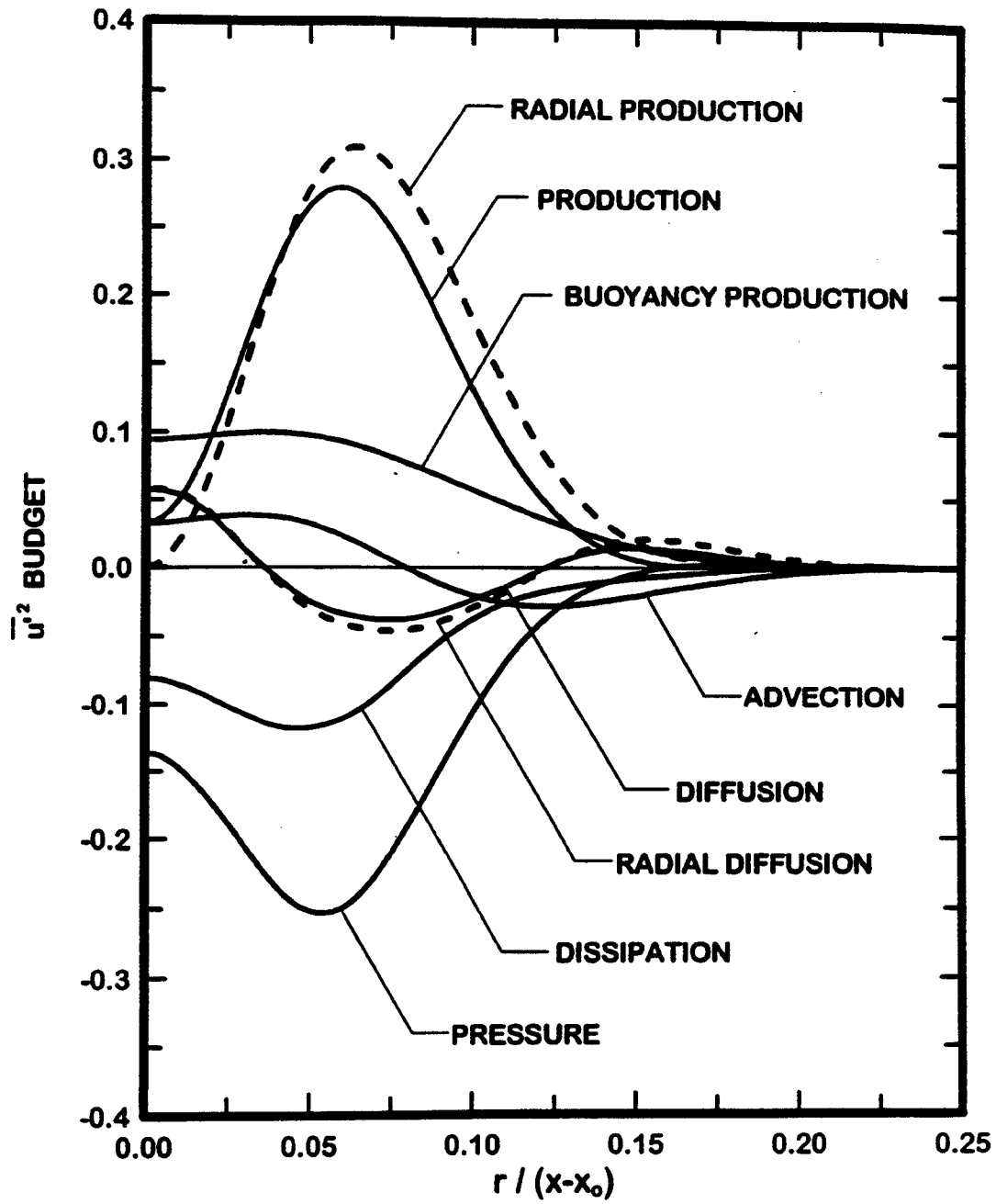


Fig. 26 Streamwise velocity fluctuation budget within self-preserving buoyant turbulent plumes.

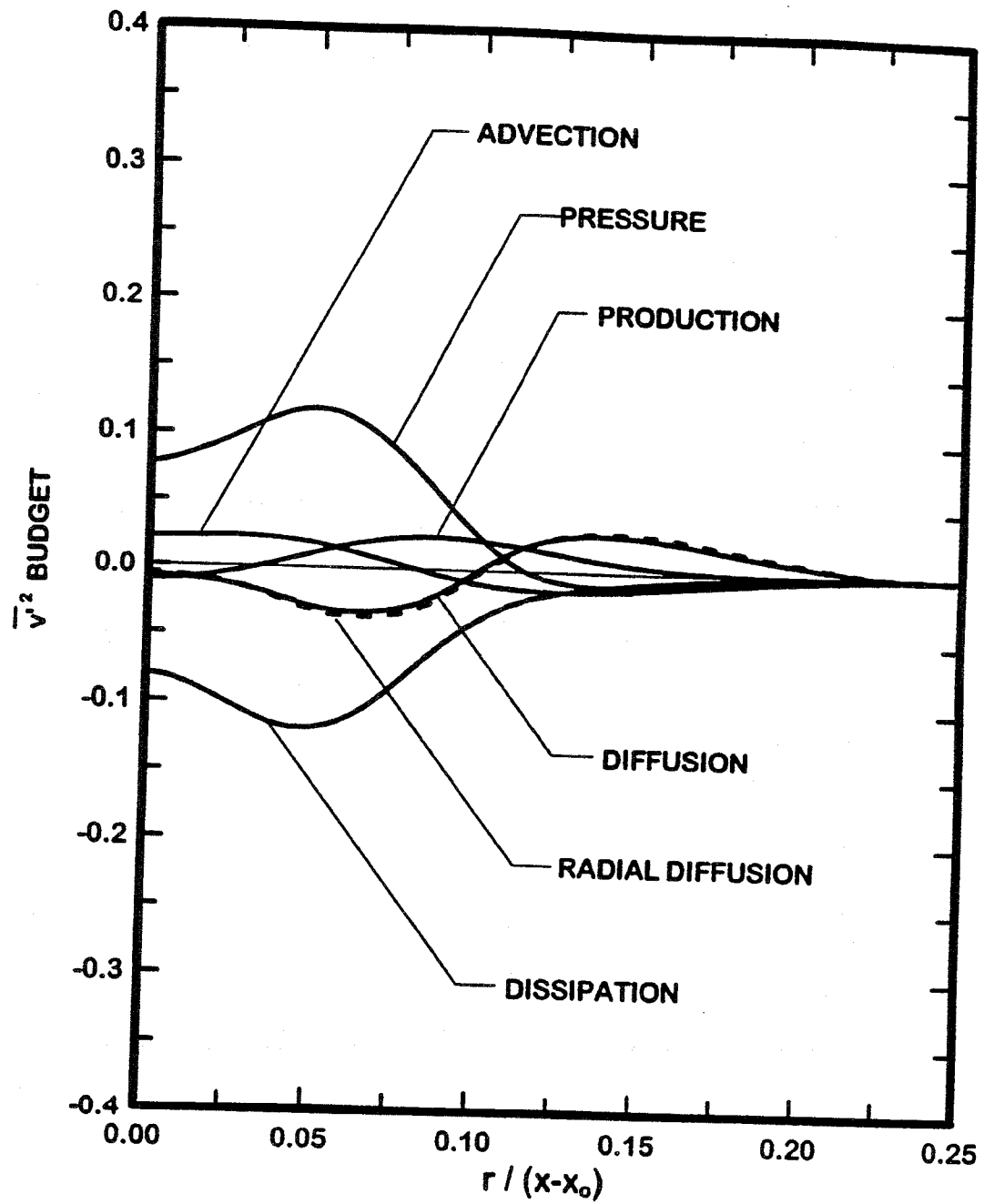


Fig. 27 Cross-stream velocity fluctuation budget within self-preserving buoyant turbulent plumes.

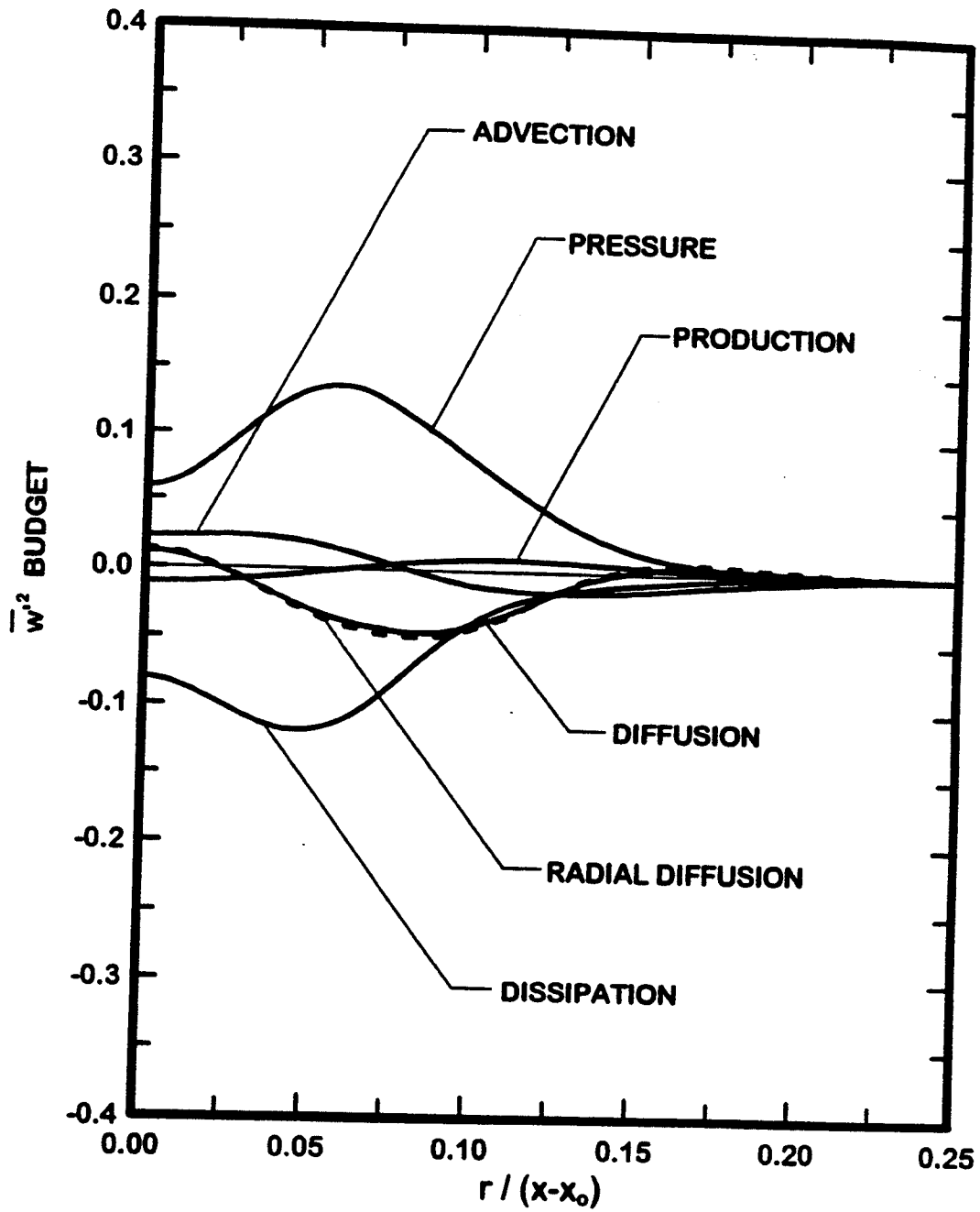


Fig. 28. Tangential velocity fluctuation budget within self-preserving buoyant turbulent plumes.

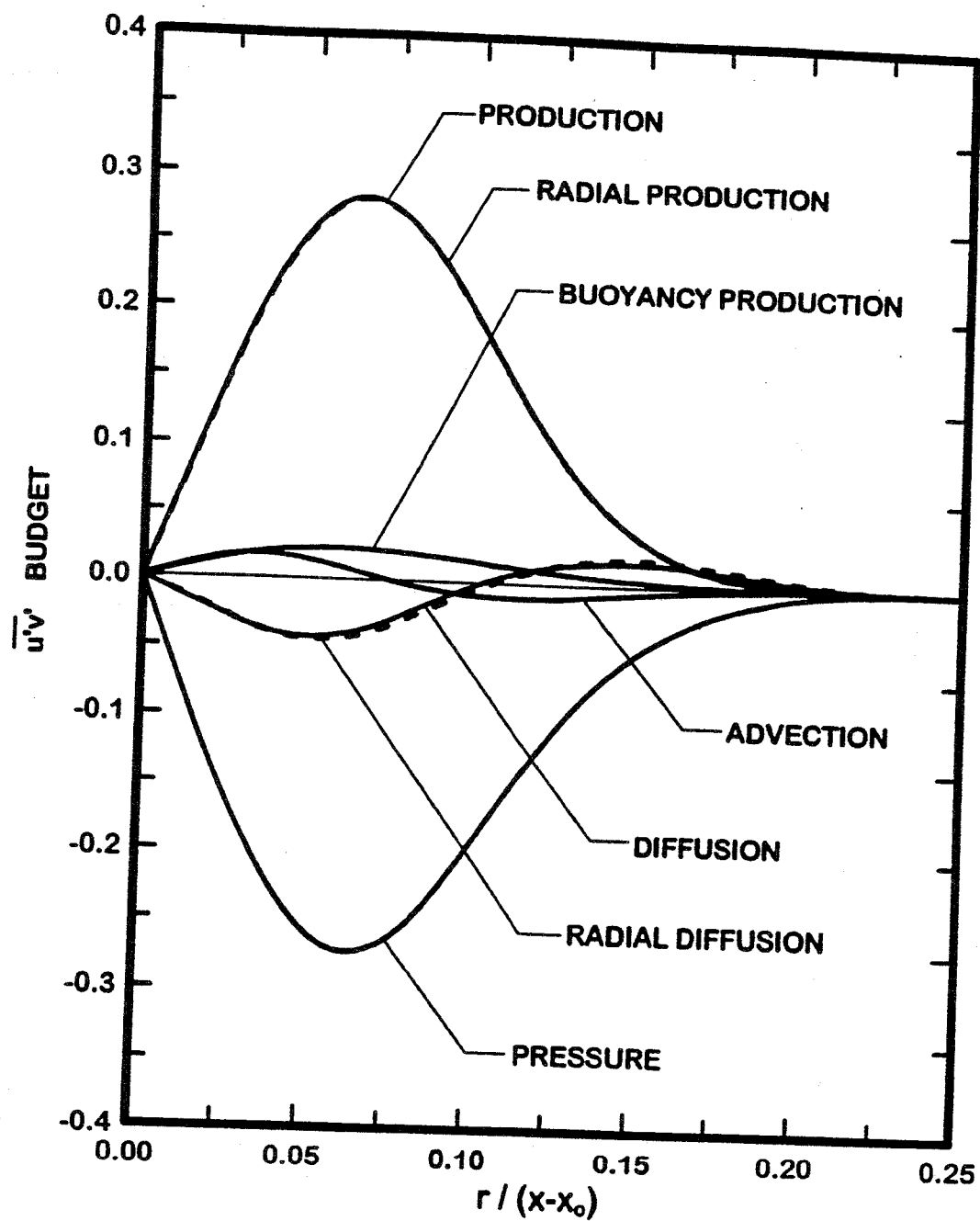


Fig. 29 Reynolds stress velocity fluctuation budget within self-preserving buoyant turbulent plumes.

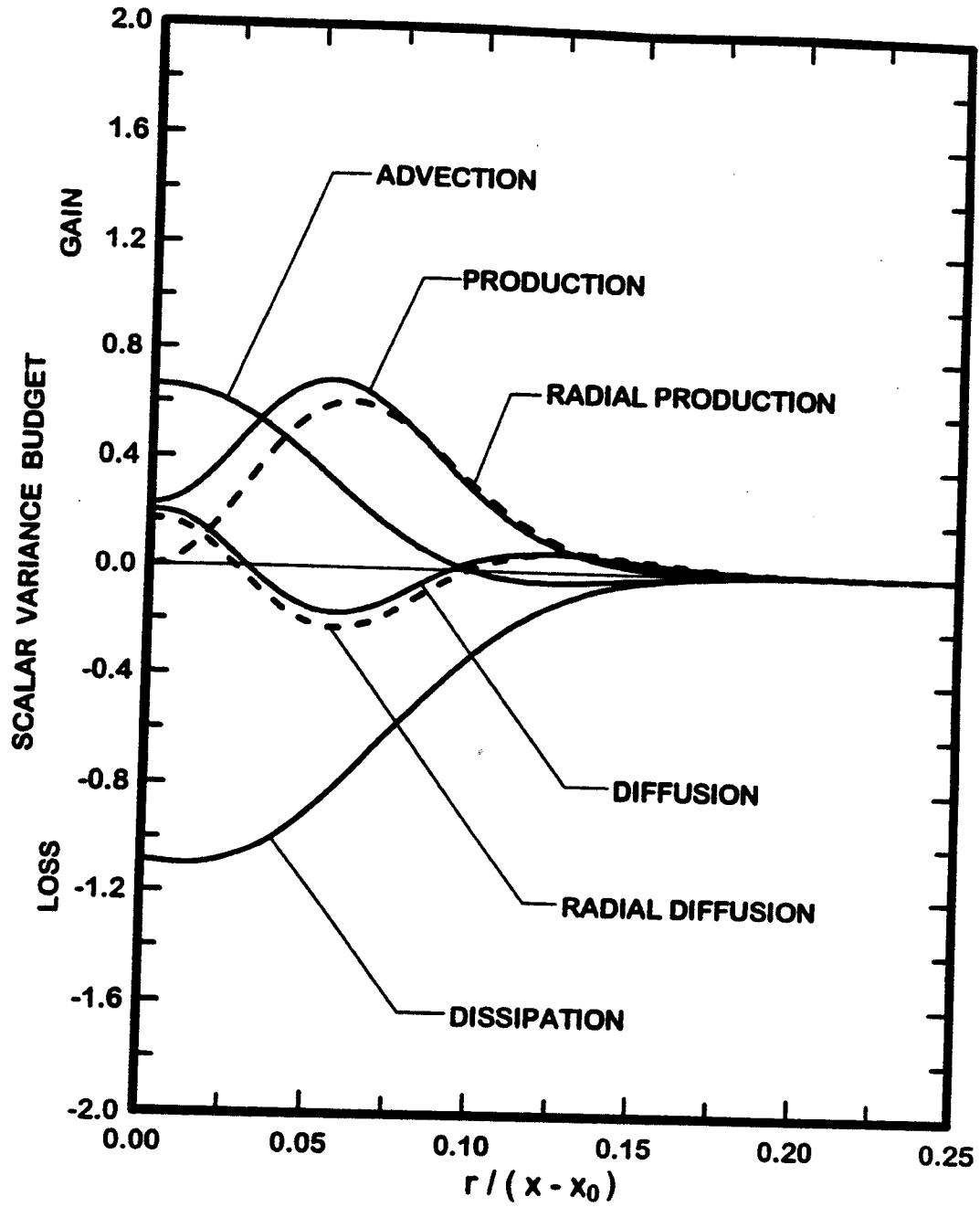


Fig. 30 Mixture fraction fluctuation budget within self-preserving buoyant turbulent plumes.

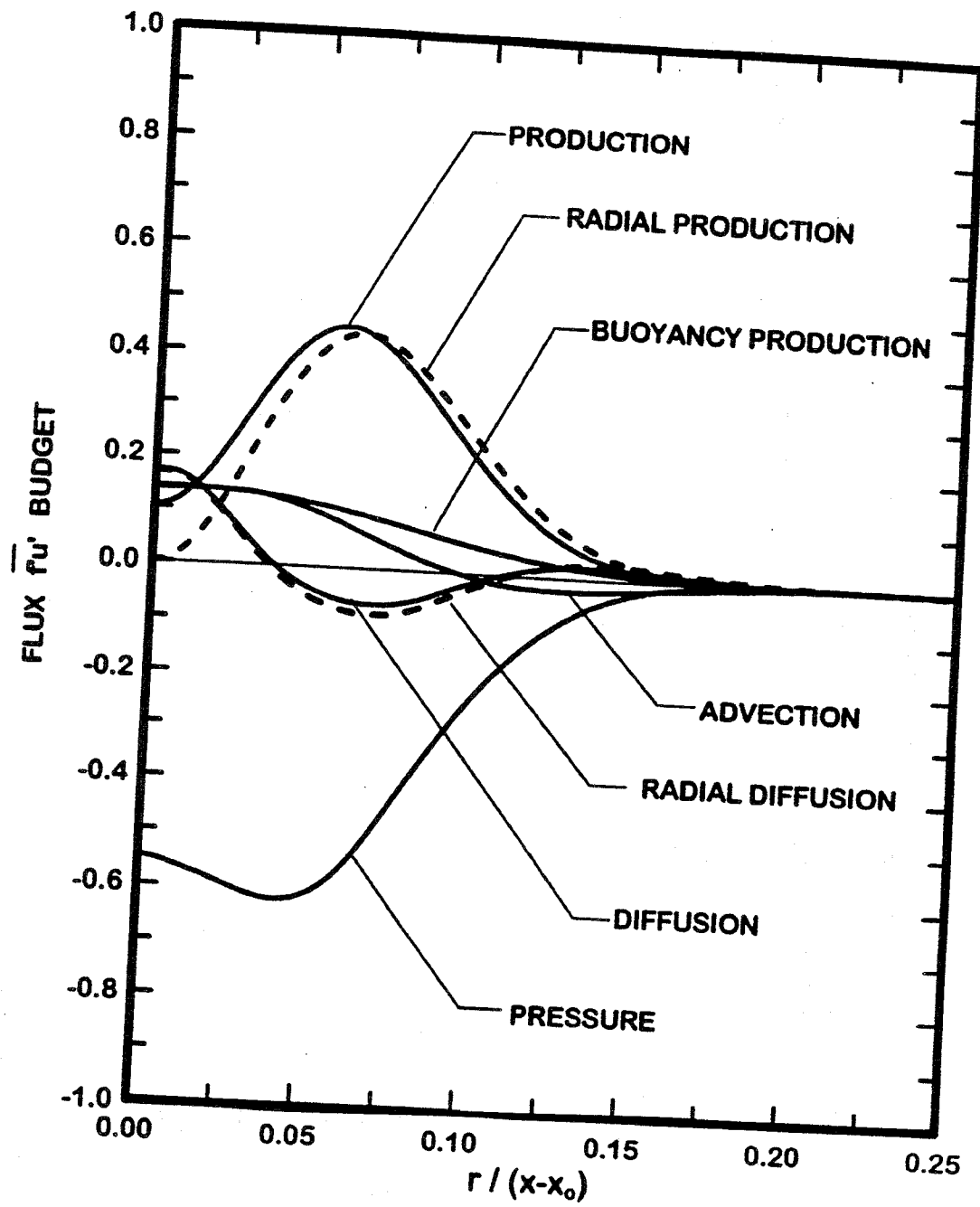


Fig. 31 Streamwise turbulent mixture fraction flux budget within self-preserving buoyant turbulent plumes.



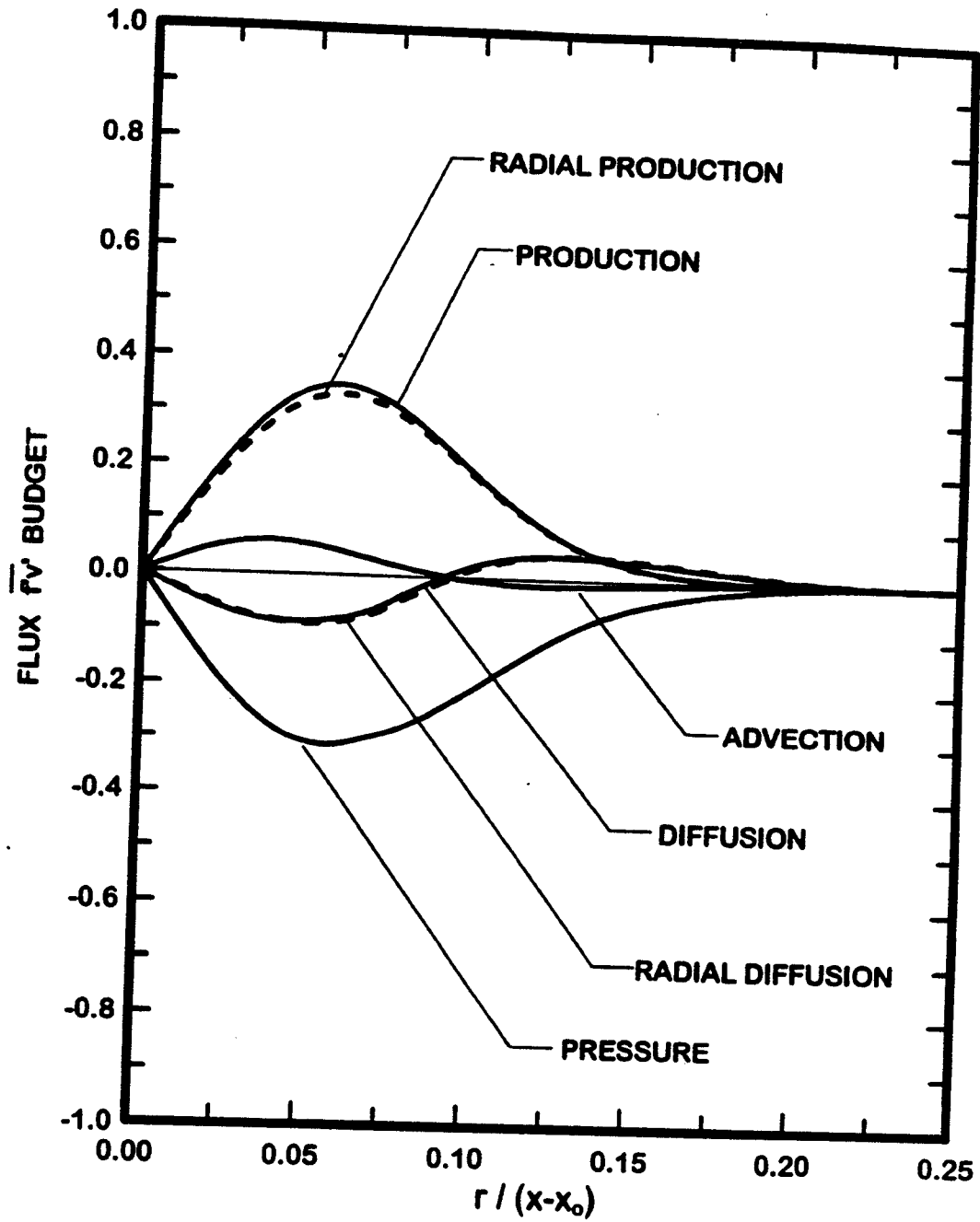


Fig. 32 Cross-stream turbulent mixture fraction flux budget within self-preserving buoyant turbulent plumes.

are similar near the edge of the flow but the streamwise production dominates production near the axis. In contrast to scalar variance which has no buoyancy production, however, the streamwise turbulent mass flux receives considerable buoyancy production near the axis. Thus, in this region, advection, buoyancy production, streamwise production and diffusion all combine to balance the loss through the pressure term. The radial turbulent mass flux budget illustrated in Fig. 32 mainly involves radial production balancing the pressure term, since diffusion and advection are relatively small. The full implications of all these results with respect to modeling buoyant turbulent flows is still under study; the first stages of model development based on the present measurements will be discussed next.

## 2.5 Modeling Implications

The differences between past and present estimates of self-preserving turbulent plume properties can have a considerable impact on the development and evaluation of models of turbulence. This can be illustrated by considering results recently reported by Pivovarov et al. (1992). This study involved testing a simplified contemporary turbulence model based on predictions assuming self-preserving flow, and comparing these predictions with the existing measurements of George et al. (1977), Shabbir (1987), Nakagome and Hirata (1977) and Ogino et al. (1980) — all of which involve transitional plumes based on present findings. Pivovarov et al. (1992) should be consulted for the specific features of the model that was considered, however, it involved  $k$ - $\epsilon$ - $g$  modeling procedures that have been widely used in field models of flame environments (Lockwood and Naguib, 1975). The main parameters that were adjusted to fit the measurements were the empirical constant  $C_\mu$  in the expression giving the effective turbulent kinematic viscosity as a function of  $k$  and  $\epsilon$  (Lockwood and Naguib, 1975):

$$\nu_T = C_\mu k^2 / \epsilon \quad (27)$$

and the effective turbulence Prandtl/Schmidt number,  $\sigma_T$ . All other constants in this model can be found in Lockwood and Naguib (1975).

Given the approach of Pivovarov et al. (1992), present work involved numerically integrating the governing equations under the assumption of self-preserving flow. Parameters considered in the calculations involved  $C_\mu = 0.09$  (the standard value) and 0.15 (a value considered by Pivovarov et al. (1992)) and  $\sigma_T = 0.7$  (the standard value) and 0.9 (a value considered by Pivovarov et al. (1992)). The resulting predictions, as well as those of Pivovarov et al. (1992), were compared with the measurements of George et al. (1977),

Shabbir (1987), Ogino et al. (1984), Nakagome et al. (1977) and the present study, as noted earlier.

The results of the predictions using the simplified  $k-\epsilon-g$  model and the measurements are illustrated in Figs. 33 and 34. These results are plotted in terms of the self-preserving variables with  $F(r/(x-x_0))$  and  $U(r/(x-x_0))$  illustrated in Figs. 33 and 34, respectively. The calculations include results obtained directly from Pivovarov et al. (1992) as well as present results using the same empirical constants in the turbulence model; in general, the two sets of results are the same within plotting and computational accuracy.

The predictions illustrated in Figs. 33 and 34 are not very sensitive to changes of  $\sigma_T$  between 0.7 and 0.9. However, increasing the value of  $C_\mu$  causes the profiles to become broader because this directly increases the effective turbulent viscosity for given turbulence conditions. Thus, Pivovarov et al. (1992) recommend the higher value of  $C_\mu$ , rather than the widely accepted value of 0.09, because it provided the best agreement between their predictions and the measurements of George et al. (1977), Nakagome and Hirata (1977), Ogino et al. (1980) and Shabbir (1987) for both mixture fractions and streamwise velocities. However, present results have shown that all these measurements represent transitional plumes; therefore, the unusually large value of  $C_\mu$  simply is compensating for effects of flow development that are ignored by the theory. In contrast, predictions based on  $C_\mu = 0.09$ , the normal value, are in best agreement with the present measurements which properly represent self-preserving plume behavior. More detailed evaluation of the simplified  $k-\epsilon-g$  model currently is in progress. However, even results thus far have highlighted deficiencies for this approach when more complex buoyant turbulent flows are considered; for example,  $\sigma_T = 0.7$  is not very realistic (see Fig. 14), effects of countergradient diffusion are encountered,  $v_t$  is not properly isotropic for streamwise and cross-stream transport, etc. Thus, more sophisticated higher-order turbulence closures will be required to treat flows representative of practical fire environments. It is hoped that present results for round self-preserving buoyant turbulent plumes will be useful for developing and evaluating such advanced turbulence modeling procedures.

## 2.6 Conclusions

Mixture fraction, velocity and combined mixture-fraction/velocity statistics were measured in round buoyant turbulent plumes in stratified still air. The test conditions involved buoyant jet sources of carbon dioxide and sulfur hexafluoride with  $(x-x_0)/d$  in the

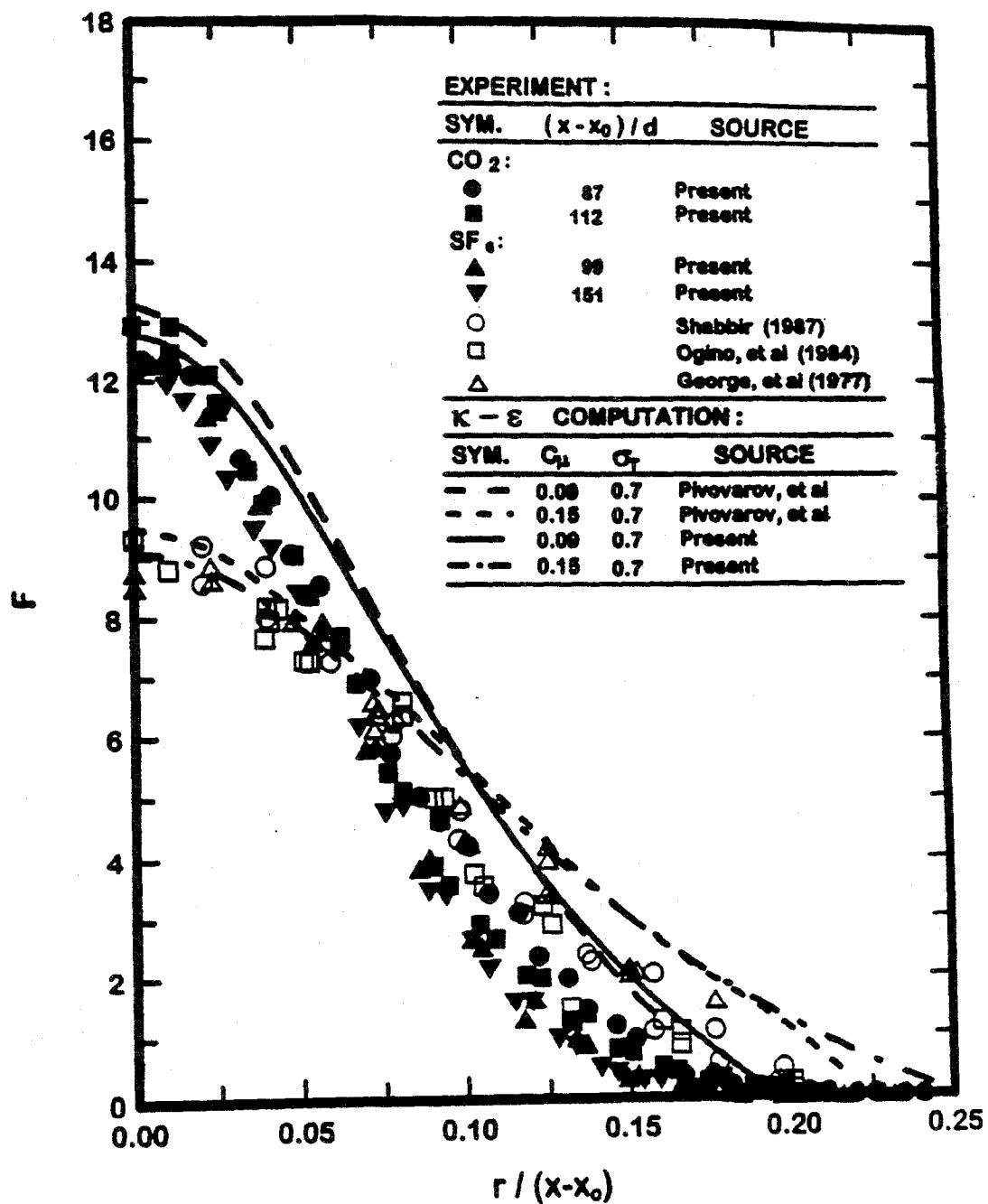


Fig. 33 Radial profiles of predicted and measured mean mixture fractions within self-preserving buoyant turbulent plumes.

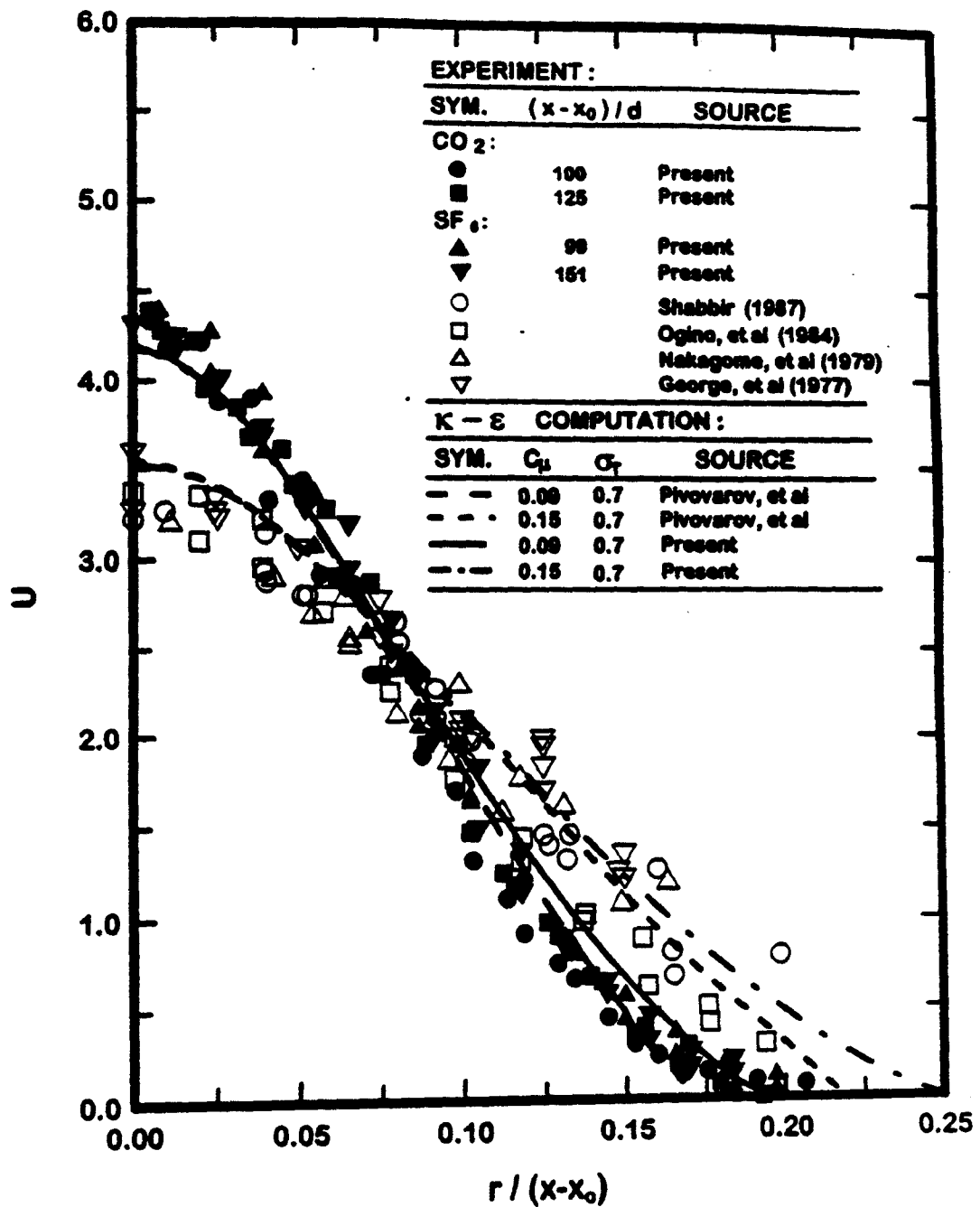


Fig. 34 Radial profiles of predicted and measured mean streamwise velocities within self-preserving buoyant turbulent plumes.

range 0-151 and  $(x-x_0)/\ell_m$  in the range 0-43. The major conclusions of the study are as follows:

1. Present measurements yielded self-preserving behavior of both mean and fluctuating flow properties for  $(x-x_0)/d$  in the range 87-151 and  $(x-x_0)/\ell_m$  in the range 12-43. These results yielded flows that were up to 40% narrower, with scaled values near the axis up to 30% larger, than earlier results in the literature that were thought to represent self-preserving buoyant turbulent plume behavior.
2. Evaluation of present measurements in the self-preserving region of the flow supported the internal consistency of the measurements. These evaluations involved predictions of  $\bar{v}$ ,  $\overline{u'v'}$ , and  $\overline{f'v'}$  based on the governing equations of conservation of mass, momentum and mixture fraction, and present measurements, that were in good agreement with direct measurements of these properties. In addition, direct evaluation of the governing equations of mean quantities, based on present measurements, yielded small error or residual values, in the range anticipated based on estimates of the experimental uncertainties of the measurements.
3. Measured values of various fourth moments of velocity and mixture fraction fluctuations generally satisfied the quasi-Gaussian approximation, which should be helpful for closing higher order models of buoyant turbulent flows. Surprisingly, quasi-Gaussian behavior was even observed near the edge of the plumes where effects of intermittency should be significant.
4. Assessment of earlier simplified  $k-\epsilon$ - $g$  turbulence models for round buoyant turbulent plume properties at self-preserving conditions, based on present measurements, was quite successful in contrast to earlier evaluations that were compromised by measurements only appropriate for transitional plumes. This level of success for a simplified turbulence model, however, is not surprising for a simple boundary layer flow like the buoyant turbulent plume. Thus, more detailed examination of predictions exhibited model deficiencies that will be problematical for the more practical flows encountered in fire environments, e.g., large variations of  $\sigma_T$ , countergradient diffusion, strong production of scalar variance due to streamwise buoyant instability near the axis. It is concluded that models involving higher-order turbulence closures will be needed for reliable treatment of practical buoyant turbulent flows.

Current work is emphasizing the evaluation of various higher-order turbulence closures using present data for round self-preserving buoyant turbulent plumes in order to avoid the uncertainties of flow development effects from particular plume sources.

### 3. Soot Optical Properties

#### 3.1 Introduction

Practical hydrocarbon fueled flames generally contain and emit soot, which affects their radiation, structure and pollutant emission properties. These effects have motivated considerable interest in the structure and optical properties of soot, in order to develop nonintrusive methods for measuring soot properties and to estimate the continuum radiation and heterogeneous reaction properties of soot in flame environments. This phase of the present investigation seeks to contribute to a better understanding of soot structure, by undertaking a computational and experimental study of the structure of soot aggregates, emphasizing characteristics needed to define soot optical and fractal properties, and to understand the relationships between actual and projected soot images.

Earlier work concerning the structure and optical properties of soot has been reviewed by Tien and Lee (1982), Viskanta and Mengüç (1987), Jullien and Botet (1987) and Köylü and Faeth (1993a); therefore, consideration of past studies will be brief. Initial studies of the structure of soot by Erickson et al. (1964), Dalzell et al. (1970) and Wersborg et al. (1972) involved thermophoretic and molecular beam sampling of premixed acetylene, benzene and propane flames, followed by analysis using transmission electron microscopy (TEM). The results showed that soot consisted of small spherical primary particles, having nearly constant diameters, collected into open structured aggregates that had broad distributions of the number of primary particles per aggregate. Subsequent work using thermophoretic sampling and TEM established similar behavior for a variety of fuels and flame conditions, e.g., laminar and turbulent flames as well as premixed and diffusion flames (Medalia and Heckman, 1969; Magnussen, 1974; Tence et al., 1986; Martin and Hurd, 1987; Samson et al., 1987, Mountain and Mulholland, 1988; Dobbins and Megaridis, 1987, 1991; Megaridis and Dobbins, 1989, 1990; Puri et al., 1993; Köylü and Faeth, 1993a,b, 1994a,b). In general, the distributions of primary particle diameters had standard deviations of 15-25% of the mean primary particle diameter, supporting the observations of nearly uniform primary particle sizes (Köylü and Faeth, 1993a). Additionally, primary particle diameters generally were less than 60 nm, with the largest diameters associated with heavily sooting fuels (Köylü and Faeth, 1993a). This behavior

yields primary particle size diameters,  $x_p < 0.4$ , for wavelengths of interest for optical measurements of soot properties and estimates of continuum radiation from soot ( $\lambda > 500$  nm). As a result, it is reasonable to assume that individual primary particles approximate Rayleigh scattering particles, e.g., their total scattering and absorption cross-sections typically are within 1 and 5%, respectively, of estimates based on Mie scattering theory for  $\lambda > 500$  nm (Köylü and Faeth, 1993a).

Soot aggregates are small near the soot inception point in flames but they aggregate rapidly with the mean number of primary particles per aggregate reaching values in the range 200-600 for soot emitted from large buoyant turbulent diffusion flames (Köylü and Faeth, 1993a). As noted earlier, unlike primary particle diameters, aggregate size distributions are broad; in fact, the standard deviations of aggregate size are comparable to the mean value of the number of primary particles in an aggregate. Thus, aggregate size distributions generally are represented by the log normal size distribution function while 95% of the soot aggregates emitted from large turbulent diffusion flames contain 30-1800 primary particles (Köylü and Faeth, 1992, 1993a). This complexity of aggregate size distributions, however, is mitigated by the observation that soot aggregates exhibit mass fractal-like behavior with a Hausdorf or mass fractal dimension,  $D_f < 2$ , even when the number of primary particles in an aggregate is small (Jullien and Botet, 1987). The mass fractal approximation implies the following relationship between the primary particle diameter, the number of primary particles in an aggregate and the radius of gyration of an aggregate (Jullien and Botet, 1987):

$$N = k_f (R_g/d_p)^{D_f} \quad (28)$$

where  $k_f$  is a constant fractal prefactor and the aggregates are assumed to consist of monodisperse non-overlapping spherical primary particles, i.e., the mean value of  $d_p$  is used in equation (28). This fractal-like behavior has important implications for the optical properties of soot which will be discussed next.

Measurements show that flame-generated soot ranges from small aggregates (dimensions on the order of 10 nm) near the start of soot formation, to large aggregates (dimensions on the order of 1  $\mu$ m) emitted from large buoyant turbulent diffusion flames (Köylü and Faeth, 1992, 1993a,b). The larger sized aggregates are too large for reasonable application of the Rayleigh scattering approximation and are too open structured for proper representation as equivalent compact spheres using the Mie scattering approximation (Köylü and Faeth, 1993a). These difficulties were established by direct measurements of soot scattering properties during early work (Erickson et al., 1964;



Erickson et al., 1964; Wersborg et al., 1972). For example, strong forward scattering was observed which is not representative of Rayleigh scattering behavior, while use of the Mie scattering approximation for an equivalent sphere still did not provide an adequate fit of scattering measurements. The former behavior follows because the large soot aggregates in the size distribution dominate scattering properties and are too large to be approximated as Rayleigh scattering objects. Additionally, the fact that soot aggregates have fractal dimensions less than 2 implies that their structure is too open to be represented by a compact object such as an equivalent Mie scattering sphere (Berry and Percival, 1986). The limitations of the Rayleigh and Mie scattering theories prompted subsequent development of optical theories of soot aggregates based on the Rayleigh-Debye-Gans (RDG) scattering approximation for mass fractal objects involving monodisperse spherical primary particles that just touch one another (Jullien and Botet, 1987; Köylü and Faeth, 1993a; Martin and Hurd, 1987; Dobbins and Megaridis, 1991). The large refractive indices of soot raised questions about the validity of the RDG scattering approximation (Köylü and Faeth, 1993a), however, recent work where both soot structure and scattering properties were known, has demonstrated performance of the RDG scattering theory for polydisperse fractal soot aggregates within experimental and computational uncertainties (Köylü and Faeth, 1994a,b; Farias et al., 1994a,b)

The reasonably successful evaluation of the RDG scattering theory for soot aggregates provides potential for resolving long-standing problems of the accurate determination of the refractive indices of soot, as well as for developing methods of solving the inverse problem so that soot structure properties can be found nonintrusively from scattering measurements (Köylü and Faeth, 1993a, 1994a,b; Sorensen et al., 1992; Cai et al., 1993). Both these objectives, however, are inhibited by current limitations about the fractal and polydisperse properties of practical soot aggregates in flames. In particular, RDG theory requires values of  $R_g$  as a function of  $N$  but this determination is inhibited by current uncertainties concerning  $D_f$  and more particularly  $k_f$  (Köylü and Faeth, 1993a,b). Additionally, information about  $k_f$  requires analysis of actual three-dimensional soot aggregates, which can be facilitated by the availability of relationships between the projected and the actual properties of soot aggregates. Unfortunately, currently available information along these lines is rather limited. In particular, evaluation of relationships between projected and true three-dimensional properties of soot aggregates have only involved small aggregate samples and a few flame conditions (Martin and Hurd, 1987; Samson et al., 1987; Köylü and Faeth, 1992). Recent work by Sorensen et al. (1993) and Cai et al. (1993) has sought to extend understanding of the projected and fractal properties of soot aggregates but more development of their experimental methods will be needed for definitive results. Finally, Wu and Friedlander (1993) address the fractal properties of

aggregates based on existing results for numerically simulated populations of aggregates of spherical primary particles; however, the relevance of these findings to practical soot aggregates must still be established.

In view of current limitations about the structure and optical properties of soot aggregates, the objective of the present investigation was to study soot structure in order to define soot optical and fractal properties, as well as the relationships between actual and projected soot images. This work involved direct evaluation of the relationships between the number of primary particles and the projected image of an aggregate, the relationships between the radius of gyration of an aggregate and properties of its projected image, and the values of the Hausdorff or mass fractal dimensions and prefactors of soot in flame environments. The new information was developed by considering both numerically simulated and experimentally measured soot aggregates. The numerical simulations to create soot aggregates were based on cluster-cluster aggregation along the lines of Jullien and Botet (1987), Mountain and Mulholland (1988) and Farias et al. (1994a). The experimental soot aggregates were obtained from two sources, as follows: the large soot aggregates found in the fuel-lean region of buoyant turbulent diffusion flames in the long residence time regime, where soot generation factors and soot structure are independent of flame position and residence time (Köylü and Faeth, 1991, 1992, 1994a; Sivathanu and Faeth, 1991); and soot aggregates collected in both the fuel-rich and fuel-lean regions of laminar jet diffusion flames (Sunderland et al., 1994). Taken together, the experimental soot properties involve a variety of fuels — acetylene, propylene, ethylene and propane — burning in air within diffusion flames.

The discussion begins with consideration of numerically simulated soot aggregates in order to establish relationships between actual and projected soot aggregate properties. Measured soot aggregate properties are then considered, emphasizing soot fractal properties.

### 3.2 Numerically Simulated Aggregates

Aggregate Simulation. Mountain and Mulholland (1988) generated soot aggregates using a simulation involving cluster-cluster aggregation based on a solution of the Langevin equations. This approach yields fractal-like aggregates that satisfy the power-law relationship of equation (28) with  $1.7 < D_f < 1.9$  and  $k_f$  ca. 5.5 for  $N > 10$ . However, a larger sample of aggregates was required for present work, and it was desired to have  $1.7 < D_f < 1.8$  and  $k_f$  of roughly 8.0 in order to correspond to recent experimental observations

of the fractal properties of soot aggregates (Köylü and Faeth, 1992, 1994a,b). As a result, an alternative aggregate simulation, based on the approach used by Farias et al. (1994a), was used during the present investigation.

The present aggregate simulation involved creating a population of aggregates by cluster-cluster aggregation, following Jullien and Botet (1987). The simulation began with individual and pairs of primary particles which were attached to each other randomly, assuming uniform distributions of the point and orientation of attachment, while rejecting configurations where primary particles intersected. This procedure was continued in order to form progressively larger aggregates, but with the additional restriction that the aggregates should have  $1.7 < D_f < 1.8$  with  $k_f$  of 8 for  $N > 8$ , based on equation (28) applied to the computed value of  $R_g$  for the aggregate. It was observed that  $D_f$  fell naturally in the range 1.6-1.9 for  $N > 48$  during these simulations; therefore, few cluster-cluster combinations were rejected for inappropriate fractal properties when larger aggregates were constructed. Similarly, for  $D_f$  in the range 1.7-1.8, the value of  $k_f$  fell naturally near  $k_f = 8.0$  for statistically significant populations of aggregates. Naturally, the numerically simulated aggregates were not useful for investigating aggregate fractal properties because their fractal properties had been prescribed. Nevertheless, these objects were useful for investigating relationships between projected and actual aggregate properties because the simulated aggregates were very similar to actual aggregates while their known geometry vastly simplified determinations of actual and projected aggregate properties.

The population of simulated aggregates involved  $N$  in the range 20-1000, considering 20 aggregate sizes. Results for each aggregate size were averaged over 20 different aggregates to yield a total sample of 400 aggregates. In order to fix ideas, a primary particle diameter of 50 nm was used for the simulations, which is typical of soot aggregates for heavily sooting materials (Köylü and Faeth, 1992). Present results are normalized by  $d_p$  or  $A_p$ , however, and such normalized results are independent of  $d_p$ , at least for  $d_p$  less than 60 nm (Köylü and Faeth, 1994a,b).

Projected images of typical aggregates constructed using the present simulation are illustrated elsewhere for  $N=16$ , 64 and 256 (Farias et al., 1994a). An example involving projected images of a given aggregate in three orthogonal directions for  $N=100$ , is illustrated in Fig. 35. This particular aggregate had  $D_f = 1.76$  while  $d_p = 50$  nm as noted earlier. Even though the value of  $N$  used in Fig. 35 is relatively modest, the dimensions of the aggregate are substantial, reaching maximum projected lengths greater than 1  $\mu\text{m}$ . It is evident that the appearance of an aggregate varies considerably with the direction of the

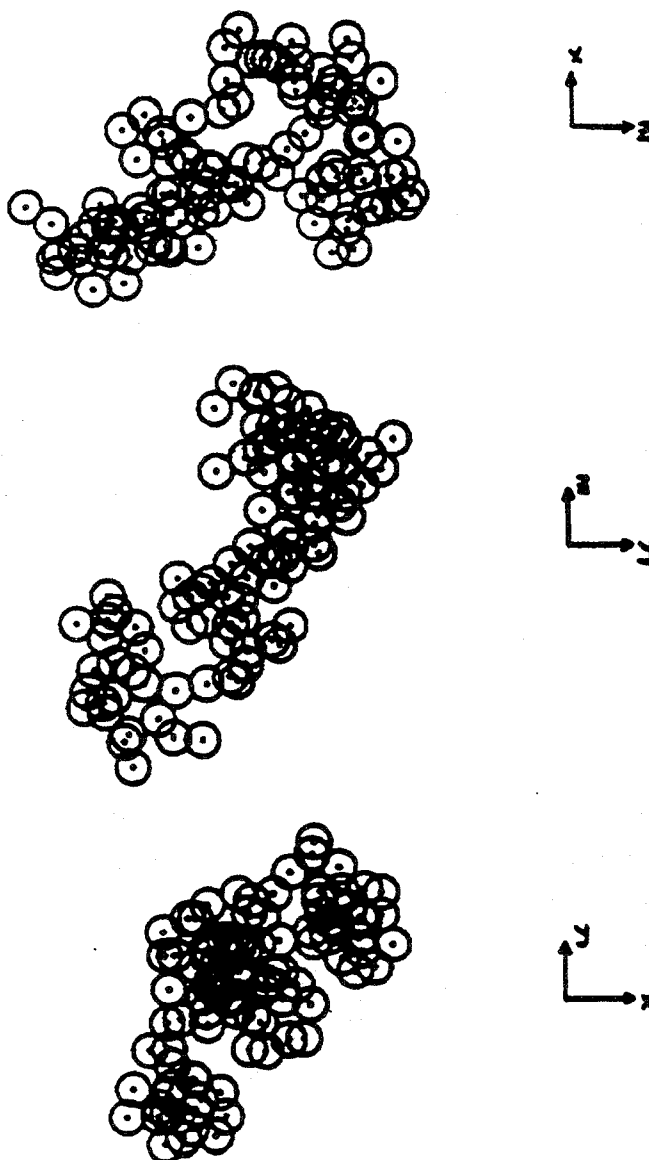
$N=100$ 

Fig. 35 Projected images of a numerically simulated soot aggregate.

projection; it also varies substantially from aggregate to aggregate within a population of given size (Farias et al., 1994a). Nevertheless, the present simulated aggregates are qualitatively similar to both past experimental observations of soot aggregates and other numerical simulations of soot aggregates (Jullien and Botet, 1987; Mountain and Mulholland, 1988). Combined with their prescribed fractal properties, this behavior suggests that the present simulated aggregate populations are reasonably representative of the structure of soot aggregates found in flame environments.

Results and Discussion. The first property studied using the numerically simulated aggregates was the relationship between the number of primary particles in an aggregate and the projected area of the aggregate. Several workers have suggested the following relationship between the projected area of a soot aggregate,  $A_a$ , and  $N$  (Samson et al., 1987; Megaridis and Dobbins, 1989, 1990; Puri et al., 1993; Köylü and Faeth, 1992):

$$N = k_a(A_a/A_p)^\alpha \quad (29)$$

where  $\alpha$  is an empirical projected area exponent and  $k_a$  is a constant normally taken to be unity. Results for the present simulated aggregates, based on random projections of the aggregates, are plotted according to equation (29) in Fig. 36. The power-law correlation of equation (29) is seen to provide an excellent fit of the data. The least-squares fit values of the correlation of equation (29) are  $\alpha = 1.10$  and  $k_a = 1.16$  with standard deviations of 0.002 and 0.01, respectively. The value of  $\alpha$  is in reasonable agreement with earlier assessments although the present value of  $k_a$  exceeds the value of unity used in earlier work (Samson et al., 1987; Megaridis and Dobbins, 1989, 1990; Puri et al., 1993; Köylü and Faeth, 1992). Further consideration of these differences will be undertaken when the experimental results are discussed.

As noted earlier, the radius of gyration is an important aggregate property because it directly affects scattering properties computed using RDG theory. Thus, the simulated aggregates were used to compare actual values of the radius of gyration with values found from projected images of the aggregates. These results are illustrated in Fig. 37 where  $R_g(3D)/R_g(2D)$  is plotted as a function of  $N$  for  $N$  in the range 20-1000. Remarkably, the ratio of the actual to projected radius of gyration is essentially independent of  $N$  and has a value of 1.24 with a standard deviation less than 0.01, i.e.:

$$R_g(3D) = 1.24 R_g(2D) \quad (30)$$

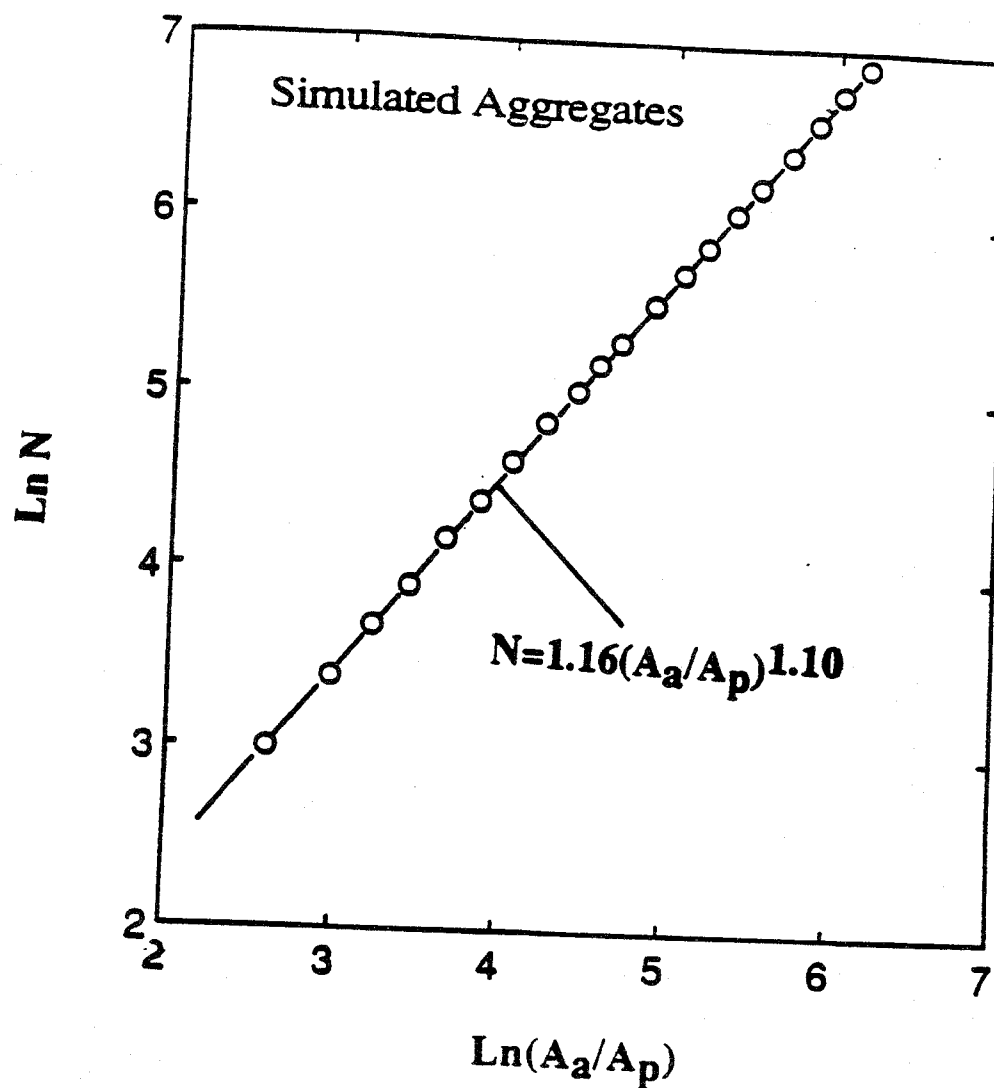


Fig. 36 Number of primary particles as a function of projected area ratio for simulated soot aggregates.

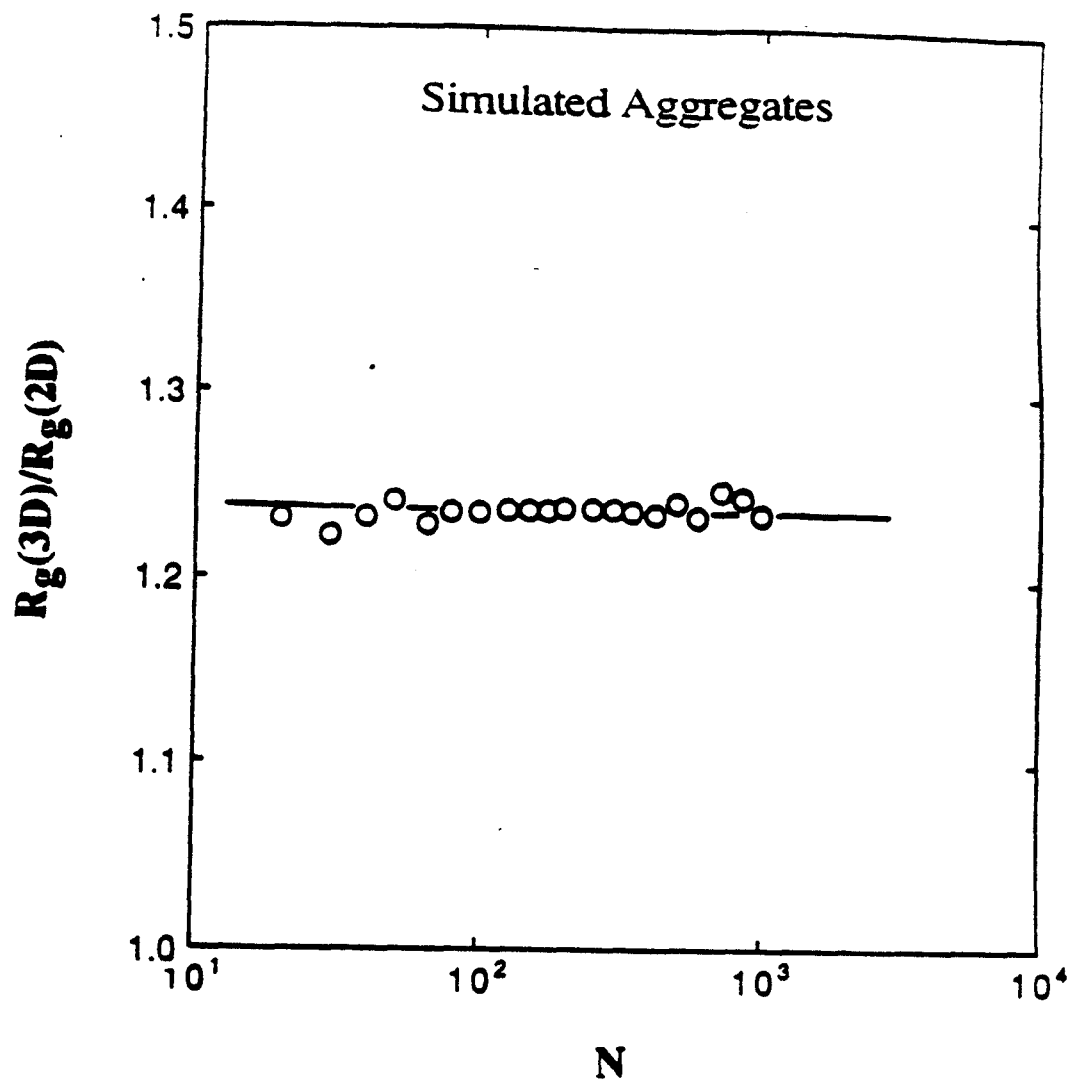


Fig. 37 Ratio of actual to projected radius of gyration as a function of aggregate size for simulated soot aggregates.

Thus, equations (28) and (30) provide convenient relationships between the properties of projected images of aggregates, and the values of  $N$  and  $R_g$  needed to assess the fractal properties of aggregates that are defined in equation (28).

Direct evaluation of fractal properties from equation (28) requires either extensive data reduction of stereopair images or the alternative evaluation from the properties of projected images through equations (28) and (30) that was just discussed. Information of this type is not often available so that several simplified methods based on projected aggregate dimensions have been developed, as discussed by Jullien and Botet (1987). One approach involves the use of the maximum projected length of the aggregate,  $L$ , as follows (Jullien and Botet, 1987):

$$N = k_{fL}(L/d_p)^{D_f} \quad (31)$$

An alternative approach, used during earlier work in this laboratory (Köylü and Faeth, 1992), involves use of the geometric mean of  $L$ , and the maximum projected width normal to  $L$ ,  $W$ , as follows (Jullien and Botet, 1987):

$$N = k_{fLW}((LW)^{1/2}/d_p)^{D_f} \quad (32)$$

where the mean value of  $d_p$  is used in the correlations of equations (31) and (32), similar to equation (28).

Comparing equations (28), (31) and (32) indicates that  $L$  and  $(LW)^{1/2}$  in equations (31) and (32), act as surrogates for  $R_g$  in the fundamental fractal relationship of equation (28). Thus, the relationship between these various lengths is of interest and is illustrated in Fig. 38. These results involve plots of  $L/(2R_g)$  and  $(LW)^{1/2}/(2R_g)$  as a function of  $N$ . Unlike  $R_g(3D)/R_g(2D)$ , the ratios of either  $L$  or  $(LW)^{1/2}$  and  $R_g$  are seen to decrease as  $N$  increases and only approach relatively constant values for  $N > 100$ , where

$$L/(2R_g) = 1.49 \quad (33)$$

$$(LW)^{1/2}/(2R_g) = 1.17 \quad (34)$$

with standard deviations of 0.02 and 0.03, respectively. The smaller value of this ratio for  $(LW)^{1/2}$  than for  $L$  is quite reasonable because  $(LW)^{1/2}$  involves  $W$ , which is less than  $L$  by definition, for each aggregate. The effect of the variation of this ratio with  $N$  is of course negligible when data for large aggregates are processed to find  $D_f$ . However, this



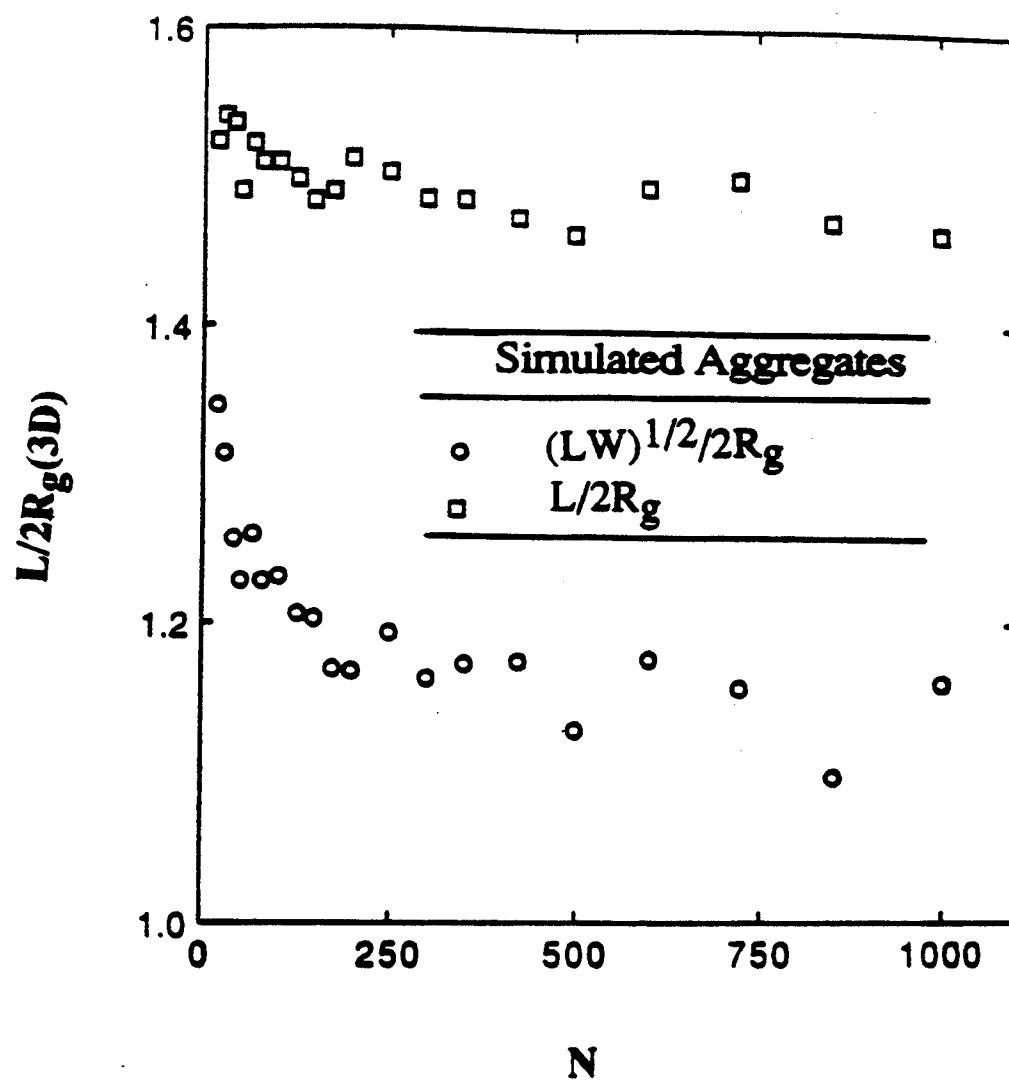


Fig. 38 Number of primary particles as a function of aggregate characteristic dimensions for simulated soot aggregates.

rarely is the case and the progressive reduction of the ratios generally acts to increase the apparent value of  $D_f$  when either  $L$  or  $(LW)^{1/2}$  is used as a surrogate for  $R_g$ . Fortunately, the effect of this variation on determinations of  $D_f$  is not large, ca. 5%, as discussed subsequently in connection with experimental measurements of aggregate properties.

Puri et al. (1993) also have considered values of  $L/(2R_g)$  based on the measurements of Samson et al. (1987). These results were obtained using a 36-aggregate sample of overfire soot from a laminar acetylene flame and yield  $L/(2R_g) = 1.78$  (Puri et al., 1993), which is roughly 20% larger than the present large  $N$  results. This behavior probably is caused by the relatively small aggregate sample used by Puri et al. (1993), e.g., these results also exhibit an unusually small value of  $D_f$  as discussed later.

### 3.3 Flame Generated Aggregates

Experimental Methods. Soot structure also was observed using flame-generated aggregates collected by thermophoretic sampling. Sampling procedures were based on the methods of Dobbins and Megaridis (1987, 1991) with specific techniques identical to past work in this laboratory (Köylü and Faeth, 1992). The sampling surfaces were the carbon-supported copper grids used to hold TEM specimens (3 mm diameter 200 mesh copper grids supported by a 20 nm-thick elemental carbon film, SPI Supplies, Philadelphia, part no. 3520C), aligned parallel to the mean flow direction. The probes were stored outside the flame and were inserted briefly into the flame environment using a double-acting pneumatic cylinder. Sampling times were controlled so that soot aggregates covered no more than 10% of the TEM grid in order to avoid overlapping aggregates on the grid. The time of transit of the grids to and from the sampling location through the flame environment was less than 5% of the sampling time so that soot on the grid was representative of the sampling location. This effect is not of any consequence for the soot sampled in the fuel-lean region of buoyant turbulent diffusion flames, however, because the properties of this soot are independent of position in any event (Köylü and Faeth, 1992).

The principles of thermophoretic sampling are discussed elsewhere, see Rosner et al. (1991) and references cited therein. For present conditions, primary particle diameters were less than 60 nm, which implies that primary particle dimensions are smaller than the mean free path for all sampling conditions, so that the thermophoretic velocities of individual primary particles are identical. In addition, Rosner et al. (1991) have shown that the thermophoretic velocities of aggregates and individual primary particles agree within 20%, even when the aggregates are larger than mean free path lengths. Thus, effects of

intrinsic bias with respect to aggregate size for the present thermophoretic sampling technique are small.

The samples were observed using a JEOL 2000FX analytical electron microscope system with a 1 nm edge-to-edge resolution and sample tilting angles up to  $\pm 45^\circ$ . Magnifications used for the present measurements were in the range 20,000-300,000. The procedure involved selecting aggregates randomly at low magnification, and then increasing the magnification in order to analyze them. The images were processed using the IMAGE computer algorithm to find projected aggregate areas and dimensions, as well as the projected positions and sizes of primary particles. Images at various angles of projection, as well as stereopairs, were then analyzed independently to find the corresponding three-dimensional properties of aggregates. Latex spheres having a diameter of 91 nm (with a standard deviation of 5.8 nm) were used to calibrate the TEM images. Specific sampling procedures and the experimental uncertainties of the soot structure parameters derived from these measurements will be considered when the results are discussed.

Results and Discussion: Turbulent Flames. The most extensive measurements of soot aggregate properties were made for the soot in the fuel-lean region of buoyant turbulent diffusion flames in the long residence time regime. As noted earlier, soot for a particular fuel at these conditions does not depend on position in the fuel-lean region or residence time (Köylü and Faeth, 1992). Specific measurements involved soot within acetylene, propylene, ethylene and propane flames, see Köylü and Faeth (1992) for a complete description of experimental conditions. The measurements involved a total of 127 aggregates which contained 10-500 primary particles per aggregate.

The first issue to be considered using the measured aggregate structure properties was the relationship between the number of primary particles in an aggregate and its projected area on a TEM image. These results are illustrated in Fig. 39, for aggregates in the fuel-lean region of buoyant turbulent diffusion flames at long residence times. Composite results for soot from all the fuels are illustrated in the figure. However, even though specific aggregate properties differ for the various flame systems, all the flames yield the same relationship between the number of primary particles in an aggregate and its projected area.

Similar to the simulated results illustrated in Fig. 36, the measured results illustrated in Fig. 39 suggest a correlation between the number of primary particles in an aggregate

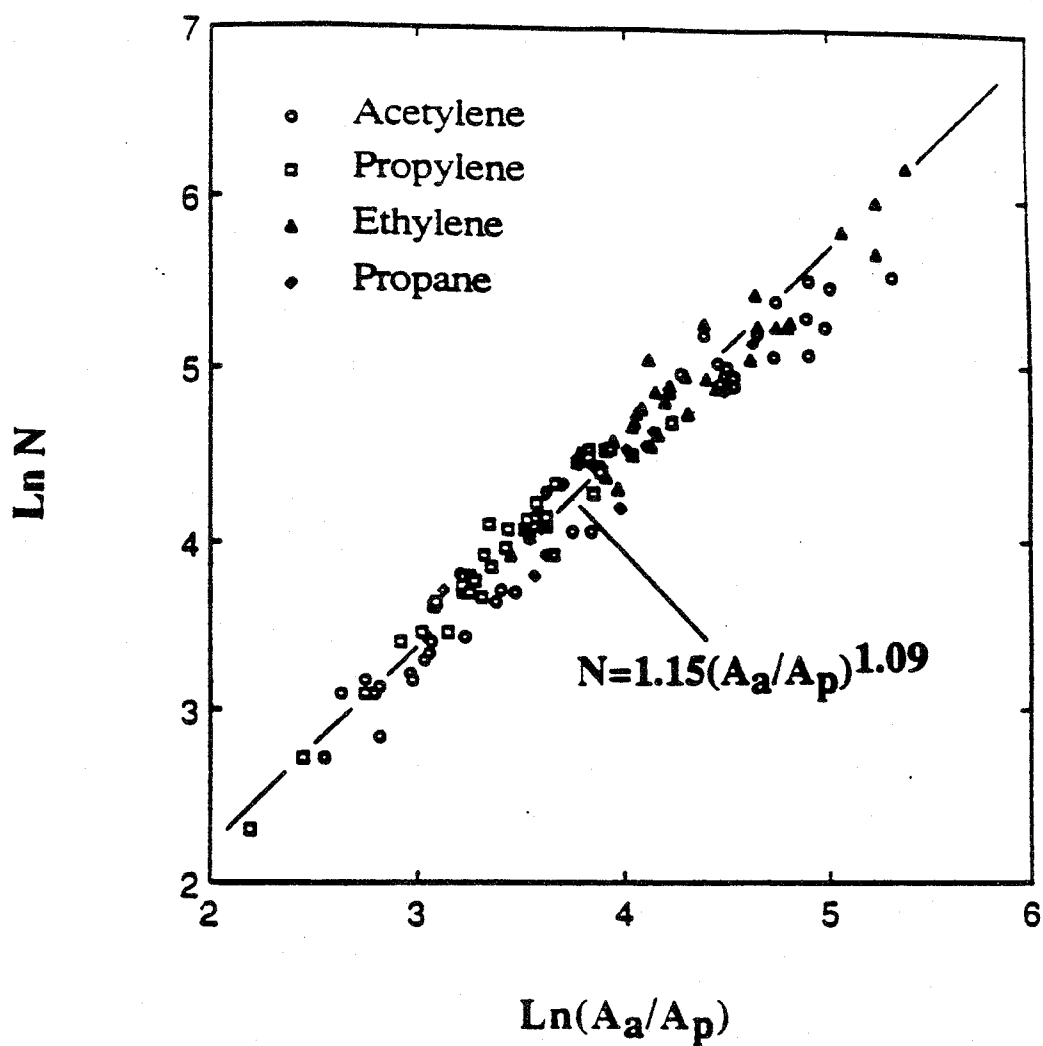


Fig. 39 Number of primary particles as a function of projected area ratio for soot aggregates from the overfire region of buoyant turbulent diffusion flames at long residence times.

and its projected area. In fact, the empirical correlation found from the results illustrated in Fig. 39 is:

$$N = 1.15(A_a/A_p)^{1.09} \quad (35)$$

with standard deviations of  $\alpha$  and  $k_a$  of 0.02 and 0.18 respectively. Within statistical significance, these values are identical to the results found for the numerically simulated aggregates which yielded  $\alpha = 1.10$  and  $k_a = 1.16$  with smaller standard deviations. Based on these findings it appears that the original correlation of equation (29) from Samson et al. (1987), Megaridis and Dobbins (1989, 1990) and Köylü and Faeth (1992) is reasonable, except that  $k_a$  should be increased from unity to roughly 1.15. This effect implies that  $N$  was somewhat underestimated during earlier evaluations of fractal dimensions, based on expressions similar to equations (31) and (32). This effect modifies values of  $k_{fL}$  and  $k_{fLW}$  inferred from these measurements but does not influence the determination of the fractal dimension,  $D_f$ .

The major effort of the present investigation was the determination of fractal prefactor,  $k_f$ , in equation (28) by measurements of  $N$  and  $R_g$  for the fuel-lean soot aggregates within buoyant turbulent diffusion flames in the long residence time regime. Similar to the results illustrated in Fig. 39, the fractal properties of aggregates for the various fuels — acetylene, propylene, ethylene and propane — were identical within experimental uncertainties, even though other properties — such as  $d_p$  and the mean number of primary particles per aggregate — differed considerably. The measured variation of  $N$  with  $R_g/d_p$  for the fuel-lean soot aggregates is illustrated in Fig. 40. The scatter of this data is appreciable, reflecting the problems of measuring  $R_g$  from projected images of aggregates at various angles. The fractal properties of the aggregates are clearly independent of fuel type, however, even though other properties of the aggregates (e.g.,  $d_p$ , the mean number of primary particles per aggregate, etc.) differ considerably for soot formed from combustion of the various fuels. The best fit correlation of the measurements in Fig. 40 yields

$$N = 8.5(R_g/d_p)^{1.65} \quad (36)$$

with standard deviations of  $D_f$  and  $k_f$  of 0.06 and 2.6, respectively. The standard deviation of  $k_f$  is relatively large; nevertheless, due to the relatively large data sample the corresponding uncertainty of the mean value of  $k_f$  is modest, i.e., the experimental uncertainty of the mean value of  $k_f$  (95% confidence) is 0.45 while the corresponding uncertainty of  $D_f$  is 0.12.

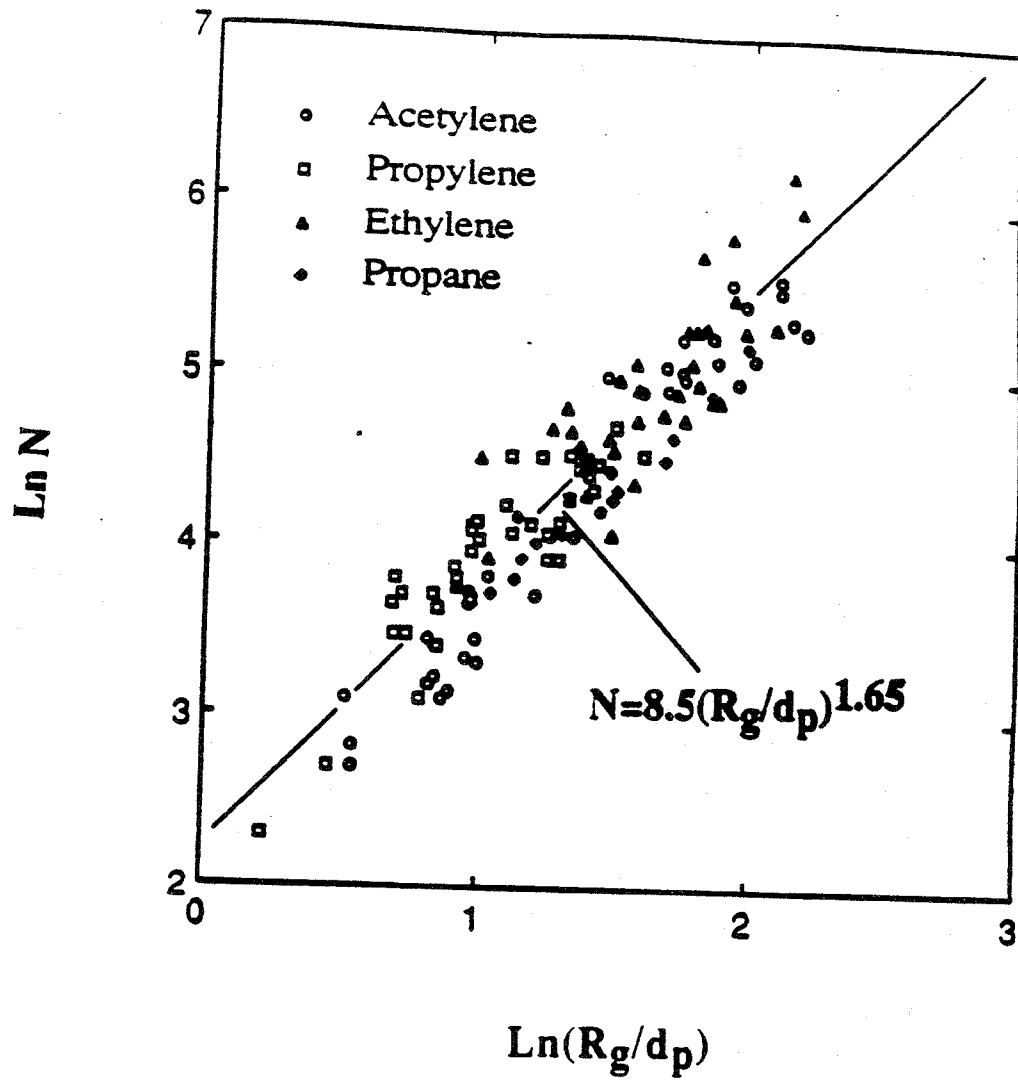


Fig. 40 Number of primary particles as a function of radius of gyration for soot aggregates from the overfire region of buoyant turbulent diffusion flames at long residence times.

The value of the fractal dimension found directly from the results of Fig. 40,  $D_f = 1.65$ , is somewhat low in comparison to earlier measurements of the same soot based on sampling and scattering determinations (Köylü and Faeth, 1992, 1994b). For example, sampling and TEM measurements based on correlations of  $N$  as a function of  $(LW)^{1/2}$  yielded  $D_f = 1.75$  with an experimental uncertainty (95% confidence) of 0.07 over the four fuels (Köylü and Faeth, 1992). The difference between the earlier and present values of  $D_f$  merits some explanation even though its statistical significance is marginal. This behavior follows from the discussion of Fig. 38; namely, that values of  $D_f$  based on  $(LW)^{1/2}$  are somewhat larger than those based on  $R_g$  for a similar range of aggregate sizes, due to the progressive reduction of  $(LW)^{1/2}/R_g$  with increasing aggregate size.

A more significant difference between the present value of  $D_f$  from equation (36), and other results, involves determinations of  $D_f$  based on light-scattering measurements (Köylü and Faeth, 1994a). For example,  $D_f$  found from the light-scattering measurements yielded a value of 1.82 with an experimental uncertainty (95% confidence) of 0.08 which is significantly greater than the present determination given by equation (36). This difference can be explained, however, by noting that the present sampling and TEM analysis yielded a progressive increase of  $D_f$  as both the size of largest aggregates and the sample size were increased. This behavior is consistent with larger observed values of  $D_f$  for the light-scattering measurements because these results emphasize the largest aggregates in the aggregate size distribution, as well, and clearly involve averages over a large number of aggregates (Köylü and Faeth, 1994a). Based on this observation, the effect of aggregate size on the present determination of  $D_f$  was estimated by Richardson extrapolation of the available variation of  $D_f$  with maximum aggregate size in the sample from the present data. This procedure involved plotting  $D_f$  found for samples containing aggregates smaller than a particular size  $N$ , as a function of  $1/N$ . The resulting plot was nearly linear for  $N > 40$  and was extrapolated to  $N \rightarrow \infty$  in order to obtain an estimate of  $D_f = 1.83$  from the present sampling and TEM measurements (Köylü and Faeth, 1994a). Clearly, this value is in good agreement with the light-scattering determinations of  $D_f = 1.82$ , which also emphasize the largest aggregates in the distribution, as noted earlier.

The variation of  $k_f$  with maximum aggregate size in the present samples was less significant than the variation of  $D_f$ ; therefore,  $k_f = 8.5$  from equation (36) represents the present best estimate of this parameter. This value agrees within experimental uncertainties with recent estimates of Puri et al. (1993) based on measurements of Samson et al. (1987) and Megaridis and Dobbins (1990). In particular, analysis of measurements of  $N$  and  $R_g$  for a 36-aggregate sample of overfire soot from a laminar acetylene flame reported by

Samson et al. (1987) yielded  $k_f = 9.22$  (Puri et al., 1993). However,  $D_f = 1.40$  for this sample, which is unusually low, so that the value of  $k_f$  was questioned based on potential sampling limitations (Puri et al., 1993). Other estimates were obtained from measurements of Megaridis and Dobbins (1990) for a nonsmoking laminar ethylene/air flame, taking  $L/(2R_g) = 1.78$ , to yield  $k_f = 8.3$  and  $8.9$  for the two available aggregate samples from Megaridis and Dobbins (1990). As noted earlier, in connection with the discussion of Fig. 38, this value of  $L/(2R_g)$  is somewhat larger than the present findings, although the corresponding values of  $k_f$  agree with present results within experimental uncertainties. Other earlier estimates of  $k_f$  are based on numerical simulations of aggregation processes and generally yield values of  $k_f$  that are smaller than present estimates, see Wu and Friedlander (1993) and references cited therein. An example of this behavior is  $k_f = 5.8$ , found by Puri et al. (1993) based on the cluster-cluster aggregation simulation of Mountain and Mulholland (1988). The reasons for the low values of  $k_f$  from these simulations in comparison to subsequent measurements are not understood at the present time.

The fractal properties of the soot in the fuel-lean region of the buoyant turbulent diffusion flames at long residence times also can be considered from the results illustrated in Fig. 41. In this case,  $N$  is plotted as a function of the geometric mean projected aggregate size  $(LW)^{1/2}$  for the four fuels over the same range of conditions as Fig. 40. The least-squares correlation of the measurements yields  $D_f = 1.73$  and  $k_{fLW} = 1.54$  with standard deviations of 0.04 and 0.30, respectively. As discussed in connection with Fig. 38, the apparent value of  $D_f$  is somewhat larger when found from  $(LW)^{1/2}$ , 1.73, than the value found from  $R_g$ , 1.65, for the same sample. All things considered, however, suggests the following estimates of the fractal properties of the fuel-lean soot:  $D_f = 1.82$  with an uncertainty (95% confidence) of 0.08 from the light scattering measurements (Köylü and Faeth, 1994a), supported by the extrapolated sampling results of Fig. 41; and  $k_f = 8.5$  with an uncertainty (95% confidence) of 0.5, based on the sampling results of Fig. 40.

Results and Discussion: Laminar Flames. The final experimental results involved soot found in a laminar diffusion flame. In this case, samples were obtained at seven different locations along the axis of a weakly-buoyant acetylene/air laminar jet flame at a pressure of 0.25 atm. The test condition involved a burner diameter of 3.3 mm, and a burner exit Reynolds number of 80, which yielded a luminous soot-containing region roughly 50 mm long. Soot was sampled in both the fuel-rich and fuel-lean regions of the flame, over the range  $x/d$  of 1.92-13.42, to obtain a total of 618 aggregates with  $N$  in the range 5-1500.



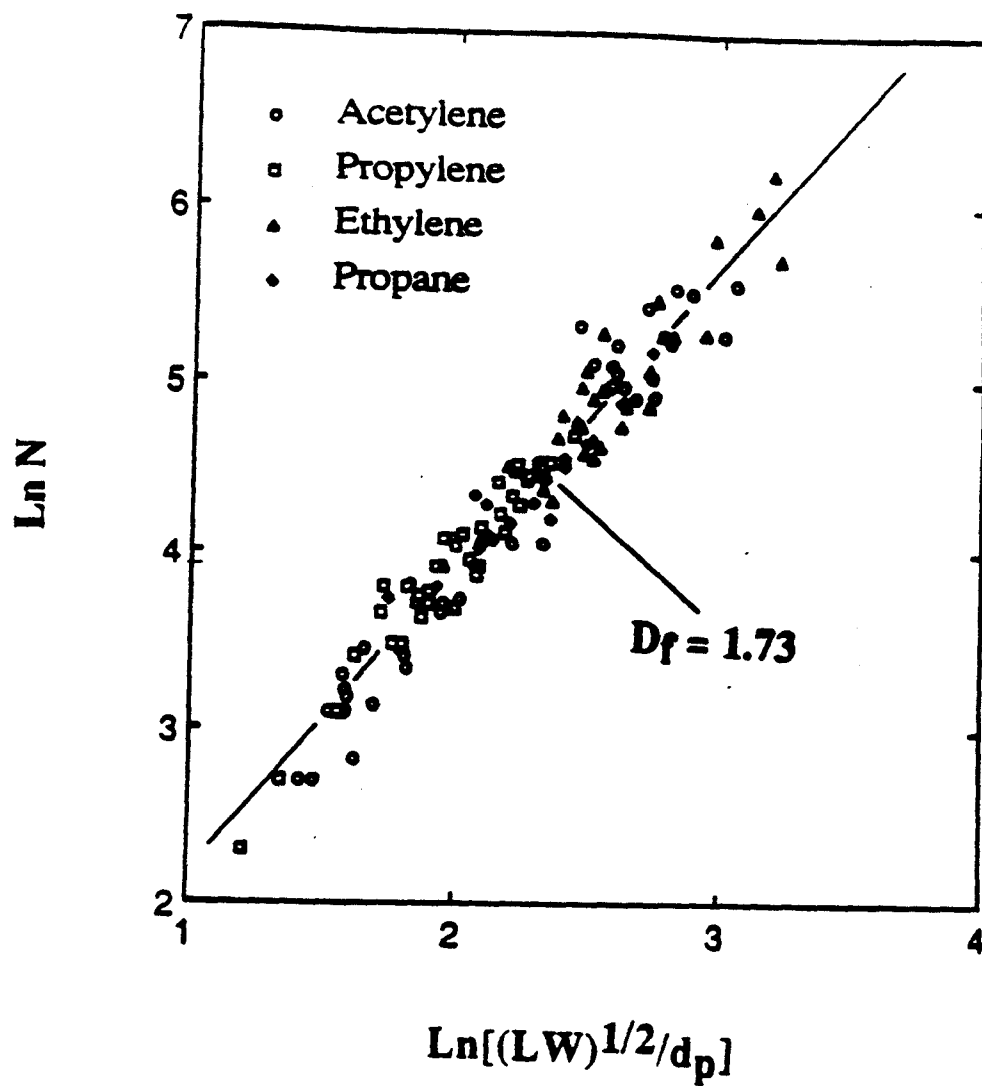


Fig. 41 Number of primary particles as a function of aggregate characteristic dimensions for soot aggregates from the overfire region of buoyant turbulent diffusion flames at long residence times.

The main results considered for soot in the laminar flame involved fractal properties. Measurements to find fractal properties are illustrated in Fig. 42 where  $N$  is plotted as a function of  $(LW)^{1/2}$ . Similar to results obtained from turbulent flames, the fractal properties of the soot illustrated in Fig. 42 were independent of the point where the soot was sampled, even though a range of fuel-lean and fuel-rich conditions were used and properties such as  $d_p$  and the mean number of primary particles per aggregate varied considerably with position in the flame. Then, treating all the laminar flame soot as a single sample population with respect to fractal properties yielded a best fit correlation of the measurements according to equation (32) with  $D_f = 1.78$  and  $k_{fLW}$  of 1.33 with standard deviations of 0.012 and 0.23, respectively. The value of  $D_f$  for this soot is somewhat larger than the value for overfire soot found in Fig. 41 but this is felt to be due to the progressive increase of  $D_f$  with aggregate and sample size discussed in connection with Fig. 40, noting that both the sample size and the maximum value of  $N$  is larger for Fig. 42 than Fig. 41. Additionally, the difference between the results of Figs. 41 and 42 are relatively small so that properties of the laminar flame soot are identical to those of the soot within the fuel-lean region of buoyant turbulent diffusion flames at long residence times, within present experimental uncertainties. This finding suggests that the main fractal properties of soot,  $D_f$  and  $k_f$ , are relatively independent of the fuel and the flame condition.

### 3.4 Conclusions

Study of the structure of soot aggregates, considering aggregates obtained from numerical simulations using cluster-cluster aggregation, measured properties of soot aggregates from the fuel-lean region of buoyant turbulent diffusion flames at long residence times, and measured properties of soot aggregates from both the fuel-rich and fuel-lean regions of weakly-buoyant laminar jet diffusion flames, yielded the following major conclusions:

1. In contrast to primary particle diameters and aggregate size, which vary considerably depending on flame conditions and fuel type, both the fractal properties, and the relationships between actual and projected soot aggregate structure properties, appear to be durable properties of soot that are relatively independent of fuel type and flame condition.
2. The best estimates of the fractal properties of soot aggregates based on present measurements yield  $D_f = 1.82$  and  $k_f = 8.5$  with experimental uncertainties (95% confidence) of 0.08 and 0.5, respectively. These results agree within experimental uncertainties with earlier determinations from sampling and TEM measurements,

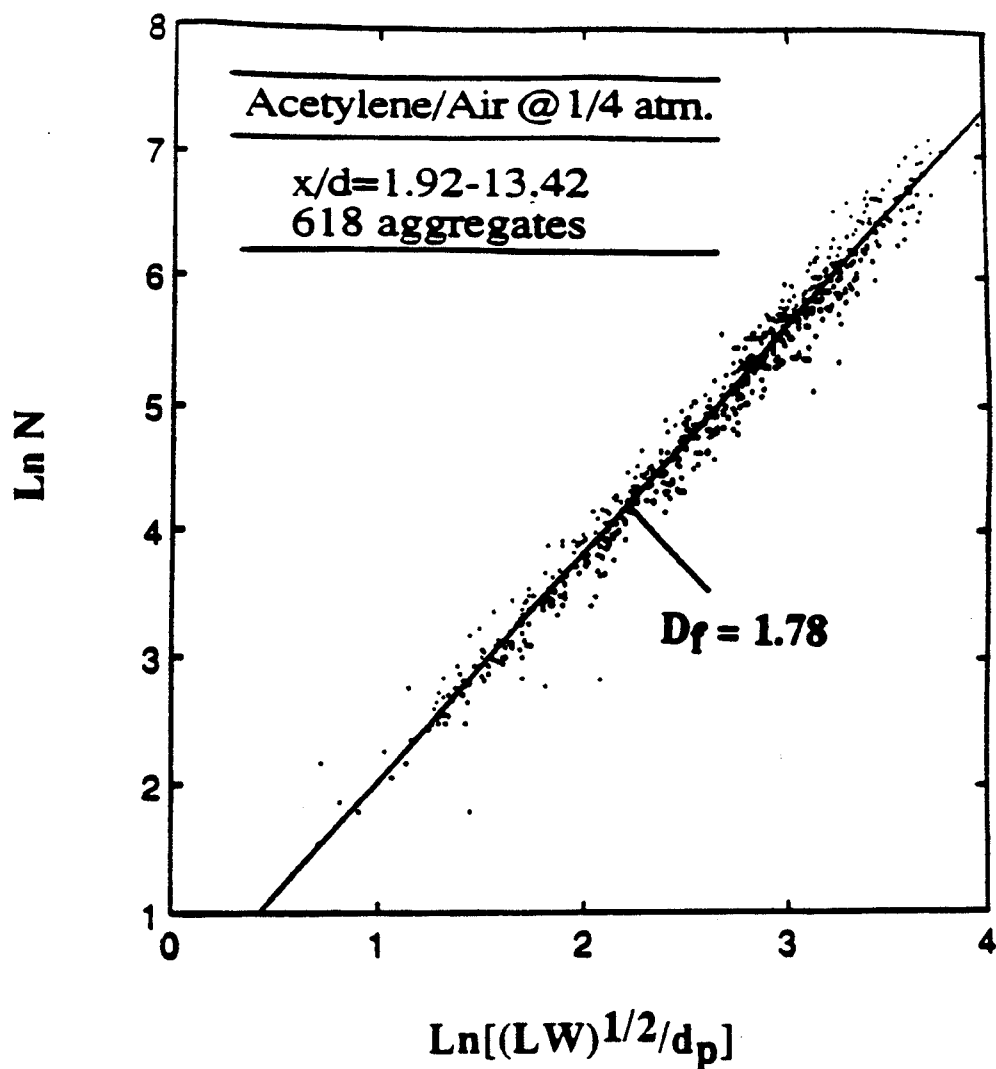


Fig. 42 Number of primary particles as a function of aggregate characteristic dimensions for soot aggregates from the underfire region of a laminar acetylene/air diffusion flame.

see Samson et al. (1987); Megaridis and Dobbins (1990); Puri et al. (1993) and Köylü and Faeth (1994a,b)

3. Both computer simulations and experimental measurements indicated that it is possible to characterize soot aggregate structure properties from projected images, yielding  $k_a = 1.15$ ,  $\alpha = 1.09$  and  $R_g(3D)/R_g(2D) = 1.24$ , with standard deviations of these properties of 0.01, 0.002 and 0.01, respectively. The value of  $\alpha$  is in good agreement with earlier estimates of this property, see Tien and Lee (1982), Megaridis and Dobbins (1989, 1990), and Köylü and Faeth (1992). In contrast, the present value of  $k_a$  is significantly larger than earlier estimates of unity for this parameter.
4. Values of the fractal dimension based on the geometric mean aggregate dimension,  $(LW)^{1/2}$ , were roughly 5% larger than values based on  $R_g$  for the aggregate samples considered here. This behavior is caused by a progressive reduction of  $(LW)^{1/2}/R_g$  with increasing aggregate size. Additionally, values of  $D_f$  from sampling progressively increased as the sample size and the size of the largest aggregate were increased; in contrast,  $k_f$  exhibited a relatively small variation with sample and maximum aggregate size over the present range of conditions.

### References

- Abraham, G. (1960) Jet diffusion in liquid of greater density. ASCE J. Hyd. Dev. 86:1-13.
- Berry, M. V. and Percival, I. C. (1986) Optics of fractal clusters such as smoke. Optica Acta 33:577-591.
- Bilger, R.W. (1976) Turbulent jet diffusion flames. Prog. Energy Combust. Sci. 1:87-109.
- Cai, J., Lu, N. and Sorensen, C.M. (1993) Comparison of size and morphology of soot aggregates as determined by light scattering and electron microscope analysis. Langmuir 9:2861-2867.
- Chen, C.J. and Rodi, W. (1980) *Vertical Turbulent Buoyant Jets: A Review of Experimental Data*, Pergamon Press, Oxford, p. 16.
- Dai, Z., Tseng, L.-K. and Faeth, G.M. (1993) Mixture fraction and velocity statistics in fully-developed turbulent plumes. Proceedings of the Fall Technical Meeting, Eastern Section of the Combustion Institute, The Combustion Institute, Pittsburgh, 173-176.

- Dai, Z., Tseng, L.-K. and Faeth, G.M. (1994a) Structure of round, fully-developed, buoyant turbulent plumes. J. Heat Trans. 116:409-419.
- Dai, Z., Tseng, L.-K. and Faeth, G.M.(1994b) Velocity statistics of round, fully-developed buoyant turbulent plumes. J. Heat Transfer, in press.
- Dai, Z., Tseng, L.-K. and Faeth, G.M. (1994c) Buoyant turbulent plumes revisited. *Heat and Mass Transfer 94*, A.R. Balakrishnan and S.S. Murthy, ed., Tata McGraw-Hill Publishing Co., Lmtd., New Delhi, pp. 59-66.
- Dalzell, W.H. and Sarofim, A.F. (1969) Optical constants of soot and their application to heat flux calculations. J. Heat Trans. 91:100-104.
- Dalzell, W.H., Williams, G.C. and Hottel, H.C. (1970) A light scattering method for soot concentration measurements. Combust. Flame 14:161-170.
- Dobbins, R.A. and Megaridis, C.M. (1987) Morphology of flame-generated soot as determined by thermophoretic sampling. Langmuir 3:254-259.
- Dobbins, R.A. and Megaridis, C.M. (1992) Absorption and scattering of light by polydisperse aggregates. Appl. Optics, 30:4747-4754.
- Erickson, W.D., Williams, G.C. and Hottel, H.C. (1964) Light scattering measurements on soot in a benzene-air flame. Combust. Flame 8:127-132.
- Faeth, G.M. (1994) Soot morphology and optical properties in nonpremixed turbulent flame environments. Proceedings of the Spring Technical Meeting, Canadian Section of the Combustion Institute, Kingston, Ontario, pp. 2-1 to 2-5.
- Faeth, G.M. and Köylü, Ü.Ö. (1994) Soot morphology and optical properties in nonpremixed turbulent flame environments. Combust. Sci. Tech., submitted.
- Farias, T., Carvalho, M.G, Köylü, Ü.Ö. and Faeth, (1993) A computational study of the absorption and scattering properties of soot. Proceedings of the Fall Technical Meeting, Eastern States Section of the Combustion Institute, The Combustion Institute, Pittsburgh, 394-397.
- Farias, T., Carvalho, M.G, Köylü, Ü.Ö. and Faeth, G.M.(1994a) Computational evaluation of approximate Rayleigh-Debye-Gans/fractal-aggregate theory for the absorption and scattering properties of soot. J. Heat Trans., in press.
- Farias, T.L., Carvalho, M.G., Köylü, Ü.Ö. and Faeth, G.M. (1994b) Scattering Properties of Polydisperse Soot Aggregates. Eurotherm Seminar No. 37: Heat Transfer in Radiating and Combusting Systems -2, Saluggio, Italy.
- George, W.K., Jr., Alpert, R.L. and Tamanini, F. (1977) Turbulence measurements in an axisymmetric buoyant plume. Int. J. Heat Mass Trans. 20:1145-1154.
- Hinze, J. O. (1975) *Turbulence*, 2nd ed., McGraw-Hill, New York, 175-319.
- Jullien, R. and Botet, R. (1987) *Aggregation and Fractal Aggregates*, World Scientific Publishing Co., Singapore, 45-60.

- Kotsovinos, N.E. (1985) Temperature measurements in a turbulent round plume. Int. J. Heat Mass Trans 28:771-777.
- Kotsovinos, N.E. and List, E.J. (1977) Turbulent buoyant jets. Part 1. Integral properties. J. Fluid Mech. 81:25-44.
- Kounalakis, M.E., Sivathanu, Y.R. and Faeth, G.M. (1991) Infrared radiation statistics of nonluminous turbulent diffusion flames. J. Heat Trans. 113:37-445.
- Köylü, Ü.Ö. (1992) Emission, structure and optical properties of overfire soot from buoyant turbulent diffusion flames. Ph.D. Thesis, The University of Michigan, Ann Arbor, Michigan.
- Köylü, Ü.Ö. and Faeth, G.M. (1991a) Properties of carbon monoxide and soot emissions from buoyant turbulent diffusion flames. Final Report, Grant No. 60NANB8D0833, The University of Michigan, Ann Arbor, Michigan.
- Köylü, Ü.Ö. and Faeth, G.M. (1991b) Carbon monoxide and soot emissions from liquid-fueled buoyant turbulent diffusion flames. Combust. Flame 87, 61-76.
- Köylü, Ü.Ö. and Faeth, G.M. (1992) Structure of overfire soot in buoyant turbulent diffusion flames at long residence times. Combust. Flame 89, 140-156.
- Köylü, Ü.Ö. and Faeth, G.M. (1993a) Radiation properties of flame-generated soot. J. Heat Trans. 115, 409-417.
- Köylü, Ü. Ö. and Faeth, G.M. (1993b) Soot scattering properties at fuel-rich conditions in buoyant laminar diffusion flames. Proceedings of the Eastern and Central States Sections Technical Meeting, The Combustion Institute, Pittsburgh, 547-551.
- Köylü, Ü.Ö. and Faeth, G.M. (1994a) Optical properties of overfire soot in buoyant turbulent diffusion flames at long residence times. J. Heat Trans. 116:152-159.
- Köylü, Ü.Ö. and Faeth, G.M. (1994b) Optical properties of soot in buoyant laminar diffusion flames. J. Heat Trans., in press.
- Köylü, Ü.Ö., Sivathanu, Y. and Faeth, G.M. (1991) Carbon monoxide emissions from buoyant turbulent diffusion flames. *Third International Symposium on Fire Safety Science*, Elsevier, London, 625-634.
- Köylü, Ü.Ö., Dai, Z., Tseng, L.-K. and Faeth, G.M. (1992) Radiation and mixing properties of buoyant turbulent diffusion flames. Report No. GDL/GMF-92-03, The University of Michigan, Ann Arbor, Michigan.
- Köylü, Ü.Ö., Dai, Z., Tseng, L.-K. and Faeth, G.M. (1993) Radiation and mixing properties of buoyant turbulent diffusion flames. Report No. GDL/GMF-93-01, The University of Michigan, Ann Arbor, Michigan.
- Köylü, Ü.Ö., Faeth, G.M., Farias, T.L. and Carvalho, M.G. (1994) Fractal and projected structure properties of soot aggregates. Combust. Flame, in press.

- Lai, M.-C. and Faeth, G.M. (1987) Turbulence structure of vertical adiabatic wall plumes. J. Heat Trans. 109, 663-670; *Ibid.*, A combined laser-doppler anemometer/laser-induced fluorescence system for turbulent transport measurements. J. Heat Trans. 109, 254-256.
- Lai, M.-C., Jeng, S.-M. and Faeth, G.M. (1986) Structure of turbulent adiabatic wall plumes. J. Heat Trans. 108:827-834.
- List, E.J. (1982) Turbulent jets and plumes. Ann. Rev. Fluid Mech. 14:189-212.
- Lockwood, F.C. and Naguib, A.S. (1975) The prediction of fluctuations in the properties of free, round-jet turbulent diffusion flames. Combust. Flame 24:109-124.
- Lumley, J.L. (1978) Computational modeling of turbulent flows. Adv. Appl. Mech. 18:123-176.
- Magnussen, B.F. (1974) An investigation into the behavior of soot in a turbulent free jet C<sub>2</sub>-H<sub>2</sub>-flame. *Fifteenth Symposium (International) on Combustion*, The Combustion Institute, Pittsburgh, 1415-1425.
- Malin, M.R., and Younis, B.A. (1990) Calculation of turbulent buoyant plumes with a Reynolds stress and heat flux transport closure. Int. J. Heat Mass Trans. 33:2247-2264.
- Martin, J.E. and Hurd, A.J. (1987) Scattering from fractals. J. Appl. Cryst. 20:61-78.
- Medalia, A.I. and Heckman, F.A. (1969) Morphology of aggregates — II. size and shape factors of carbon black aggregates from electron microscopy. Carbon 7:567-582.
- Megaridis, C.M. and Dobbins, R.A. (1989) Comparison of soot growth and oxidation in smoking and nonsmoking ethylene diffusion flames. Combust. Sci. Tech. 66:1-16.
- Megaridis, C.M. and Dobbins, R.A. (1990) Morphological description of flame-generated materials. Combust. Sci. Tech. 71:95-109.
- Mizushima, T., Ogino, F., Veda, H. and Komori, S. (1979) Application of laser-doppler velocimetry to turbulence measurements in non-isothermal flow. Proc. Roy. Soc. London A366:63-79.
- Morton, B.R. (1959) Forced plumes. J. Fluid Mech. 5:151-163.
- Morton, B.R., Taylor, G.I. and Turner, J.S. (1956) Turbulent gravitational convection from maintained and instantaneous sources. Proc. Roy. Soc. London A234:1-23.
- Mountain, R.D. and Mulholland, G.W. (1988) Light scattering from simulated smoke agglomerates. Langmuir 4:1321-1326.
- Nakagome, H. and Hirata, M. (1977) The structure of turbulent diffusion in an axisymmetrical thermal plume. *Heat Transfer and Turbulent Buoyant Convection* (D.B. Spalding and N. Afgan, eds.), McGraw-Hill, New York, 367-372.

- Ogino, F., Takeuchi, H., Kudo, I. and Mizushima, T. (1980) Heated jet discharged vertically in ambients of uniform and linear temperature profiles. Int. J. Heat Mass Trans. 23:1581-1588.
- Panchapakesan, N.R. and Lumley, J.L. (1993) Turbulence measurements in axisymmetric jets of air and helium. Part. 1. Air jet. J. Fluid Mech. 246:197-223; *ibid.*, Part 2. Helium jet. J. Fluid Mech. 264:225-247.
- Papanicolaou, P.N. and List, E.J. (1987) Statistical and spectral properties of tracer concentration in round buoyant jets. Int. J. Heat Mass Trans. 30:2059-2071.
- Papanicolaou, P.N. and List, E.J. (1988) Investigation of round vertical turbulent buoyant jets. J. Fluid Mech. 195:341-391.
- Papantoniou, D. and List, E.J. (1989) Large scale structure in the far field of buoyant jets. J. Fluid Mech. 209:151-190.
- Peterson, J. and Bayazitoglu, Y. (1992) Measurements of velocity and turbulence in vertical axisymmetric isothermal and buoyant plumes. J. Heat Trans. 114:135-142.
- Pivovarov, M.A., Zhang, H., Ramaker, D.E., Tatem, P.A. and Williams, F.W. (1992) Similarity solutions in buoyancy-controlled diffusion flame modelling. Combust. Flame 92:308-319.
- Puri, R., Richardson, T.F., Santoro, R.J. and Dobbins, R.A. (1993) Aerosol dynamic processes of soot aggregates in a laminar ethene diffusion flame. Combust. Flame 92:320-333.
- Rosner, D.E., Mackowski, D.W. and Garcia-Ybarra, P. (1991) Size- and structure-insensitivity of the thermophoretic transport of aggregated 'soot' particles in gases. Combust. Sci. Tech. 80:87-101.
- Rouse, H., Yih, C.S. and Humphreys, H.W. (1952) Gravitational convection from a boundary source. Tellus 4:201-210.
- Samson, R. J., Mulholland, G. W. and Gentry, J. W. (1987) Structural analysis of soot agglomerates. Langmuir 3:272-281.
- Seban, R.A. and Behnia, M.M. (1976) Turbulent buoyant jets in unstratified surroundings. Int. J. Heat Mass Trans. 19:1197-1204.
- Shabbir, A. (1987) An experimental study of an axisymmetric turbulent buoyant plume and evaluation of closure hypotheses. Ph.D. Thesis, SUNY-Buffalo.
- Shabbir, A. and George, W.K. (1992) Experiments on a round turbulent buoyant plume. NASA Technical Memorandum 105955.
- Shabbir, A. and Taulbee, D.B. (1990) Evaluation of turbulence models for predicting buoyant flows. J. Heat Trans. 112:945-951.
- Shih, T.-H., Lumley, J.L. and Janicka, J. (1987) Second-order modeling of a variable-density mixing layer. J. Fluid Mech. 180:93-116.



- Sorensen, C.M., Cai, J. and Lu, N. (1992) Light-scattering measurements of monomer size, monomers per aggregate, and fractal dimension for soot aggregates in flames. Applied Optics 31:6547-6557.
- Sunderland, P.B., Köylü, Ü.Ö. and Faeth, G.M. (1994) Soot formation in weakly-buoyant acetylene-fueled laminar jet diffusion flames burning in air. Combust. Flame, in press.
- Taulbee, D.B. (1992) An improved algebraic Reynolds stress model and corresponding nonlinear stress model. Phys. Fluids A 4:2555-2561.
- Tence, M., Chevalier, J.P. and Jullien, R. (1986) On the measurement of the fractal dimension of aggregated particles by electron microscopy: experimental method, corrections and comparison with numerical models. J. Physique (Paris) 47:1989-1998.
- Tennekes, H. and Lumley, J.L. (1972) *A First Course in Turbulence*, MIT Press, Cambridge, Massachusetts.
- Tien, C. L. and Lee, S. C. (1982) Flame radiation. Prog. Energy Combust. Sci. 8:41-59.
- Viskanta, R. and Mengüç, M.P. (1987) Radiation heat transfer in combustion systems. Prog. Energy Combust. Sci. 13:97-160.
- Wesborg, B.L., Howard, J.B. and Williams, G.C. (1972) Physical mechanisms in carbon formation in flames. *Fourteenth Symposium (International) on Combustion*, The Combustion Institute, Pittsburgh, 929-940.
- Wu, M.K. and Friedlander, S.K. (1993) J. Colloid. Inter. Science 159:246-248 .
- Zimin, V.D. and Frik, P.G. (1977) Averaged temperature fields in asymmetrical turbulent streams over localized heat sources. Izv. Akad. Nauk. SSSR, Mekhanika Zhidkosti Gaza 2:199-203.

NIST-114  
(REV. 9-92)  
ADMAN 4.09

U.S. DEPARTMENT OF COMMERCE  
NATIONAL INSTITUTE OF STANDARDS AND TECHNOLOGY

MANUSCRIPT REVIEW AND APPROVAL

(ERB USE ONLY)

ERB CONTROL NUMBER

DIVISION

PUBLICATION REPORT NUMBER

CATEGORY CODE

NIST-GCR-95-671

PUBLICATION DATE

June 1995

NUMBER PRINTED PAGES

INSTRUCTIONS: ATTACH ORIGINAL OF THIS FORM TO ONE (1) COPY OF MANUSCRIPT AND SEND TO:  
THE SECRETARY, APPROPRIATE EDITORIAL REVIEW BOARD.

TITLE AND SUBTITLE (CITE IN FULL)

Mixing and Radiation Properties of Buoyant Turbulent Diffusion Flames

CONTRACT OR GRANT NUMBER

Grant Number 60NANB1D1175

TYPE OF REPORT AND/OR PERIOD COVERED

September 1, 1993 - August 31, 1994

AUTHOR(S) (LAST NAME, FIRST INITIAL, SECOND INITIAL)

Dai, Z., Tseng, L.-K., Koylu, U.O., and Faeth, G.M.  
Department of Aerospace Engineering  
University of Michigan  
Ann Arbor, MI 48109-2118

PERFORMING ORGANIZATION (CHECK (X) ONE BOX)

☐ NIST/GAITHERSBURG

☐ NIST/BOULDER

☐ JILA/BOULDER

LABORATORY AND DIVISION NAMES (FIRST NIST AUTHOR ONLY)

SPONSORING ORGANIZATION NAME AND COMPLETE ADDRESS (STREET, CITY, STATE, ZIP)

U.S. Department of Commerce  
National Institute of Standards and Technology  
Gaithersburg, MD 20899

RECOMMENDED FOR NIST PUBLICATION

☐  
☐  
☐  
☐  
☐

JOURNAL OF RESEARCH (NIST JRES)

J. PHYS. & CHEM. REF. DATA (JPCRD)

HANDBOOK (NIST HB)

SPECIAL PUBLICATION (NIST SP)

TECHNICAL NOTE (NIST TN)

☐  
☐  
☐  
☐  
☐

MONOGRAPH (NIST MN)

NATL. STD. REF. DATA SERIES (NIST NSRDS)

FEDERAL INF. PROCESS. STDS. (NIST FIPS)

LIST OF PUBLICATIONS (NIST LP)

NIST INTERAGENCY/INTERNAL REPORT (NISTIR)

☐  
☐  
☐  
☒

LETTER CIRCULAR

BUILDING SCIENCE SERIES

PRODUCT STANDARDS

OTHER NIST-GCR

RECOMMENDED FOR NON-NIST PUBLICATION (CITE FULLY)

☐

U.S.

☐

FOREIGN

PUBLISHING MEDIUM

☒  
☐  
☐

PAPER

DISKETTE (SPECIFY)

OTHER (SPECIFY)

☐

CD-ROM

SUPPLEMENTARY NOTES

ABSTRACT (A 1500-CHARACTER OR LESS FACTUAL SUMMARY OF MOST SIGNIFICANT INFORMATION. IF DOCUMENT INCLUDES A SIGNIFICANT BIBLIOGRAPHY OR LITERATURE SURVEY, CITE IT HERE. SPELL OUT ACRONYMS ON FIRST REFERENCE.) (CONTINUE ON SEPARATE PAGE, IF NECESSARY.)

An investigation of the mixing and radiation properties of buoyant turbulent diffusion flames is described. The study was divided into two phases: (1) the structure and mixing properties of turbulent plumes, which must be understood in order to resolve effects of turbulence/radiation interactions and to benchmark models of buoyant turbulent flows; and (2) the fractal and structure properties of soot aggregates, which must be understood in order to develop nonintrusive methods for measuring soot properties and to estimate the continuous radiation and heterogeneous reaction properties of soot in flame environments.

KEY WORDS (MAXIMUM 9 KEY WORDS; 28 CHARACTERS AND SPACES EACH; ALPHABETICAL ORDER; CAPITALIZE ONLY PROPER NAMES)

diffusion flames; fractal properties; laminar flames; lasers; mixing; soot; soot aggregates; turbulent flames

AVAILABILITY

☒  
☐  
☒

UNLIMITED

☐

FOR OFFICIAL DISTRIBUTION. DO NOT RELEASE TO NTIS.

ORDER FROM SUPERINTENDENT OF DOCUMENTS, U.S. GPO, WASHINGTON, D.C. 20402

ORDER FROM NTIS, SPRINGFIELD, VA 22161

NOTE TO AUTHOR(S) IF YOU DO NOT WISH THIS  
MANUSCRIPT ANNOUNCED BEFORE PUBLICATION,  
PLEASE CHECK HERE. ☐

ELECTRONIC FORM